Modélisation numérique, mesures pour les applications industrielles

Yongfeng Qu

UNIVERSITÉ DE LORRAINE

SCIENCE ET INGÉNIERIE DES MOLÉCULES, DES PRODUITS, DES PROCÉDÉS ET DE l'ÉNERGIE

MÉMOIRE d'HABILITATION A DIRIGER DES RECHERCHES

Discipline : Génie des Procédés et des Produits et des molécules

MODÉLISATION NUMÉRIQUE, MESURES POUR LES APPLICATIONS INDUSTRIELLES

QU Yongfeng

Présentée et soutenue

Le vendredi 15 mai 2020, à l'Université de Lorraine

JURY

Rapporteurs :	Mme.	Xuan-Mi MEYER	Professeur, ENSIACET
	Mme.	Lingai LUO	Professeur, Université de Nantes
	M.	Jean-Charles DE HEMPTINNE	Professeur, IFP School
Examinateurs :	M.	Jean-Noël JAUBERT	Professeur, Université de Lorraine
	M.	Romain PRIVAT	Maître de conférences, Université de Lorraine

A ma famille

Remerciements

En particulier, je tiens à exprimer ma profonde reconnaissance à Monsieur le Professeur Jean-Noël JAUBERT pour la confiance qu'il m'a accordée ainsi que pour son soutien. Je le remercie également pour sa disponibilité et ses précieux conseils.

Mes remerciements s'adressent aux membres de ce jury, pour l'honneur qu'ils me font de participer à l'évaluation de ce travail. Je remercie les rapporteurs de ce mémoire, Mesdames et Monsieur les Professeurs Xuan-Mi MEYER, Lingai LUO et Jean-Charles DE HEMPTINNE. Je remercie également les examinateurs de ce mémoire, qui ont accepté d'en être les suffragants : Monsieur MCF-HdR Romain PRIVAT et Monsieur le Professeur Jean-Noël JAUBERT.

De très nombreuses personnes m'ont apporté leur soutien et ont contribué à ce travail. Que ces personnes soient assurées de ma gratitude. Beaucoup contribuent à la mécanique des fluides cryogéniques : enseignants, chercheurs, ingénieurs. Tous sont soucieux de leur mission et sont, en cela, un exemple pour moi.

Sommaire

1.
PRÉSENTATION GÉNÉRALE

1.1. SITUATION ACTUELLE

Depuis mars 2014, je suis ingénieur R&D à GTT (Gaztransport & Technigaz). Et depuis septembre 2019, je suis enseignant vacataire et suis rattaché à deux unités de l'Université d'Evry Val d'Essonne : le GMP (département Génie Mécanique et Productique) et le CRL (Centre de Ressources en Langues). J'effectue une partie de ma recherche au Laboratoire de Mécanique et d'Energétique au sein de l'équipe Fluide Environnement Identification, FEI.

1.2. PARCOURS

Mon parcours étudiant à l'université s'est principalement déroulé en quatre temps :

En 2001, j'ai obtenu l'équivalent d'une maitrise en génie mécanique à l'Université de Shanghai en Chine.

A partir de 2003, je me suis installé en France pour apprendre la langue française. En 2004, je suis entré à l'université Paris VI et j'ai obtenu deux diplômes de master. Le premier en Mécanique et ingénierie des systèmes (en 2007) et le second en Mécanique des fluides et énergétique (en 2008).

J'ai ensuite débuté une thèse CIFRE en partenariat avec EDF R&D, en Sciences et Techniques de l'Environnement, et plus précisément en Mécanique des fluides numérique (CFD en anglais), sous la direction du Docteur Bertrand CARISSIMO, que j'ai soutenue en novembre 2011. Mon mémoire de thèse s'intitulait : « Modélisation tri-dimensionnelle des échanges radiatifs et convectifs dans l'atmosphère urbaine »

Enfin, à la suite de ma thèse, j'ai effectué deux années de recherche post-doctorale à l'Ecole des Ponts ParisTech.

1.3. ACTIVITES PROFESSIONNELLES

Depuis la fin de ma thèse, je partage mon temps professionnel entre des activités de recherche et développement, d'administration et d'enseignement.

1.3.1. Enseignements

Depuis 2019, j'interviens en tant qu'enseignant vacataire au GMP et au CRL de l'Université d'Evry Val d'Essonne. J'enseigne le génie des procédés et la langue chinoise. J'interviens également au Lycée Nadar professionnel à Draveil où je donne des cours de chinois depuis 2016. Je suis également impliqué dans des échanges ou des projets de coopération entre des écoles françaises et des écoles chinoises.

De 2016 à 2018, j'ai également formé des ingénieurs de GTT à l'utilisation de logiciels scientifiques.

En 2013, j'ai enseigné l'état de l'art sur la modélisation de la dispersion des émissions atmosphériques industrielles pour des étudiants de Master2 « Environnement-Société ». Le cours est centré sur des rappels relatifs aux bases théoriques sur lesquelles reposent le transport et la dispersion des polluants émis dans la basse atmosphère : la dispersion turbulente, la météorologie locale et la dispersion atmosphérique. Ce cours est ouvert aux étudiants de l'Université Paris-Sud 11, des écoles de ParisTech, de l'Ecole Centrale Paris et Supélec, de L'INSTN.

De 2010 à 2013, j'ai encadré des Travaux Pratiques pour étudiants de Master2 « Environnement-Société ». Le TP initie les étudiants à la CFD et au modèle Gaussian pour modéliser le suivi des rejets dans une centrale nucléaire.

1.3.2. Responsabilités administratives et scientifiques

1.3.2.1. Responsable des mesures thermiques

Dans le cadre du projet ANR « EUREQUA » (Evaluation mUltidisciplinaire et Requalification Environnementale des QUArtiers), une campagne de mesures sur les paramètres physiques (météo, acoustique, qualité de l'air) et une enquête auprès des habitants et usagers des quartiers étudiés ont été réalisées conjointement. En tant que co-responsable des mesures thermiques des surfaces urbaines, j'ai participé aux campagnes de Marseille, Paris et Toulouse. J'avais en charge la responsabilité technique de la définition d'un prototype de

mesure et la formation de plusieurs collaborateurs à l'utilisation de la caméra thermique.

Pendant le déroulement du projet, j'ai coordonné les activités techniques et scientifiques relatives à l'acquisition des mesures et à leur modélisation. J'étais également chargé de communiquer les résultats intermédiaires aux partenaires du projet et d'organiser les réunions de suivi.

1.3.2.2. Responsable au sein du GTT

De 2014 à 2017, au sein de la Direction de l'Innovation de l'entreprise GTT, département Calculs et Conception, en tant que responsable de projets avec des partenaires industriels et universitaires, je dois définir les propositions techniques et financières. Ces documents sont indispensables pour trouver un accord sur le contenu scientifique et sur les aspects économiques des projets. Pendant le déroulement des projets, je suis responsable de la coordination des activités techniques et scientifiques relatives à l'acquisition des mesures et à leur modélisation. Je suis aussi chargé de communiquer les résultats intermédiaires aux partenaires industriels et universitaires par le biais de rapports intermédiaires et de discuter des éventuels changements dans les objectifs des projets. A la fin du projet, je dois rédiger rapport final. Une réunion avec les partenaires industriels et universitaires pour une présentation orale des résultats du projet peut aussi être organisée.

De 2017 à 2018, j'assurais le pilotage de l'équipe « Outils et Méthodes » dont le principal objectif est le développement de nouvelles approches numériques afin d'améliorer la modélisation des phénomènes thermodynamiques et thermiques dans une cuve de GNL.

Mes activités principales:

- Activités R&D alimentant le développement de nos outils et méthodes et renforçant notre savoir-faire autour de la compréhension et de la modélisation des phénomènes thermodynamiques du GNL. Cette activité est menée en collaboration avec des partenariats extérieurs (laboratoires, universités et industries…).
- Support métier dans le cadre de projets de développement, principalement le développement de services embarqués ou de technologies concernant la gestion énergétique du navire.
- Management d'une équipe de 4 ingénieurs

L'enjeu majeur consiste à faire le lien entre des sujets R&D complexes et les problématiques opérationnelles nécessitant la mise en place de méthodes numériques adaptées (simplifiées) en cohérence avec les contraintes de mise en œuvre.

Suite à la réorganisation de l'entreprise, je me suis actuellement intégré au nouveau pôle « Modélisation » attaché au département « Process et Instrumentation » de la Direction Technique. Pour répondre aux besoins du marché GNL carburant, je suis chargé du développement de nouveaux outils thermiques pour les projets spéciaux.

1.3.3. Encadrement de thésards et de stagiaires de master

Depuis mon arrivée à GTT, j'ai participé à l'encadrement de deux doctorants :

- I. Noba

Sujet : Modélisation et simulation numérique du comportement de chargement de gaz naturel liquéfié dans une cuve de méthanier (2016-2018)

- A. Dehlouz

Sujet : Modélisation des écoulements diphasiques pour le stockage du Gaz Naturel Liquéfié (GNL) (depuis 2018)

A GTT, j'ai également encadré divers étudiants en stage de Master 2 dont la liste est fournie ci-après :

- P. Ta

Sujet : Modélisation thermique et thermodynamique d'une cuve de navire de transport de GNL dans le cadre du développement d'un calculateur (2014)

- S. El Gharib

Sujet : Modélisation 3D des effets du sloshing sur l'évaporation du GNL dans les cuves d'un méthanier (2015)

- H. Foka Fogue

Sujet : Modélisation numérique en thermique et thermodynamique de l'évaporation du GNL avec l'outil OpenFoam (2015)

- A. Hassine

Sujet : Développement d'une application de simulation de montée en pression dans une cuve cryogénique (2016)

- B. Cuniasse

Sujet : Validation and development of a calculation code for LNG storage and transportation (2016)

- A. Dehlouz

Sujet : Développement d'un modèle numérique 1D dans un code de calcul pour les applications sur le transport maritime du gaz naturel liquéfié (2017)

- A. Ihsine

Sujet : Portage et sécurité d'un outil de calcul thermique et thermodynamique sous Windows (2017)

- L. Mouchaouche

Sujet : Calibration et validation d'un code de calcul thermique et thermodynamique pour les applications sur les transports maritimes du gaz naturel liquéfié (GNL) (2018)

1.3.4. Travaux de recherche

Mes travaux de recherche sont principalement orientés vers le développement de codes numériques et l'acquisition de données pour des applications industrielles. Ces aspects sont largement décrits dans ce manuscrit :

- Le 1er chapitre est dédié aux modélisations en mécanique des fluides numérique (CFD) dans le but de concevoir une ville durable.

- Le 2ème chapitre résume les travaux de modélisation numérique que j'ai menés afin de développer des solutions logicielles permettant d'optimiser la gestion de la cargaison d'un navire transportant du GNL.

- Le 3ème chapitre est consacré aux travaux expérimentaux, notamment les essais cryogéniques chez Ariane Group auxquels j'ai participé. Ariane Group a réalisé en partenariat avec GTT des tests de Boil-off et de montée en pression de liquides cryogéniques à l'intérieur d'une cuve cylindrique de petite taille dans un environnement statique. Les expériences menées par Ariane Group regorgent de données essentielles pour mieux comprendre les phénomènes de Boil-off et de montées en pression et pour améliorer les modèles de la plateforme développée par GTT.

En résumé, je m'attache à développer à la fois des travaux de modélisation et des travaux expérimentaux et tente dans la mesure du possible, de générer une information expérimentale au service de la modélisation.

2.
MODÉLISATION TRIDIMENSIONNELLE DES ÉCHANGES RADIATIFS ET CONVECTIFS DANS L'ATMOSPHÈRE URBAINE POUR UNE VILLE DURABLE

2.1. PROBLEMATIQUE ET OBJECTIFS

Ce travail proposé par EDF R&D s'inscrit dans le cadre du projet « Plateforme voie air » pour lequel des outils de modélisation des écoulements et de la dispersion des polluants dans l'atmosphère sont développés.

Une caractéristique importante des villes est leur bilan énergétique. La structure et les propriétés de la couche limite atmosphérique sont fortement influencées par la présence des surfaces urbaines. En effet, le rayonnement et les échanges thermiques en milieu urbain diffèrent de ceux en milieu rural, en raison de la spécificité des surfaces urbaines (le caractère tridimensionnel, l'inhomogénéité des matériaux et la végétation). Dans de nombreuses études micrométéorologiques, les modèles numériques prenant en compte les bâtiments considèrent généralement l'atmosphère comme neutre, c'est-à-dire sans prendre en compte les effets radiatifs et thermiques. Cette situation peut être justifiée pour les cas de vent fort, mais dans les cas où le vent est assez faible (cas fréquent en ville), où la stratification est forte, cette hypothèse est erronée.

Afin de prendre en compte le rayonnement atmosphérique et les effets thermiques des bâtiments dans les simulations de l'écoulement atmosphérique et la dispersion des polluants en milieux urbains, ils nécessitent la mise en œuvre d'un modèle radiatif 3D prenant en compte les interactions entre rayonnement et milieu bâti. Le domaine de recherche dans lequel se situe cette étude est le difficile problème de la modélisation tridimensionnelle en géométrie complexe des effets thermo-radiatifs et convectifs en milieu urbain réaliste.

2.2. TRAVAUX REALISES

2.2.1. Modèle numérique

Nous avons développé un schéma thermo-radiatif tridimensionnel (3D) à l'échelle du quartier dans le module atmosphérique du Code_Saturne. Les équations mathématiques détaillées qui identifient ce modèle peuvent être trouvées dans la littérature (**Archambeau et al., 2003; Milliez & Carissimo, 2007; 2008**). Notre modèle radiatif prend en compte à la fois le rayonnement

infrarouge atmosphérique et le rayonnement solaire. Un schéma hybride est utilisé pour déterminer la température du sol et celle des toits et des murs.

La figure. 1 montre un aperçu du fonctionnement de notre algorithme. Tout d'abord, la modélisation nécessite les entrées suivantes : date, localisation, configuration urbaine, conditions météorologiques, description des matériaux de surface, etc. A partir d'un champ d'écoulement initial utilisé pour calculer les flux convectifs, les températures de surface sont calculées en utilisant le modèle thermo-radiatif. Ensuite, ces températures de surface sont utilisées comme une condition aux limites pour les simulations CFD, qui sont ensuite effectuées.

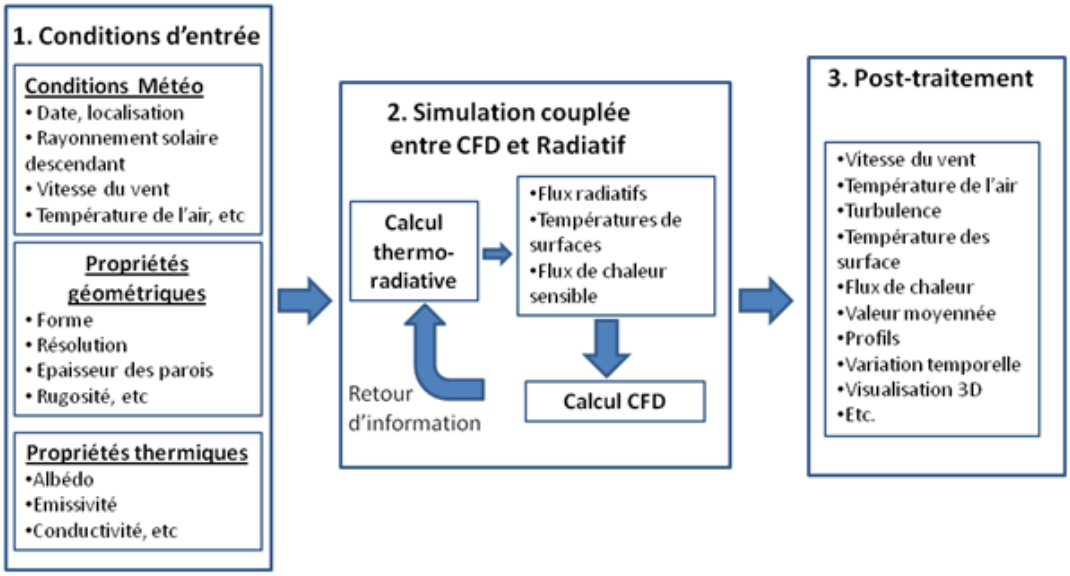

Figure 1 - Schéma de la modélisation dans le modèle Code_Saturne

2.2.2. Validation du modèle sur des géométries simples

La validation du couplage thermo-radiatif-convectif est d'abord effectuée sur des géométries simples. L'article ci-après résume nos résultats et montre la première évaluation du couplage en utilisant les données de la campagne de mesure américaine Mock Urban Setting Test (MUST).

Référence:

Qu, Y., M. Milliez, L. Musson-Genon, B. Carissimo, 2011: Micrometeorological modeling of radiative and convective effects with a building resolving code, J. Appl. Meteor. Climatol., 50 (8) 1713–1724. doi: http://dx.doi.org/10.1175/2011JAMC2620.1

Micrometeorological Modeling of Radiative and Convective Effects with a Building-Resolving Code

YONGFENG QU, MAYA MILLIEZ, LUC MUSSON-GENON, AND BERTRAND CARISSIMO

Teaching and Research Center in Atmospheric Environment (CEREA), Champs-sur-Marne, France

(Manuscript received 10 August 2010, in final form 14 March 2011)

ABSTRACT

In many micrometeorological studies with computational fluid dynamics, building-resolving models usually assume a neutral atmosphere. Nevertheless, urban radiative transfers play an important role because of their influence on the energy budget. To take into account atmospheric radiation and the thermal effects of the buildings in simulations of atmospheric flow and pollutant dispersion in urban areas, a three-dimensional (3D) atmospheric radiative scheme has been developed in the atmospheric module of the Code_Saturne 3D computational fluid dynamic model. On the basis of the discrete ordinate method, the radiative model solves the radiative transfer equation in a semitransparent medium for complex geometries. The spatial mesh discretization is the same as the one used for the dynamics. This paper describes ongoing work with the development of this model. The radiative scheme was previously validated with idealized cases. Here, results of the full coupling of the radiative and thermal schemes with the 3D dynamical model are presented and are compared with measurements from the Mock Urban Setting Test (MUST) and with simpler modeling approaches found in the literature. The model is able to globally reproduce the differences in diurnal evolution of the surface temperatures of the different walls and roof. The inhomogeneous wall temperature is only seen when using the 3D dynamical model for the convective scheme.

1. Introduction

Interest in urban climatology has increased in the past decade. It corresponds to the thermal and dynamical airflow response to the urban system solicitations, resulting in radiative transfers and convective exchanges within the urban air and with the building walls (Grimmond and Oke 1999; Arnfield 2003). In the past few years, numerical studies have been conducted to solve the surface energy balance (SEB) in urban canopies, with different degrees of simplification, using either an integrated representation of the urban canopy (Masson 2000) or a three-dimensional approach (Mills 1996; Miguet and Groleau 2002; Kanda et al. 2005; Krayenhoff and Voogt 2007; Gastellu-Etchegorry 2008; Asawa et al. 2008). Those models share the following parameterizations in their design: the schemes possess separate energy budgets for roofs, roads, and walls; radiative interactions between roads and walls are explicitly treated.

The Town Energy Balance (TEB) scheme of Masson (2000) consists of a facet-averaged scheme with one generic roof, one generic wall, and one generic road. The advantage of the integrated resolution is that few individual SEBs need to be resolved and therefore computation time is kept low, with a simple approach to model the inner-canopy wind flow. TEB has been shown to reproduce accurately the SEB from regional to mesoscale and urban scales (Masson et al. 2002; Lemonsu et al. 2004). Mills (1996) developed the Urban Canopy-Layer Climate Model, which has a detailed representation of the canyon with a highly simplified wind parameterization. The "SOLENE" (Miguet and Groleau 2002) and 3D-Computer Aided Design (Asawa et al. 2008) models are based on a realistic description of the canopy structure using a geometrical 3D surface model assigning radiative and thermal properties to each subfacet of the model and a constant transfer coefficient for each class of elements. The model is originally designed for simulating sunshade, natural lighting, and heat transfers for architectural purposes. The Discrete Anisotropic Radiative Transfer (DART) model (Gastellu-Etchegorry et al. 2004) simulates the radiative transfer in the whole optical domain simultaneously in the atmosphere and in

Corresponding author address: Yongfeng Qu, Teaching and Research Center in Atmospheric Environment (CEREA) (ENPC/EDF R&D), 6–8 avenue Blaise Pascal, 77455 Champs-sur-Marne, France.
E-mail: yongfeng.qu@cerea.enpc.fr

DOI: 10.1175/2011JAMC2620.1

the urban and vegetated landscapes, with or without topography. A major feature of DART is that it can simulate images in the plane of the sensor, for different altitudes from the bottom to the top of the atmosphere. The new version of the DART model, DART-EB, (Gastellu-Etchegorry 2008) includes an energy balance component. In the case of urban canopies, turbulent fluxes and conduction are computed with classical boundary layer laws, using the equations of the TEB model (Masson 2000). The Simple Urban Energy Balance Model for Mesoscale Simulations (SUMM; Kanda et al. 2005), which represents the urban canopy with an infinitely extended regular array of uniform buildings, is more adapted for the mesoscale. The Temperatures of Urban Facets in 3D (TUF-3D) model (Krayenhoff and Voogt 2007) uses the radiosity approach based on interpatch view factors to model radiative exchange between the identical square patches that compose the simplified 3D urban geometry. An exponential inner-canopy wind speed profile is employed. TUF-3D has applications in both surface temperature distributions and thermal remote sensing anisotropy at several scales.

Previously described models have all put a strong emphasis on radiative exchanges but not on a detailed flow field. In this work, in addition to the above applications, we are also interested in applying the model to pollutant dispersion in low–wind speed conditions, when the thermal effects have a strong influence on the flow.

To model the airflow in the urban canopy in nonneutral conditions more accurately and to take into account the 3D convective exchanges, we developed a 3D microscale radiative model coupled with a 3D computational fluid dynamics (CFD) code for complex geometries to simulate dynamics and thermodynamics of the urban atmosphere (Milliez 2006). Differing from other radiative models that calculate the view factors to estimate the incoming radiative fluxes on urban surfaces, our model directly solves the 3D radiative transfer equation in the whole fluid domain. This approach allows us to determine the radiation flux not only on the facets of the urban landscape but also in each fluid grid cell between the buildings. The difference could become important in the case of smoke or fog between the buildings. The model was evaluated with idealized cases, using as a first step a constant 3D wind field (Milliez et al. 2006). The purpose of the work presented here is to study the full radiative–dynamical coupling, using an evolving 3D flow field. First we present the model, and then we discuss in detail the results of the full coupling. We further discuss the influence on the surface temperature of the internal building temperature and the wall thermal modeling, comparing the 3D resolution with the approaches used in other models.

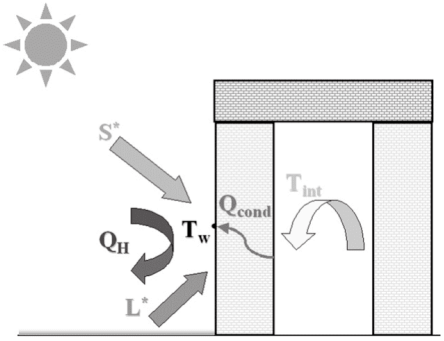

FIG. 1. Schematic representation of the energy exchanges at an urban surface (cross section of a building) (S^*: net shortwave radiative flux; L^*: net longwave radiative flux; Q_H: sensible heat flux; Q_{cond}: conduction heat flux; T_W: wall surface temperature; T_{int}: internal building temperature).

2. Equations and model design

As a key parameter, surface temperature T_{sfc} is determined by the SEB, which governs the energy exchange processes between each urban surface and the atmosphere (Fig. 1). It is given by

$$Q_{cond} + Q_H = L^* + S^*, \quad (1)$$

where Q_{cond} is the conductive heat flux (W m^{-2}) within the building or the ground subsurface that links the surface temperature to the internal-building or the deep-soil temperature, Q_H is the sensible heat flux (W m^{-2}) and depends on the local wind intensity, S^* is the net shortwave radiative flux (W m^{-2}), and L^* is the net longwave radiative flux (W m^{-2}). We neglect in this study the other energy fluxes such as the anthropogenic flux and the latent heat flux. In our model the advection fluxes are taken into account by the full resolution of the flow field.

a. CFD model

To solve the dynamics and therefore to resolve the Q_H term explicitly, simulations are performed with the 3D open-source CFD code known as Code_Saturne (Archambeau et al. 2003), which can handle complex geometry and complex physics. The flow features in built-up areas make the modeling within the urban canopy difficult. Some typical effects that we have to handle are 3D vortices behind the buildings, high wind speed near the edges of the upwind face, wake effects, and modified turbulence.

In this work, we use the atmospheric module of Code_Saturne, described in detail in Milliez and Carissimo (2007), which takes into account the larger-scale meteorological conditions and the thermal stratification of the atmosphere. In our simulations, we use a Reynolds-averaged Navier–Stokes (RANS) approach with a k–ε turbulence closure. The numerical solver is based on a finite-volume approach for collocated variables on an unstructured grid. Time discretization is achieved through a fractional step scheme, with a prediction–correction step.

b. Radiative model

A new atmospheric 3D radiative scheme was developed in Code_Saturne for the urban canopy (Milliez 2006). We have adapted to the atmosphere a radiative heat transfer scheme available for complex geometry in Code_Saturne that solves the radiative transfer equation for a gray nondiffusive semitransparent media:

$$\mathrm{div}[I(\underline{x}, \underline{D})\underline{D}] = -K(\underline{x})L(\underline{x}, \underline{D}) + K(\underline{x})\sigma T_a^4(\underline{x})/\pi, \quad (2)$$

where $I(\underline{x}, \underline{D})$ is the intensity of radiation at the point $\underline{x}$ and for the propagation direction $\underline{D}$, $K(\underline{x})$ is the absorption coefficient, $L(x, \underline{D})$ is the luminance (W m^{-3} sr^{-1}), and T_a is the air temperature (K). In a semitransparent media, I (W m^{-3} sr^{-1}) and K can be considered to be independent of the wavelength and are integrated over the spectrum. The rate of radiation heating S_{rad} (W m^{-3}) is then given by

$$S_{\mathrm{rad}} = -\mathrm{div}\int_0^{4\pi} I(\underline{x}, \underline{D})\underline{D}\, d\Omega, \quad (3)$$

where $d\Omega$ is the element of the solid angle (sr) around the direction.

1) DISCRETE ORDINATE METHOD (DOM)

To solve the radiative transfer equation, we chose the discrete ordinate method (Fiveland 1984; Truelove 1987; Liu et al. 2000), which is based on the directional propagation of the radiative wave. The spatial discretization uses the same mesh as the CFD model. The angular discretization has two resolutions: 32 or 128 directions.

2) SHORTWAVE AND LONGWAVE RADIATION

As is usually done, we separate the atmospheric radiation into shortwave and longwave radiation. The total incoming and outgoing shortwave radiative fluxes for each solid surface are given by

$$S^{\downarrow} = S_D + S_f + S_e \quad \text{and} \quad (4)$$

$$S^{\uparrow} = \alpha S^{\downarrow}, \quad (5)$$

where $S^{\downarrow}$ and $S^{\uparrow}$ are respectively the incoming and outgoing shortwave radiative fluxes (W m^{-2}), S_D is the direct solar flux (W m^{-2}), S_f is the solar flux diffused by the atmosphere above our simulation domain (W m^{-2}), S_e is the flux diffused by the environment, that is, resulting from the multireflections on the other subfacets (W m^{-2}), and α is the albedo of the surface.

We express the longwave radiation flux for each surface as

$$L^{\downarrow} = L_a + L_e \quad \text{and} \quad (6)$$

$$L^{\uparrow} = \varepsilon\sigma T_{\mathrm{sfc}}^4 + (1 - \varepsilon)(L_a + L_e), \quad (7)$$

where $L^{\downarrow}$ and $L^{\uparrow}$ are respectively incoming and outgoing longwave radiation flux (W m^{-2}), ε is emissivity of the surface; σ is the Stefan–Boltzmann constant ($5.667\,03 \times 10^{-8}$ W m^{-2} K^{-4}), T_{sfc} is the surface temperature (K), and L_a and L_e are the longwave radiation flux from the atmosphere and from the multireflection on the other surface. As the first step of validation, we assume that, at the scale of our simulations, the atmosphere between the buildings is transparent and set the absorption coefficient to 0 for both the longwave and shortwave radiation.

3) SURFACE TEMPERATURE MODEL

The force–restore approach (Deardorf 1978) is commonly used to calculate the ground temperature in meteorological models. This approach is considered to be a very useful tool because a prognostic equation for temperature is used to reproduce the response to periodic heating of the soil. This model has been extended to urban surfaces (Johnson et al. 1991; Dupont and Mestayer 2006). This extension nevertheless supposes well-insulated buildings with a nearly constant internal temperature and homogeneous material. In our model, the force–restore method has been available for some time in simple geometries and has been extended to complex geometries. Because of the limiting hypotheses built into the method, however, especially concerning the deep-soil temperature, we have also tested a simple wall thermal model with a given thickness and an average thermal conductivity.

(i) Force–restore model

The force–restore model is based on a two-layer decomposition of a material considered to be homogeneous: the surface-layer temperature T_{sfc} responding to external forcing and the deeper layer independent of the diurnal variation. It reads

$$\frac{\partial T_{\text{sfc}}}{\partial t} = \frac{\sqrt{2\omega}}{\mu}(L^* + S^* - Q_H) - \omega(T_{\text{sfc}} - T_{g/b}), \quad (8)$$

where ω is the Earth angular frequency (Hz), μ is the thermal admittance (J m^{-2} s$^{-0.5}$ K^{-1}), and $T_{g/b}$ is either deep-soil or internal building temperature (K).

(ii) Wall thermal model

This model solves the conduction equation to compute the wall temperature. It reads, after expressing each term in Eq. (1), as

$$\frac{\lambda}{e}(T_{\text{sfc}} - T_{\text{int}}) + h_f(T_{\text{sfc}} - T_a) = \varepsilon(L_a + L_e - \sigma T_{\text{sfc}}^4) + (1 - \alpha)(S_D + S_f + S_e), \quad (9)$$

where λ is the average thermal conductivity of the wall (W K^{-1} m^{-1}), e is the thickness of the wall (m), T_{int} is the internal air temperature (K), h_f is the heat transfer coefficient (W m^{-2} K^{-1}) computed from local flow parameters, and T_a is the external air temperature (K).

4) INTERNAL BUILDING TEMPERATURE

In a real building with good insulation, the variation of the internal building temperature is small. In the experiment we simulate (see section 3), however, the buildings are represented by poorly insulated shipping containers. In this case, the variation of the internal temperature is important and has a great influence on the surface temperature. The internal temperature was not measured in the experiment, however and we computed it with one of the following methods.

(i) Constant T

In this case, the internal building temperature is set to a constant and is computed by averaging the diurnal temperatures of all of the building surfaces.

(ii) Evolution equation

A temperature evolution equation, as in Masson et al. (2002), is used to represent the temperature inside the buildings:

$$T_{\text{int}}^{n+1} = T_{\text{int}}^{n-1}\left(\frac{\tau - \Delta t}{\tau}\right) + \overline{T}\left(\frac{\Delta t}{\tau}\right), \quad (10)$$

where T_{int}^{n+1} and T_{int}^{n-1} are the computed internal temperatures (K) at the following and previous time step, respectively, Δt is the time step (s), τ is the period (equal to 1 day; (s), and $\overline{T}$ is the average over all of the surface temperatures (K) computed at time step n.

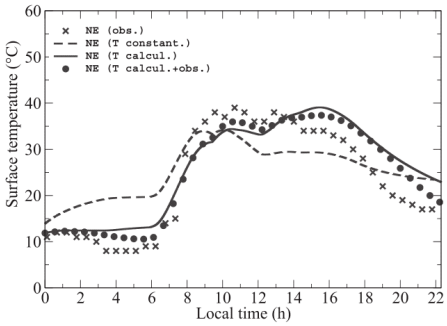

FIG. 2. Comparison of the diurnal evolution of the surface temperature of a northeast-oriented wall computed with three different models for the internal temperature (times signs: surface temperature from the measurements; dashed line: taking a constant internal building temperature; solid line: taking an evolution equation; filled circles: taking the average surface temperature from the measurements and then using the result in the evolution equation).

(iii) Evolution equation with $\overline{T}$ interpolated from measurements

We use the previous formula [Eq. (10)] and replace $\overline{T}$ from the calculation with the average of the measured surface temperatures.

Figure 2 compares the northeast wall surface temperature of a shipping container computed with the three different internal temperature models and the measurements from the Mock Urban Setting Test experiment (see section 3). The value of the constant average internal temperature model is 24°C, which is approximately 2 times the initial values in the other two internal temperature models. Before sunrise, this high value of the constant internal temperature induces a too-rapid heating of the northeast wall. At midday, the constant internal temperature is too low to account for the warming of the surface by the interior air heated by the other sunlit surfaces of the container. Computing the internal temperature with an evolution equation model decreases the heating of the northeast wall before sunrise and improves the results at midday. The differences in the results obtained by using the two evolution equation models (with $\overline{T}$ from computation and $\overline{T}$ from measurements) are small, which was expected because $\Delta t/\tau$ is small. Nevertheless, using the observed average temperature slightly improves the results, especially during the night, when the atmospheric radiative fluxes decrease. The same conclusion applies for the other sides of the containers, which are not shown here. We stress that this may be relevant only in the case of metal containers.

5) CONVECTION MODEL

The thermal energy equation of the flow must be solved, both to determine stratification effects on vertical turbulent transport and to estimate the surface–air thermal gradient that controls convective heat transfer. The sensible heat flux Q_H is given by

$$Q_H = h_f(T_a - T_{\text{sfc}}). \tag{11}$$

Detailed comparisons between different approaches to model the heat transfer coefficient will be discussed in section 5. Our CFD model solves in 3D the RANS equations in the entire fluid domain. In our simulations, we use a rough-wall boundary condition. The h_f is computed for each solid subfacet, depending on the local friction velocity:

$$h_f = \frac{\rho C_p u_* \kappa f_m}{\sigma_t \ln\left(\dfrac{d + z_0}{z_{0_T}}\right)\sqrt{f_h}}, \tag{12}$$

where ρ is flow density (kg m^{-3}), C_p is specific heat (J kg^{-1} K^{-1}), u_* is the friction velocity, κ is the von Kármán constant, σ_t is the turbulent Prandtl number, d is the distance (m) to the wall, z_0 is the roughness length (m), z_{0_T} is the thermal roughness length (m), and f_m and f_h are the Louis (1979) stability functions.

3. Study case: The Mock Urban Setting Test

a. Configuration of the experiment

The Mock Urban Setting Test (MUST; Biltoft 2001; Yee and Biltoft 2004) conducted in the Utah desert is a near-full-scale experiment that consists of measurements in an idealized urban area represented by 120 shipping containers (length L × width W × height H = 12.2 m × 2.42 m × 2.54 m) arranged in a regular array. MUST has already been used to validate dynamics and dispersion models (Brook et al. 2002; Hanna et al. 2002; Camelli et al. 2005; Milliez and Carissimo 2007, 2008). Because temperature data are also provided, we used the MUST field experiment to study in detail the dynamic–radiative coupling. We focused our study on one instrumented container within the array, and therefore the computational domain was reduced to three rows of three containers (Fig. 3).

From the MUST experiment, we selected the day of 25 September 2001. Despite a fairly strong wind (U_{mean} = 7 m s^{-1}), we selected this day because it has already been partly simulated for studies on dispersion (Milliez and Carissimo 2007) and moreover because a complete 24-h dataset for the upstream wind and the surface temperature was available (which was not the case for other days). During this day (Fig. 4), the wind velocity varied from U_{min} = 3 m s^{-1} to U_{max} = 11.5 m s^{-1} and the average diurnal air temperature was about 24°C (measured at 10 m). For our coupling study, the wind speed may be a little high to test strong radiative effects on the airflow, but it emphasizes the convective effects on the surface temperature.

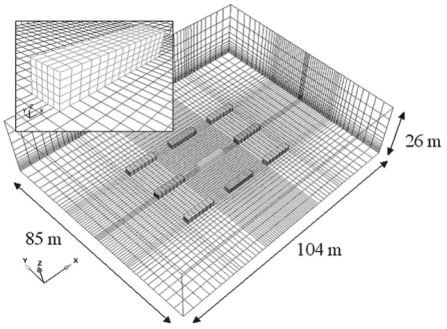

FIG. 3. Mesh of the domain and the subdomain for the 0.8 m × 0.5 m × 0.5 m resolution.

b. Boundary conditions and surface parameters

Table 1 gives the parameters used in the simulation. To be consistent with the experiment, the wind inlet boundary conditions are determined from measurements, using a meteorological file that contains the wind velocity, turbulence kinetic energy, dissipation rate, and temperature profiles for every 2 h. The variation of the deep-soil temperature is neglected. The internal building temperature is computed by the evolution equation with $\overline{T}$ from measurements. We take the same value of the roughness length z_0 as in Eichhorn and Balczo (2008). The thermal roughness length z_{0_T} is considered to be 1/10 of z_0 (Garratt 1992). Because some thermal properties were not determined during the experiment, their values were taken from the literature: we took the values of the albedo and emissivity of the wall to be those of corrugated iron (Oke 1987). The thermal admittance was taken assuming an insulating material in the walls, as observed in some pictures. The ground albedo α_s that was input to the model was evaluated from the incoming and outgoing solar fluxes measured upstream by pyranometers and depends on the zenith angle.

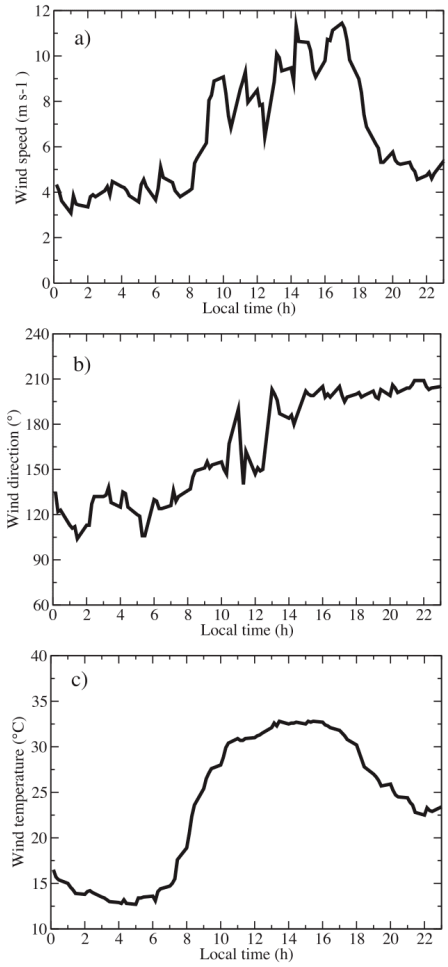

FIG. 4. Meteorological data at 10 m from the MUST experiment for 25 Sep 2001: (a) wind speed (m s^{-1}), (b) meteorological wind direction (°), and (c) wind (air) temperature (°C).

TABLE 1. Parameters employed in the MUST simulations, with Z_{ref} being the reference height for forcing data, U_{ref} being the initial wind speed at Z_{ref}, and θ being the initial wind angle. Soil z_0, wall z_0, and roof z_0 are respectively the roughness length for momentum of soil, walls, and roofs. Soil z_{0_T}, wall z_{0_T}, and roof z_{0_T} are respectively the roughness length for heat of soil, walls, and roofs; α_S, α_W, and α_R are respectively the shortwave albedo of soil, walls, and roofs; ε_S, ε_w, and ε_R are respectively the longwave emissivity of soil, walls, and roofs; μ_S, μ_W, and μ_R are respectively the admittance of soil, walls, and roofs; T_{air} is the initial air temperature at Z_{ref}; T_S and T_{Sint} are respectively the initial soil temperature and deep-soil temperature; T_{Top}, T_{NW}, T_{SE}, T_{NE}, and T_{SW} are initial individual surface temperature; T_{Wint} and T_{Rint} are respectively the building and roof internal temperature.

Parameter	Unit	Value
Dynamic		
Time step	s	0.1
Z_{ref}	m	10
U_{ref}	m s^{-1}	4.27
θ	°	135
Soil z_0	cm	2
Wall z_0 = roof z_0	cm	0.2
Radiative		
Time step	min	5
Soil z_0	cm	0.2
Wall z_{0_T} = roof z_{0_T}	cm	0.02
α_S		From measurements
$\alpha_W = \alpha_R$		0.1
ε_s		0.8
$\varepsilon_w = \varepsilon_R$		0.13
μ_S	J m^{-2} $s^{-0.5}$ K^{-1}	1200
$\mu_W = \mu_R$	J m^{-2} $s^{-0.5}$ K^{-1}	1600
Initial values		
T_{air}	°C	16.45
T_S	°C	15.88
T_{Sint}	°C	24.28
T_{Top}	°C	9.28
T_{NW}	°C	10.50
T_{SE}	°C	11.68
T_{NE}	°C	11.87
T_{SW}	°C	12.37
$T_{Wint} = T_{Rint}$	°C	11.11

c. *Numerical sensitivity*

Before starting our simulations, we performed a numerical sensitivity study for the grid size, the number of directions in the discrete ordinate method, and the radiative time step. We focus here on the radiative aspects because a sensitivity study of the dynamical part has already been performed (Milliez and Carissimo 2007, 2008).

Figure 5 shows surface temperature evolution with grids of different resolutions. The fine (~55 000 cells) and the refined grids (~173 000 cells) give similar results, and the coarse grid (~4000 cells) overestimates or underestimates temperatures, and therefore the fine grid is used in the remaining simulations. Among these three resolutions, we also observe that the coarse grid largely underestimates the southwest surface temperature at about 16 h. The reason is that this surface receives less direct solar flux in the coarse grid than in the fine grid as shown on (Fig. 6). In addition, the thermal boundary layer close to the heated surface may need a sufficient resolution to be captured in such a canopy.

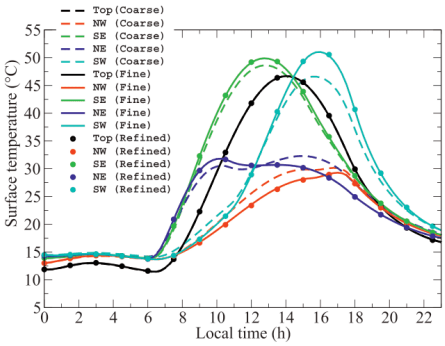

FIG. 5. Surface temperature evolution during a diurnal cycle for different mesh resolutions: dashed lines: coarse grid of ~4000 cells; solid lines: fine grid of ~55 000 cells; filled circles: refined grid about 173 000 cells.

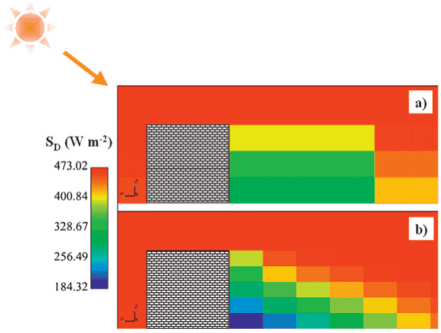

FIG. 6. Vertical cross section of the direct solar flux in the fluid domain around a building at 16 h for different spatial resolutions: (a) coarse grid and (b) fine grid.

Hence, we verified that the fine resolution (0.5 m) in the canopy is enough to reproduce a thermal boundary layer thickness of about 2 m.

In our model, the DOM was implemented with two angular discretizations: 32 or 128 directions, which influence the prediction of the diffuse solar flux and the infrared flux. In this case, the results obtained with 32 directions are very close to the ones with 128 directions, but the calculation is faster by a factor of 5. So we took 32 directions in the remaining simulations. A time step was introduced for the radiative scheme that is different from the one used for the dynamics. We have tested several radiative time steps: 1, 5, 15, and 30 min and 1 h for a diurnal cycle simulation. The resulting difference between a time step of 1 min and 5 min is small, being less than 1°C. We considered that 5 min was an optimum radiative time step for our simulations. The time step for the dynamics was set to 0.1 s after Milliez and Carissimo (2007). The 24-h simulation in parallel computing on a workstation with eight processors took approximately 4.5 days. We have also tested a dynamical time step of 0.5 s, which reduces the computational time to less than 1 day: the results are close to the ones obtained with a dynamical time step of 0.1 s from 0 to 9 h, but after 10 h an important difference (12%–30%) appears when the wind speed exceeds 6 m s^{-1} (Fig. 4). In cases in which the wind speed is small, we could set up the dynamical time step to 0.5 s to reduce significantly the CPU time. The full radiative–dynamic coupling remains computationally expensive, in comparison with simpler models, but at this stage the model is intended for research and not for operational applications.

4. Results

a. *Simulation of 25 September*

Figure 7 shows the evolution of modeled and measured surface temperatures using the force–restore method, with two modeling approaches: 1) radiative only and no convection model (meaning with the convective flux set to zero) and 2) coupled radiative and dynamical model. The diurnal evolutions of the surface temperatures of the top face, southeast face, and northeast face are correctly reproduced by our coupled model. For the northwest face and the southwest face, the simulations show a delay in the morning warming. This delay in warming can be explained by the conduction between the container walls, which contributes to the fast warming in the northwest and southwest faces before they are in the sun but which is neglected in the simulations. In addition, this delay may be inherent to the force–restore method, which overestimates in this case the relaxation to the internal temperature and therefore enhances the thermal inertia. This inertia effect is also observed after sunset for the simulated northwest surface temperature, which shows a delay in cooling. In the afternoon when the atmospheric radiative forcing increases, however, the modeled surface temperatures compare well to the measurements. The comparison with measurements shows a large improvement for the coupled model as compared with the radiative-only model, underlining the importance of accurately including the effect of convection in microscale modeling.

b. *Sensitivity to the surface parameters and surface temperature models*

The values of the surface parameters were taken from the literature. The values for the thermal properties of

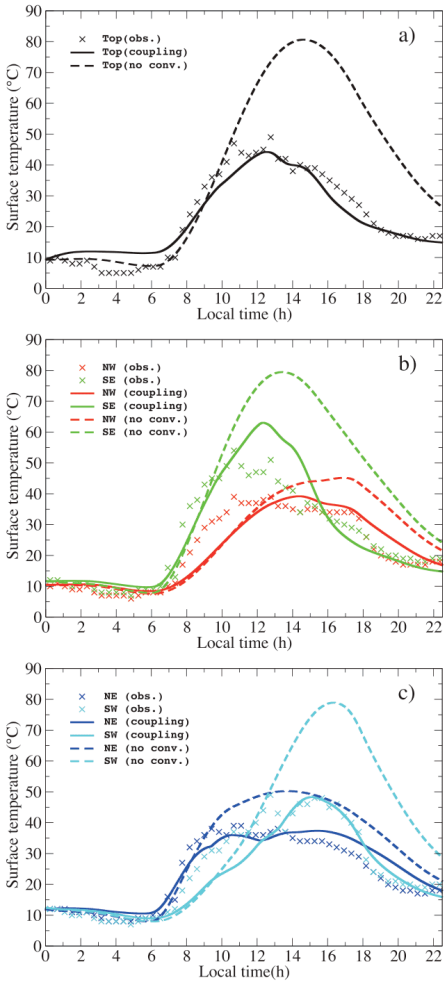

FIG. 7. Evolution of surface temperature of (a) roof (top), (b) northwest, southeast, (c) northeast, and southwest faces modeled using the force–restore method during a diurnal cycle (crosses: measurements; dashed lines: simulation with radiation only; solid lines: simulation with the dynamic–radiative coupling).

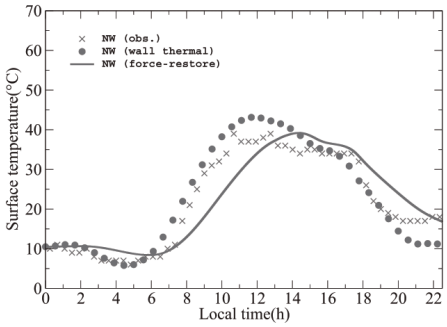

FIG. 8. The northwest wall temperature evolutions obtained with different surface temperature models (crosses: measurements; filled circles: wall thermal model; solid line: force–restore method).

metal cover a wide range (Oke 1987), however, and we performed a sensitivity study of the variation of the surface temperatures when varying the parameters in the range given by the literature. Table 2 illustrates that a change in albedo, emissivity, or admittance, in the range given by the literature, can make a difference of about 1°–10°C for the surface temperature. Because the southeast wall is the most exposed to the sun all day, the deviation of the temperature on this wall is the most important.

The results presented above were obtained by using the force–restore method and are now compared with those obtained with the wall thermal model [see section 2b(3)]. The emissivity was chosen after Oke (1987) for corrugated iron. Because some of the containers in the MUST array were painted, we also made a test taking a much higher emissivity (i.e., 0.9). It results in a decrease in surface temperature. This decrease is greater when using the force–restore method, about 10°C for the southeast wall and 5°C for rest of the walls. For the wall thermal model, the influence of higher emissivity on the surface temperature is less significant, the difference being less than 2°C for all of the faces. This is can be explained the fact that the internal temperature has a greater influence than the other surface parameters. The wall thermal model also requires the characteristics of the surface material and the thickness and the thermal conductivity of the wall which were not provided in the data. When choosing a thermal conductivity of 26 W K^{-1} m^{-1} for the walls, the resulting conduction remains too high, resulting in an homogenization of the temperature of the five walls (not shown here). To improve the comparisons with the observations, we adjusted the value of the conductivity to 6 W K^{-1} m^{-1}, which is not that of pure metal, but may be set by assuming an insulating material in the walls. In Fig. 8, we display the evolution of the northwest wall temperature where we used a conductivity of 6 W K^{-1} m^{-1} and

TABLE 2. Deviation of the surface temperatures (°C) during a diurnal cycle by varying albedo, emissivity, and thermal admittance (J m^{-2} s$^{-0.5}$ K^{-1}), respectively.

Parameter	Variation	Top	Northwest	Southeast	Northeast	Southwest
Albedo	+0.1	−2.6	−1	−4.5	−1.5	−2.3
Emissivity	+0.15	−1.3	−1.2	−3.5	−1	−3.2
Admittance	−400	+1.8	+2	+10.1	+2.6	+2.5

a thickness of 10 cm for the wall and compare it with the observations and that obtained with the force–restore method. In the morning, the wall thermal model (represented by the circles) is able to simulate accurately the increase in the northwest wall surface temperature at 0600 LT, with no delay, as opposed to the force–restore model (represented by the solid line). An overcooling of the surface temperature appears after sunset, however. This overcooling may be explained by a wrong estimation of the internal temperature by the evolution equation, which is highly dependent on the other computed surface temperatures. Another reason could be an overestimation of the mixing by the turbulence scheme, but we expect this deficiency to be weak. Indeed, the turbulence scheme, which takes into account the stability effects, has been extensively used and was previously validated (Buty et al. 1988; Milliez and Carissimo 2008). The wall thermal model seems more adapted to shipping containers than is the force–restore method, however, and a perspective would be to improve the conduction model by, for instance, implementing a multilayer wall model.

5. Discussion: Comparison of three schemes of increasing complexity for predicting surface sensible heat flux

In this section, sensitivity testing is done to compare three schemes used for predicting surface sensible heat flux. The simulated case is based on the MUST geometry with an upstream wind direction of −45°, a reference 10-m wind speed $U_{\text{ref}} = 4$ m s^{-1}, and an initial air temperature of 18°C. The simulation starts at 1200 LT for period of 30 min.

a. Constant h_f model

This scheme is usually used in architecture simulation tools (Miguet and Groleau 2002; Asawa et al. 2008). The radiative model in this type of tool is very accurate, usually using a detailed 3D geometry. The convective model is very simplified, however, and the scheme considers a constant transfer coefficient. For the comparison, we take the constant h_f as the average value on each wall from the 3D convection model that we presented in section 2b(5). Here, we take h_f equal 14.45 W m^{-2} K^{-1} for the roof and 6.12 W m^{-2} K^{-1} for the walls.

In fact, if instead of taking the same constant h_f for all of the walls, we take separate transfer coefficients for each surface (roof 14.45; northwest face 3.94; southeast face 10.78; northeast face 1.38; southwest face 8.35), we can better take into account the orientation of the surface in the wind flow, which decreases the wall surface temperatures by about 2–4 K.

b. One-dimensional h_f model (1D h_f)

In this model employed in TUF-3D (Krayenhoff and Voogt 2007) and similar to the one used in Masson (2000), the transfer coefficient is calculated based on a simple relationship (Martilli et al. 2002):

$$h_f(z) = 11.8 + 4.2u(z) - 4.0, \tag{13}$$

with $u(z)$ being the vertical wind profile within the canopy. Many authors model this wind profile within the canopy with an exponential law (Cionco 1965; Rotach 1995; Krayenhoff and Voogt 2007). For instance, in TUF-3D, Krayenhoff and Voogt (2007) used an iterative way to find a profile of the exponential form with three coefficients. Here, we model the vertical velocity with the exponential profile of Macdonald (2000), which is well adapted to low-density arrays:

$$u(z) = u_H \exp[a(z/H - 1)], \tag{14}$$

where u_H is the mean velocity at the top of the obstacles and the constant a is the attenuation coefficient, which is determined by fitting the average wind profile within the obstacle array.

c. Three-dimensional h_f model (3D h_f)

The full model is three dimensional not only in terms of the radiative exchanges but also the convective exchanges. In this approach, h_f is computed by resolving the 3D RANS and energy equations in the whole fluid domain. Coefficient h_f is calculated for each subfacet depending on the local friction velocity [Eq. (12)], and the sensible heat flux is calculated with the local air temperature [Eq. (11)].

d. Discussion

Figure 9 illustrates the effect of the three convective schemes by visualizing, successively, the transfer

coefficient, the sensible heat flux, and the surface temperature. The three convective schemes show a difference of the sensible flux of approximately 100–240 W m^{-2} for the southeast face and northeast face. With the constant h_f model, the surface temperatures are more homogeneous than in the other two cases. In the MUST configuration, the building array is not dense, and therefore the effects of the shadow and the multireflections are small. That is the reason why the temperatures in the constant h_f approach show little difference within each wall. With the 1D h_f model, we can obviously see the 1D inhomogeneity of the surface temperatures, which is linked to the exponential law wind profile. The 3D h_f model results show the 3D inhomogeneity of the surface temperatures, linked to the inhomogeneity of the 3D wind. On the same face with the same material, we can have a difference of temperature of about 4 K. These results demonstrate the effects of realistically computing the convection fluxes on the surface temperature in the urban areas. Note that in the comparison of the three convective schemes we change only the transfer coefficient and not the air temperature (which is computed for each grid cell of the fluid domain in three dimensions). A simple air temperature model could lead to additional differences.

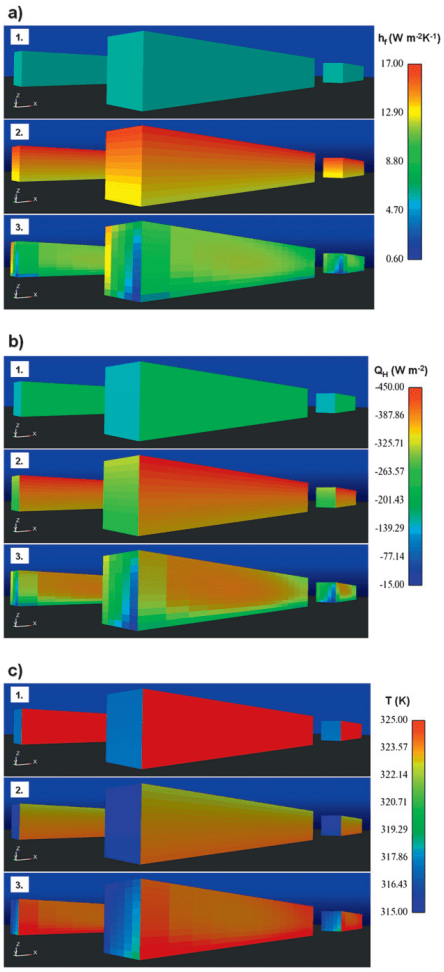

FIG. 9. Comparison of three convective models with visualization of the southeast and northeast walls at 1230 LT: (a) transfer coefficient h_f (W m^{-2} K^{-1}), (b) sensible heat flux Q_H (W m^2), (c) surface temperature T (K). Label 1 indicates the constant h_f model, label 2 is for the 1D h_f model, and label 3 represents the 3D h_f model.

6. Conclusions and perspectives

New atmospheric radiative and thermal schemes were implemented in the atmospheric module of the three-dimensional CFD code known as Code_Saturne. The purpose of this paper was to study in detail the coupling between the radiative scheme and the 3D dynamical model. The model was evaluated with the field measurements from an idealized urban area, the MUST experiment. The coupled model is able to reproduce the evolution of the surface temperatures for different sides of a container within the MUST canopy during a diurnal cycle despite a delay in warming for the northwest and southwest faces at sunrise. The simulations also showed a significant impact of the convective flux on the surface temperatures.

Because the thermal information available in the MUST field is insufficient, sensitivity studies were performed that emphasized the dependence of the model on the parameters describing the building: the properties of the material. In addition, the internal building temperature shows great importance because the buildings are made of metal.

We compared two ways of computing the surface temperature: the force–restore method and a wall thermal model. Because the force–restore method may be more suited for insulated buildings with a near-constant internal temperature (which is not very representative of the MUST containers), we have also tested a one-layer wall model. Using an appropriate evolution equation for the interior buildings, the force–restore shows

good results during the afternoon. It induces a delay in warming at sunset, however, and for the northwest wall a delay in cooling, because of the thermal inertia inherent to the method. The one-layer wall thermal model we tested also show some weakness, since it can reproduce the diurnal cycle of the different surface temperature only with a very low thermal conductivity. Nevertheless, it seems more adapted to model shipping containers than is the force–restore method. One proposed improvement is to implement a multilayer 1D thermal model for the walls, as in Masson (2000) or Krayenhoff and Voogt (2007), which may be more adequate for such surfaces. In fact, shipping-container surface temperatures appear difficult to predict with classical urban models, which for instance do not take into account the conduction between the walls, which can be neglected for real buildings but should not be for metal containers, and a 3D conduction wall model may in this case be necessary.

We also compared our 3D modeling approach to estimate the convective exchanges at the surface (which consists of solving the 3D RANS equations in the whole fluid domain) with two modeling approaches found in the literature: the first approach consists in using a constant heat transfer coefficient, and the second approach is to use a 1D equation based on a vertical wind profile within the canopy. The comparisons are made in terms of the convective transfer coefficients, sensible heat fluxes, and surface temperatures. The three schemes give values of the same order of magnitude for the average surface temperature; nevertheless, only the 3D approach can reproduce the inhomogeneous effect on the wind on a surface: the difference of the same wall can reach 4 K.

The simulation of realistic atmospheric conditions in the urban areas made possible by this work can be used for various applications. A first example is to study pollutant dispersal in a low-wind case. A good description of the heat transfer is essential to describe the convective movement of the air in the streets and is very important for air pollution investigations. A second example is the energy balance of buildings. Estimating the convection fluxes in simple models can keep the computing time low and has application in mesoscale studies; nevertheless, at microscale, it can lead to misleading values in the estimation of the energy loss from the buildings to the atmosphere. In this case, a good prediction of the convective flux can be helpful to the management of the energy consumption and a useful tool in building design. The simulations' results show a significant difference of the parameterizations between taking a simple convection model and describing the physical processes in a realistic way, coupling the 3D dynamics and the radiative processes. The simulations point out the larger difference in surface temperatures at different locations on the same wall.

This study is the first step to validate our dynamic–radiative coupling model. This 3D modeling investigation can bring more detailed information both on radiative and convective fluxes in very local-scale studies. In the MUST case, however, the urban area is idealized. At microscales, small irregularities can break the repeated flow patterns found in a regular array of containers with identical shape. In addition, uncertainties associated with the thickness and the properties of the material of the container wall limit our ability to validate the results. There are also still challenges for modeling in this area. The comparison of three different modeling approaches to estimate the convective exchanges at the surface could be compared with observations if thermal images are available. That is the reason why we will evaluate the coupled dynamic–radiative model on a district of a real urban area with the Canopy and Aerosol Particles Interactions in Toulouse Urban Layer (CAPITOUL) experiment (in the city of Toulouse, France) (Masson et al. 2008; Lagouarde et al. 2010) for which thermal infrared images are available.

Another perspective of this work is to apply the 3D radiative scheme to nontransparent media. Indeed, in many urban applications, the atmosphere between the boundaries can be considered to be transparent and nondiffusive. Nevertheless, when studying smoke dispersion or fog formation and dissipation, absorption and diffusion play an important role. Absorption can already be taken into account by our scheme, and one important perspective of this work is to study radiation in 3D nontransparent media and add the diffusion term in the resolution of the radiative transfer equation.

Acknowledgments. The authors thank the Defense Threat Reduction Agency (DTRA) for providing access to the MUST data.

REFERENCES

Archambeau, F., N. Méchitoua, and M. Sakiz, 2003: Code_Saturne: A finite volume code for the computation of turbulent incompressible flows—Industrial applications. *Int. J. Finite Vol.,* **1,** 1–62.

Arnfield, A. J., 2003: Two decades of urban climate research: A review of turbulence, exchanges of energy and water, and the urban heat island. *Int. J. Climatol.,* **23,** 1–26.

Asawa, T., A. Hoyano, and K. Nakaohkubo, 2008: Thermal design tool for outdoor space based on a numerical simulation system using 3D-CAD. *Build. Environ.,* **43,** 2112–2123.

Biltoft, C. A., 2001: Customer report for Mock Urban Setting Test. West Desert Test Center, U.S. Army Dugway Proving Ground, DPG Doc. WDTC-FR-01-121, 58 pp.

Brook, D. R., N. V. Beck, C. M. Clem, D. C. Strickland, I. H. Griffits, D. J. Hall, R. D. Kingdon, and J. M. Hargrave, 2002: Validation of the Urban Dispersion Model (UDM). *Proc. Eighth Int. Conf. on Harmonisation within Atmospheric Dispersion Modelling for Regulatory Purposes,* Sofia, Bulgaria, National Institute of Meteorology and Hydrology of Bulgaria, 8–12.

Buty, D., J. Y. Caneill, and B. Carissimo, 1988: Simulation numerique de la couche limite atmospherique en terrain complexe au moyen d'un modele mesometeorologique non hydrostatique: Le code mercure (Numerical simulation of the atmospheric boundary layer in complex terrain by means of a nonhydrostatic model: The Mercury code). *J. Theor. Appl. Mech.,* **7,** 35–62.

Camelli, F. E., R. Lohner, and S. R. Hanna, 2005: VLES study of MUST experiment. *Proc. 43rd AIAA Aerospace Sciences Meeting and Exhibit,* Reno, Nevada, American Institute of Aeronautics and Astronautics, 1–19.

Cionco, R. M., 1965: A mathematical model for air flow in a vegetative canopy. *J. Appl. Meteor.,* **4,** 517–522.

Deardorf, J. W., 1978: Efficient prediction of ground surface temperature and moisture with inclusion of a layer of vegetation. *J. Geophys. Res.,* **83,** 1889–1903.

Dupont, S., and P. Mestayer, 2006: Parameterization of the urban energy budget with the submesoscale soil model. *J. Appl. Meteor. Climatol.,* **45,** 1744–1765.

Eichhorn, J., and M. Balczo, 2008: Flow and dispersal simulations of the Mock Urban Setting Test. *Proc. 12th Int. Conf. on Harmonisation within Atmospheric Dispersion Modelling for Regulatory Purposes,* Cavtat, Croatia, Meteorological and Hydrological Service of Croatia, 67–72.

Fiveland, W. A., 1984: Discrete-ordinates solutions of the radiative transport equation for rectangular enclosure. *J. Heat Transfer,* **106,** 699–706.

Garratt, J. R., 1992: *The Atmospheric Boundary Layer*. Cambridge University Press, 316 pp.

Gastellu-Etchegorry, J., 2008: 3D modeling of satellite spectral images, radiation budget and energy budget of urban landscapes. *Meteor. Atmos. Phys.,* **102,** 187–207.

——, E. Martin, and F. Gascon, 2004: DART: A 3-D model for simulating satellite images and surface radiation budget. *Int. J. Remote Sens.,* **25,** 75–96.

Grimmond, C. S. B., and T. R. Oke, 1999: Heat storage in urban areas: Local-scale observations and evaluation of a simple model. *J. Appl. Meteor.,* **38,** 922–940.

Hanna, S. R., S. Tehranian, B. Carissimo, R. W. Macdonald, and R. Lohner, 2002: Comparisons of model simulations with observations of mean flow and turbulence within simple obstacle arrays. *Atmos. Environ.,* **36,** 5067–5079.

Johnson, G. T., T. R. Oke, T. J. Lyons, D. G. Steyn, I. D. Watson, and J. A. Voogt, 1991: Simulation of surface urban heat islands under 'ideal' conditions at night. Part I: Theory and tests against field data. *Bound.-Layer Meteor.,* **56,** 275–294.

Kanda, M., T. Kawai, M. Kanega, R. Moriwaki, K. Narita, and A. Hagishima, 2005: A simple energy balance model for regular building arrays. *Bound.-Layer Meteor.,* **116,** 423–443.

Krayenhoff, E. S., and J. A. Voogt, 2007: A microscale three-dimensional urban energy balance model for studying surface temperatures. *Bound.-Layer Meteor.,* **123,** 433–461.

Lagouarde, J. P., A. Hénon, B. Kurz, P. Moreau, M. Irvine, J. Voogt, and P. Mestayer, 2010: Modelling daytime thermal infrared directional anisotropy over Toulouse city centre. *Remote Sens. Environ.,* **114,** 87–105.

Lemonsu, A., C. S. B. Grimmond, and V. Masson, 2004: Modelling the surface energy balance of an old Mediterranean city core. *J. Appl. Meteor.,* **43,** 312–327.

Liu, J., H. M. Shang, and Y. S. Chen, 2000: Development of an unstructured radiation model applicable for two-dimensional planar, axisymmetric, and three-dimensional geometries. *J. Heat Transfer,* **66,** 17–33.

Louis, J., 1979: A parametric model of vertical eddy fluxes in the atmosphere. *Bound.-Layer Meteor.,* **17,** 187–202.

Macdonald, R. W., 2000: Modelling the mean velocity profile in the urban canopy layer. *Bound.-Layer Meteor.,* **197,** 25–45.

Martilli, A., A. Clappier, and M. W. Rotach, 2002: An urban surface exchange parameterisation for mesoscale models. *Bound.-Layer Meteor.,* **104,** 261–304.

Masson, V., 2000: A physically based scheme for the urban energy budget in atmospheric models. *Bound.-Layer Meteor.,* **94,** 357–397.

——, C. S. B. Grimmond, and T. R. Oke, 2002: Evaluation of the Town Energy Balance (TEB) scheme with direct measurements from dry districts in two cities. *J. Appl. Meteor.,* **41,** 1011–1026.

——, and Coauthors, 2008: The Canopy and Aerosol Particles Interactions in Toulouse Urban Layer (CAPITOUL) experiment. *Meteor. Atmos. Phys.,* **102,** 135–157.

Miguet, F., and D. Groleau, 2002: A daylight simulation tool for urban and architectural spaces—Application to transmitted direct and diffuse light through glazing. *Build. Environ.,* **37,** 833–843.

Milliez, M., 2006: Modélisation micro-météorologique en milieu urbain: Dispersion des polluants et prise en compte des effets radiatifs (Micrometeorological modeling in urban environment. Dispersion of pollutants and the taking into account of radiative effects). Ph.D. thesis, École des Ponts ParisTech, 228 pp. [Available online at http://cerea.enpc.fr/fich/these_milliez.pdf.]

——, and B. Carissimo, 2007: Numerical simulations of pollutant dispersion in an idealized urban area, for different meteorological conditions. *Bound.-Layer Meteor.,* **122,** 321–342.

——, and ——, 2008: CFD modelling of concentration fluctuations in an idealized urban area, for different meteorological conditions. *Bound.-Layer Meteor.,* **127,** 241–259.

——, L. Musson-Genon, and B. Carissimo, 2006: Validation of a radiative scheme for CFD modelling of heat transfers between buildings and flow in urban canopies. Preprints, *Sixth Int. Conf. on Urban Climate,* Göteborg, Sweden, International Association of Urban Climate, 266–269.

Mills, G., 1996: An urban canopy-layer climate model. *Theor. Appl. Climatol.,* **1997,** 229–244.

Oke, T. R., 1987: *Boundary Layer Climates*. 2nd ed. Routledge, 435 pp.

Rotach, M. W., 1995: Profiles of turbulence statistics in and above an urban street canyon. *Atmos. Environ.,* **29,** 1473–1486.

Truelove, J. S., 1987: Discrete-ordinates solutions of the radiative transport equation. *J. Heat Transfer,* **109,** 1048–1051.

Yee, E., and C. A. Biltoft, 2004: Concentration fluctuations measurements in a plume dispersing through a regular array of obstacles. *Bound.-Layer Meteor.,* **111,** 363–415.

2.2.3. Étude des effets thermiques des bâtiments par vent faible

J'ai testé deux approches différentes pour modéliser les échanges radiatifs en milieu urbain avec une comparaison entre le Code_Saturne et SOLENE. SOLENE a été conçu pour s'intéresser aux outils de conception de l'architecte dans le domaine de l'ajustement climatique et thermique (**Miguet & Groleau, 2002).** Les résultats montrent que les deux modèles sont en bon accord pour prédire l'évolution temporelle du rayonnement solaire direct, du rayonnement infra-rouge incident et la température de surface.

Ensuite, j'ai montré l'apport du modèle de transfert radiatif sur l'écoulement de l'air dans des conditions de faible vitesse du vent dans une canopée 3D. Dans l'article qui suit, les résultats montrent que la prise en compte de la stratification thermique a une forte influence sur le champ de vent (**Qu et al. 2012**).

Référence:

Qu, Y., M. Milliez, L. Musson-Genon and B. Carissimo, 2012: Numerical study of the thermal effects of buildings on low-speed airflow taking into account 3D atmospheric radiation in urban canopy, J. Wind Eng. Ind. Aerodyn. (104–106), 474–483. doi: http://dx.doi.org/10.1016/j.jweia.2012.03.008

J. Wind Eng. Ind. Aerodyn. 104-106 (2012) 474–483

Contents lists available at SciVerse ScienceDirect

Journal of Wind Engineering and Industrial Aerodynamics

journal homepage: www.elsevier.com/locate/jweia

Numerical study of the thermal effects of buildings on low-speed airflow taking into account 3D atmospheric radiation in urban canopy

Yongfeng Qu [1,*], Maya Milliez, Luc Musson-Genon, Bertrand Carissimo

CEREA, 6-8 avenue Blaise Pascal, 77455 Champs-sur-Marne, France

ARTICLE INFO

Available online 21 March 2012

Keywords:
Thermal transfer
3D atmospheric radiation
Computational Fluid Dynamics
Urban canopy
Coupling

ABSTRACT

A three-dimensional atmospheric radiative model which evaluates the thermal-radiative transfers in the lower atmosphere was implemented in the atmospheric module of a Computational Fluid Dynamics code. This model can study the thermal effects of buildings on the local atmospheric flow with a coupled dynamic-radiative model. Previously, we have validated this approach and discussed the impact of the convective flux on the surface temperatures by comparing a detailed wind and temperature field with the Mock Urban Setting Test (MUST) experiment dataset. In this paper our objective is to demonstrate the ability of our radiative model to simulate the thermal effect of buildings on the local atmospheric flow under low wind speed condition. Therefore, we present different numerical simulations for low wind speed and higher building density than in MUST, comparing the neutral case with different levels of thermal exchange model and analyzing the differences. The results show first that taking into account the thermal stratification has a significant influence on the wind field. Then we show that the difference between the case for which we impose the temperatures and the case with temperatures calculated with a 3D radiative transfer scheme can also be important near the buildings. In addition, with the 3D radiative model, the temperature and vertical motion show an important sensitivity to changes in the physical parameters of the wall surfaces, such as the surface albedo.

1. Introduction

The influence, on the airflow pattern, of the incident atmospheric radiation on the canyon walls and ground surfaces under conditions of low wind speed can be important and should not be neglected in pollutant dispersion or urban design studies. Solar heating of the building walls and the ground during the day warms the air near the wall or above the ground, which can cause strong thermally induced air motion. This thermal effects on the airflow, including building geometry and architecture as well as street canyon dimensions, have been mainly studied with wind-tunnel experiments (Uehara et al., 2000; Kovar-Panskus et al., 2002; Richards et al., 2006) and numerical models (Sini et al., 1996; Kim and Baik, 2001; Louka et al., 2001; Xie et al., 2007) and fewer with full-scale or near full-scale experiments (Louka et al., 2001; Kanda, 2006; Niachou et al., 2008). In general, field and wind-tunnel experimentalists stress the technical difficulties in controlling air and surface temperatures and various air or surface temperatures gradients. Moreover, in order to obtain significant thermal effects and respect the similarity with a real building, a very high surface temperature (100−400 °C) has to be applied in wind-tunnel experiments (Uehara et al., 2000; Kovar-Panskus et al., 2002; Richards et al., 2006).

To overcome this limitation, numerical studies were performed. Sini et al. (1996) first numerically showed that the thermal forcing could markedly influence the air motions and the wind structure. Later, Kim and Baik (2001) simulated the flow in an urban street canyon with various aspect ratios and with street bottom heating using a two-dimensional (2D) Computational Fluid Dynamics (CFD) model with a *k-epsilon* turbulence closure. Kovar-Panskus et al. (2002) identified the differences in the airflow regimes between the cases with and without wall heating. Xie et al. (2007) investigated the influence of the multi-surface heating configuration on the flow field and pollutant transport problems with the wind-tunnel experiment of Uehara et al. (2000).

However, most of the previous research works considered a 2D computational domain and assumed idealized sunlit wall configurations (uniform sunlight on one surface of the canyon and no sunlight on any other solid surfaces) without including a realistic radiative model. Further research work is therefore necessary to improve our knowledge about the thermal effects on local atmospheric environment. On the basis of this background, the aim of this work is to perform three-dimensional (3D) numerical

* Corresponding author. Tel.: +33 130877217.
E-mail address: yongfeng.qu@cerea.enpc.fr (Y. Qu).
[1] CEREA Teaching and Research Center in Atmospheric Environment (Ecole des Ponts ParisTech/EDF R&D).

0167-6105/$ - see front matter Crown Copyright © 2012 Published by Elsevier Ltd. All rights reserved.
doi:10.1016/j.jweia.2012.03.008

Nomenclature

Superscripts

↓	incoming
↑	outgoing (–)

Subscripts

int	internal building or deep soil
ref	reference height (–)
sfc	external surface (–)

Roman symbols

C_p	specific heat (J kg^{-1} K^{-1})
d	distance of the cell center to the wall (m)
e	wall thickness (m)
epsilon	dissipation rate (–)
f_m, f_h	Louis stability functions (–)
L	long-wave radiative flux (W m^{-2})
L_a	long-wave radiative flux from the sky (W m^{-2})
L_e	long-wave radiative flux from the multi-reflection on the other surfaces (W m^{-2})
h_f	heat transfer coefficient (W m^{-2} K^{-1})
k_{ref}	turbulent energy (m^2 s^{-2})
Q_{cond}	conductive heat flux (W m^{-2})
Q_H	sensible heat flux (W m^{-2})
Q^*	net radiation flux (W m^{-2})
S	short-wave radiative flux (W m^{-2})
S_D	direct solar flux (W m^{-2})
S_e	solar flux diffused by the environment (W m^{-2})
S_f	solar flux diffused by the atmosphere above (W m^{-2})
T	temperature (K, °C)
T_a	air temperature (K, °C)
u_*	friction velocity (m s^{-1})
U	wind speed (m s^{-1})
z_0	aerodynamic roughness length (m)
z_{0_T}	thermal roughness length (m)
Z	vertical height (m)

Greek symbols

α	albedo of the surface (–)
ε	emissivity of the surface (–)
σ	Stefan–Boltzmann constant (5.66703×10^{-8} W m^{-2} K^{-4})
σ_t	turbulent Prandtl number (–)
ρ	flow density (kg m^{-3})
κ	von Kármán constant (–)
λ	average thermal conductivity (W m^{-1} K^{-1})
θ	potential temperature (K, °C)

simulations in order to evaluate the effects of non-uniform wall-heating on the airflow pattern using a 3D radiative model developed in the CFD code *Code_Saturne* (Archambeau et al., 2003) which is adapted to complex geometry. Milliez (2006) first evaluated the model with idealized cases, using a constant 3D wind field. Then, Qu et al. (2011) validated the full radiative–convective coupling through a comparison with observation datasets from Mock Urban Setting Test (MUST) field campaign (Yee and Biltoft, 2004; Milliez and Carissimo, 2007, 2008). The model successfully simulates a key parameter in the surface energy balance (SEB), the surface temperature, for different sides of a container within the MUST canopy in a diurnal cycle. In the same paper, they have also discussed the influence on the surface temperatures of the internal building temperature and the wall thermal modeling, and compared the 3D modeling of the convective exchanges to simpler approaches used in other models. Later, based on MUST full radiative–convective validation, the atmospheric radiation model in *Code_Saturne* is well-tested through the atmospheric radiation fluxes and the container walls surface temperature to achieve the objective of comparison with the geometric view factor approach (Qu, 2011, Chapter 4), used by the SOLENE model (Miguet and Groleau, 2002).

In this paper, in order to assess the thermal impact on the flow field in different thermal conditions, we extend the work of Qu et al. (2011) and Qu (2011) to lower wind speed and a higher building density than in MUST. First, we briefly describe the model and discuss the thermal exchange modeling of buildings. Then we present different numerical simulations for low wind speed in this idealized urban area with a high building density, varying the thermal exchange model and analyzing the differences.

2. Equations and model design

The model used in this study is the open-source CFD code *Code_Saturne* which can handle complex geometry and physics. Taking into account the larger scale meteorological conditions and the thermal stratification of the atmosphere, the atmospheric module of *Code_Saturne*, described in Milliez and Carissimo (2007, 2008), uses a detailed representation of the surfaces allowing a complex 3D spatial representation of wind speed, turbulence, and temperature. The numerical solver employs a finite-volume approach for co-located variables on an unstructured mesh. Time discretization is achieved through a fractional step scheme, with a prediction–correction step. In our simulations with *Code_Saturne*, we keep a standard residual value (10^{-9}) and check the convergence of the solution with monitoring points. When the thermal effects are taken into account in this low wind speed case, using a center scheme happens to create numerical instabilities, especially in the inflow region, thus an upwind scheme is used.

2.1. Turbulence model k-epsilon

Although Reynolds-Averaged Navier–Stokes (RANS) is less accurate in comparison to Large Eddy Simulation (LES), RANS is the most commonly used CFD methodology for the simulation of turbulent flows encountered in industrial and engineering applications because of its computational efficiency. In our simulations, the turbulence in the entire fluid domain is parameterized by the standard *k-epsilon* formulation as in our previous work (Qu et al., 2011). A comparison between LES and RANS computations for the study of contaminant dispersion in the presence of buildings in the MUST field experiment has been assessed by Santiago et al. (2010). Globally, the results obtained with LES and RANS for the spatially averaged flow properties were found to be similar for each flow configuration considered and only slight differences were observed in their cases studied (LES in regular and irregular obstacle arrays, and RANS in regular and irregular obstacle arrays). LES captured better the irregularity effects observed on the vertical velocity components. The magnitude of this velocity component is in general underestimated by RANS. At the microscale level, small irregularities are shown to affect

significantly the mean vertical velocity component while the mean streamwise velocity and Reynolds shear stress are shown to be less sensitive to small geometrical perturbations. However, for the mean streamwise velocity and Reynolds shear stress, the LES results are found to be close to RANS results and both approaches were in satisfactory agreement with the observations.

As also stressed in Milliez and Carissimo (2008), stability effects inside urban canopies should not be neglected. The turbulence model we use, accounts for atmospheric stratification through the production and destruction of turbulent kinetic energy and dissipation. Buoyancy is also taken into account in the momentum equations.

2.2. Surface energy balance

To take into account the thermal effects of buildings, we model the surface energy balance (SEB). In this study, we neglect the anthropogenic heat flux and the latent heat flux. The advection fluxes are obtained by the resolution of the entire flow field. Thus, for each surface the SEB is expressed as

$$Q_{cond} + Q_H = Q^*, \tag{1}$$

where Q_{cond} is the conductive heat flux ($W\,m^{-2}$) within the building or the ground subsurface, which links the surface temperature to the internal building or the deep soil temperature, Q_H is the sensible heat flux ($W\,m^{-2}$) which depends on the local airflow intensity, Q^* is the net radiative flux ($W\,m^{-2}$).

2.3. Radiative model: Q^*

2.3.1. Solar and infrared radiation

The net atmospheric radiation Q^* is the net or resultant value of the short- and long-wave radiation. The total incoming and outgoing short-wave radiative fluxes for each solid surface are expressed as

$$S^{\downarrow} = S_D + S_f + S_e, \tag{2}$$

$$S^{\uparrow} = \alpha S^{\downarrow}, \tag{3}$$

where $S^{\downarrow}$ and $S^{\uparrow}$ are respectively the incoming and outgoing short-wave radiative fluxes ($W\,m^{-2}$), S_D is the direct solar flux ($W\,m^{-2}$), S_f is the solar flux diffused by the atmosphere above our simulation domain ($W\,m^{-2}$), S_e is the flux diffused by the environment, i.e. resulting from the multi-reflections on the other sub-facets ($W\,m^{-2}$) and α is the albedo of the surface.

Then, the long-wave radiation flux for each surface reads

$$L^{\downarrow} = L_a + L_e, \tag{4}$$

$$L^{\uparrow} = \varepsilon\sigma T_{sfc}^4 + (1-\varepsilon)(L_a + L_e), \tag{5}$$

where $L^{\downarrow}$ and $L^{\uparrow}$ are respectively the incoming and outgoing long-wave radiative fluxes ($W\,m^{-2}$), ε is the emissivity of the surface, σ is the Stefan–Boltzmann constant ($5.66703 \times 10^{-8}\,W\,m^{-2}\,K^{-4}$), T_{sfc} (K) is the surface temperature, L_a ($W\,m^{-2}$) and L_e ($W\,m^{-2}$) are respectively the long-wave radiation flux from the atmosphere and from the multi-reflection on the other surfaces.

2.3.2. Discrete Ordinate Method (DOM)

The radiative fluxes are computed using the Discrete Ordinate Method (DOM) (Fiveland, 1984; Truelove, 1987; Liu et al., 2000) which solves the radiative transfer equation for a gray non-diffusive semi-transparent media by the directional propagation of the radiative wave. In our models, the angular discretization has two resolutions: 32 or 128 directions and the spatial discretization uses the same mesh as the CFD model. Taking into account both short- and long-wave radiation separately, we have adapted a radiative heat transfer scheme available for combustion in *Code_Saturne*. Described in detail by Milliez (2006), the new atmospheric 3D radiative approach was developed in *Code_Saturne* for built-up areas. The main advantage of this model is that the radiative transfer equations is solved in the whole fluid domain and not only at solid faces (such as when using view factors), but also can be applied to non-transparent media (e.g. fog or pollution). In this work, we consider a transparent atmosphere between the building at the microscale of our simulations.

2.4. Wall law and convective model

In our simulations, momentum and heat transfer from horizontal surfaces follow a rough wall logarithmic law modified by stratification. Usually these modified laws are based on the Monin–Obukov similarity but are implicit and therefore need to be solved iteratively. Here we use an explicit approach based on the work of Louis (1979) and described in Musson-Genon et al. (2007). Convection from vertical surfaces defaults to the neutral wall law.

With this scheme, the sensible heat flux Q_H term in Eq. (1) is calculated from

$$Q_H = h_f(T_a - T_{sfc}), \tag{6}$$

with T_a(K) is the external air temperature.

The local heat transfer coefficient h_f ($W\,m^{-2}\,K^{-1}$) for each solid sub-facet in the equation (6) is defined here as

$$h_f = \frac{\rho C_p u_* \kappa f_h}{\sigma_t \ln\left(\frac{d+z_0}{z_{0_T}}\right)\sqrt{f_m}}, \tag{7}$$

where ρ is the flow density ($kg\,m^{-3}$), C_p is the specific heat ($J\,kg^{-1}\,K^{-1}$), κ is the von Kármán constant, σ_t is the turbulent Prandtl number, d is the distance (m) to the wall, z_0 is the roughness length (m), z_{0_T} is the thermal roughness length (m), f_m and f_h are the Louis (1979) stability dependent surface layer functions.

The friction velocity u_* ($m\,s^{-1}$) in Eq. (7) is obtained as follows:

$$u_* = U(Z=d)\frac{\kappa}{\ln\left(\frac{d+z_0}{z_0}\right)}\sqrt{f_m}, \tag{8}$$

where U is the wind speed ($m\,s^{-1}$).

In neutral conditions, we have $f_m = f_h = 1$ and $Q_H = 0$. In that case, the u_* estimated from Eq. (8) is exactly the equilibrium law discussed by Richards and Hoxey (1993). We have verified that the wind and turbulence profiles are maintained in flat terrain to a good accuracy, and we do not experience the difficulties mentioned in Blocken et al. (2007) for codes that we use a wall law based on sand-grain roughness, without a displacement height.

2.5. Modeling surface temperature: wall thermal model Q_{cond}

As shown in Eq. (1), the solution of the surface energy balance for each surface cell at each time step requires the calculation of the heat conduction (Q_{cond}) which links the internal temperature to the surface temperature. Conduction between surface layers spatially varying in thickness e (m) and thermal conductivity λ ($W\,K^{-1}\,m^{-1}$), as typical for building walls, necessitates a sophisticated approach. Yet, the simulations are short-term in this study. So we adopted one-dimensional conduction scheme with an average thermal conductivity of the wall and a constant value to the internal building temperature T_{int} (K). Hence, the solution for the surface

temperature is calculated from

$$\frac{\lambda}{e}(T_{sfc}-T_{int})+h_f(T_{sfc}-T_a)=\varepsilon(L_a+L_e-\sigma T_{sfc}^4)+(1-\alpha)(S_D+S_f+S_e), \quad (9)$$

where the heat transfer coefficient h_f is computed from local flow parameters as shown in Eq. (7).

3. Numerical simulations set-up

3.1. Initial and boundary conditions

The computational domain is three-dimensional and the boundaries are positioned far or high enough from the built-up area of interest (10*H* as shown in Fig. 1a). A Dirichlet boundary condition is applied at the inlet (East in Fig. 1a). For the top boundary, we consider a constant shear stress, corresponding to the inflow profiles in order to prevent a horizontal change from the inflow profiles. As frequently done in CFD codes, we use the symmetry boundary conditions at the lateral boundaries (North and South in Fig. 1a) since the approach inflow direction is parallel to them. At the outlet boundary (West in Fig. 1a), we apply the free outflow condition. Thus, the derivatives of all flow variables are forced to zero.

The buildings have the same dimensions ($L\times W\times H$: 12.2 m × 2.42 m × 2.54 m) as the MUST experiment shipping containers (Yee and Biltoft, 2004; Milliez and Carissimo, 2007; Qu et al., 2011) and the orientation of the *x*-axis is pointing towards the geographic north. In addition, we modified the aspect ratio (*H*/*W*, where *H* is the building height and *W* is the along-wind spacing) to 1 in order to increase the density of the urban canopy and therefore to emphasize the thermal impact on the wind. The run takes place from 0900 LST to 0910 LST. At this time, the Sun position is on the East side of the domain as shown in Fig. 1a. The meteorological initial and inlet boundary conditions are a neutrally stratified logarithmic wind profile blowing westward, associated with a neutral potential temperature profile of 30 °C with both dynamical and thermal roughness lengths set to 4 cm. Since the thermal effects are expected to be of substantial importance for low wind speeds, certainly below 3 m s^{-1} when the urban dome regime dominates (Oke, 1987; Kovar-Panskus et al., 2002), the 10 m high wind speed is set to 1 m s^{-1}. Low wind conditions and large surface-air temperature differences cause large thermal effects. Different differential temperatures between the heated surfaces and the air were simulated in numerical studies (5 °C in Sini et al., 1996, 10 °C in Xie et al., 2007, 32 °C between the windward wall and the air, 53 °C between the leeward wall and the air in Onomura et al., 2009). In general, a surface-air temperature difference of 5–10 °C is considered to be close to the one of a wall heated by solar radiation. Thus, in our study, the initial air, soil and wall/roof temperatures are set to 30, 32 and 36 °C, respectively.

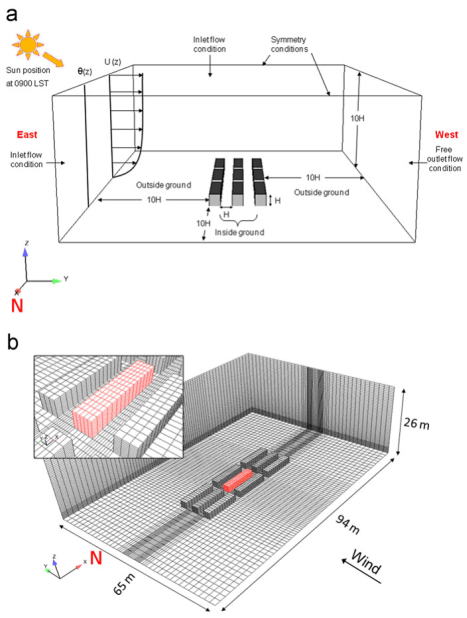

Fig. 1. Computational domain with building models for low wind speed: (a) simulations-definition of boundary conditions; (b) mesh of the domain and sub-domain. The north is indicated.

In order to study the contribution of atmospheric radiation on the airflow, we simulated three cases: a reference case without heat transfer, i.e. with a neutral stratification of the atmosphere—called hereafter "neutral case", a case with heat transfer but where the surface temperatures are imposed—called hereafter "imposed temperatures case", and a case with the 3D atmospheric radiative model coupled to the dynamical one—called hereafter "radiative transfer case".

For the second case, the imposed wall/roof temperature is set to the one used to initialize the surface temperatures in the radiative transfer case (36 °C). For the ground, two imposed temperatures are used, which are obtained by averaging the results of the radiative transfer case: one (lower) for the ground inside the canyons (11.30 °C) (in order to take into account the shading effects) and another one for the area outside the array (35.15 °C).

In the two last cases, a buffer zone is included to remove any numerical perturbation due to the difference between the ground-level temperature of the inlet meteorological profile and the imposed or initial ground temperature inside the domain. The numerical simulation features including initial and wall boundary conditions are summarized in Table 1.

3.2. Mesh resolution

The mesh with sufficient resolution plays a direct role in the quality of the simulations. Based on the unstructured hexahedral grid used in Qu et al. (2011), we have increased the grid resolution in this work as shown in Fig. 1b. We have followed the guideline from Franke et al. (2007) and the minimum grid resolution is set to 1/10 of the building height scale (0.25 m) within the regions of high gradients. In order to keep the truncation error small, an expansion ratio of 1.2 is set for the grid stretching/compression. Thus, the mesh generated in this work has total about 250,000 cells (Table 1). After a sensitivity study, the time-steps for the dynamical model and the radiative one were respectively set to 0.05 s and 2 min.

4. Results and discussion

The numerical simulation results are analyzed at $t=600$ s, when the mean flows in the entire simulated urban canopy

Table 1
Boundary conditions and parameters used in the low wind speed simulations.

Domain dimensions	$52(x)$ m × $93.68(y)$ m × $26.54(z)$ m
Unstructured hexahedral grid resolution	Total 253,943 cells $x_{min}=0.81$ m, $x_{max}=1.90$ m $y_{min}=0.48$ m, $y_{max}=1.90$ m $z_{min}=0.23$ m, $z_{max}=0.68$ m
Inlet boundary conditions	Time-step 0.05 s, reference height $Z_{ref}=10$ m Initial wind speed $U_{ref}=1.0$ m s^{-1}, wind direction relative to the north $-90°$ $k=1.88\times10^{-2}$ m^2 s^{-2}, $epsilon=1.01\times10^{-4}$ Dynamical roughness for soil $z_0=4$ cm, for wall and roof $z_0=2$ cm
Thermal boundary conditions	Thermal roughness z_{0_t} for soil, wall and roof as same as dynamical roughness z_0 Initial potential temperature $\theta=30$ °C
For the imposed temperatures case	Outside/inside ground temperature $T_{sfc}=35.15/11.30$ °C
For both the imposed temperatures and the radiative transfer cases	Initial walls and roofs temperature $T_{sfc}=36$ °C
Additional boundary conditions for the radiative transfer cases	Radiative time-step 120 s
For the soil	Albedo $\alpha=0.53$, emissivity $\varepsilon=0.8$ Conductivity $\lambda=0.75$ W K^{-1} m^{-1}, thickness $e=50$ cm Deep-soil temperature $T_{int}=25$ °C
For the walls and roofs	Albedo $\alpha=0.1$, emissivity $\varepsilon=0.13$ Conductivity $\lambda=6$ W K^{-1} m^{-1}, thickness $e=10$ cm Internal temperature $T_{int}=32$ °C

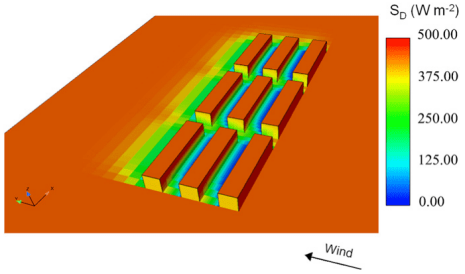

Fig. 2. Visualization of the direct solar flux (S_D) (W m^{-2}) received by the surfaces with a 0900 LST sun position from the radiative model.

reaches a quasi-steady state. Fig. 2 presents at 0900 LST the direct solar flux received by the surfaces from the radiative model. We observe that the distribution of the shadow in the canyons is mainly behind the leeward walls and the most heated walls are at windward sides.

4.1. Comparison of three thermal conditions: neutral, imposed temperatures and 3D radiative transfer cases

Fig. 3a and b shows the mean Turbulent Kinetic Energy (TKE) fields at roof level and half building height level for three thermal conditions. In all conditions, due to the presence of the buildings creating mechanically induced turbulence, more TKE is found at roof level than in the canopy. Compared to the neutral case (Fig. 3a1 and b1), the presence of heat transfer (Fig. 3a2, a3, b2, b3) enhances the TKE in the whole domain due to a large thermal production, in particular near the windward side of the first array (the most heated wall) and in the wake zone (accumulated thermal production). Similar TKE distributions in the street canyons are found in the two cases with heat transfer (Fig. 3a2, a3, b2, b3) due to surface temperatures on the same order of magnitude, generating similar thermal production. However, the non-uniform surface heating in the radiative transfer case shows an asymmetry in the TKE distribution. This asymmetry obviously shows smaller values in the center and larger values on the right side of the wake zone.

The asymmetrical TKE distribution and the larger TKE in the wake zone can be better understood by looking at the dominating vortex structure in the cross-section $5H$ behind the array, as shown in Fig. 4. Consistent with Fig. 3a, three different vortex regimes are found above the roof (Fig. 4), with larger TKE values in the case with heat transfer (Fig. 4.2 and 4.3). In comparison to neutral and imposed temperatures cases (Fig. 4.1 and 4.2), involving shadowing and radiation trapping effects in the radiative transfer case induces a different TKE contour in the right side part of the wake zone (Fig. 4.3).

As mentioned in Section 2.1 our model accounts the thermal stratification, thus the motion in the canyon induced by thermal effects is substantially vertical. Fig. 5 compares the distribution of the mean airflow potential temperature and velocity vector maps for the three cases. Velocity vectors are normalized by the reference velocity (i.e. 1 m s^{-1}) and projected into the center-plane. Without surface heating (neutral case, Fig. 5.1), due to the building density ($H/W=1$), the airflow pattern in the canopy is a classic skimming flow regime as described by Oke (1987): a clockwise wind flow structure develops in the center of the street canyon. Taking into account surface heating (either imposed temperatures or radiative transfer conditions), the potential temperature is increased mainly at the roof level and windward wall (Fig. 5.2 and 5.3). As a result, the airflow structure is characterized by a significant air motion along the windward faces in the cavities. As mentioned previously, the initial ground temperature outside the canyon in the imposed temperatures case is set to a constant value (35.15 °C) estimated by averaging the results of the radiative transfer computation. In fact, in the radiative transfer case, the ground temperature close to the first building is higher (+2 °C) as a result of short- and long-wave reflections and long-wave emissions between the soil and the first windward face. Behind the last building, the soil temperature in the shaded area is much lower in the radiative transfer case (12−24 °C not shown here) than in the imposed temperatures case (35.15 °C), which results in significant difference in potential temperature.

It should be pointed out that the velocity vectors (Fig. 5) show no effect of separation over the forward corner of the upwind building. These flows are always present in shear flow over bluff bodies attached to a wall. As mentioned above in the Section 2,

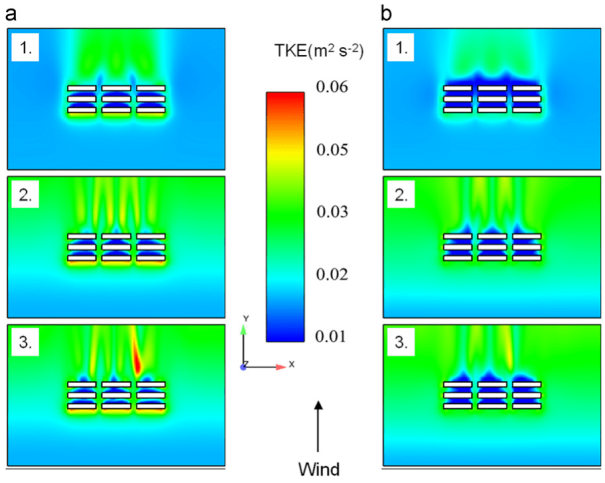

Fig. 3. Comparison of the mean turbulent kinetic energy (*TKE*) ($m^2\,s^{-2}$) distribution on (a) roof level; (b) half height of the building, for three thermal conditions: (1) neutral; (2) imposed temperatures; (3) 3D radiative transfer with a 0900 LST sun position.

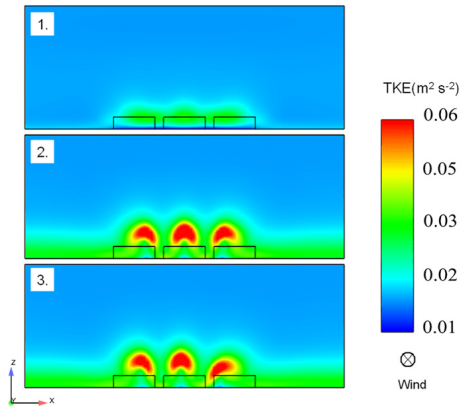

Fig. 4. Comparison of the mean turbulent kinetic energy (*TKE*) ($m^2\,s^{-2}$) distribution on the cross-section at 5*H* behind last building for three thermal conditions: (1) neutral; (2) imposed temperatures; (3) 3D radiative transfer with a 0900 LST sun position.

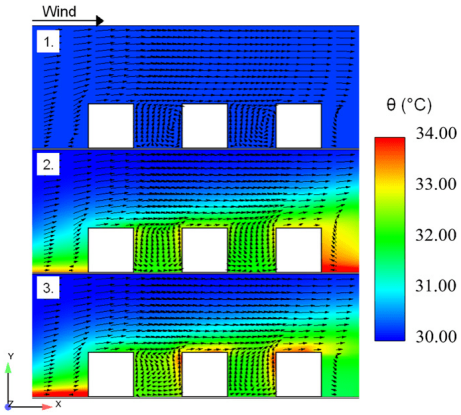

Fig. 5. Comparison of the mean airflow potential temperature (θ) (°C) distribution on the center-plane for three thermal conditions: (1) neutral; (2) imposed temperatures; (3) 3D radiative transfer with a 0900 LST sun position.

the absence of such structures on the roof is due to the fact that *k-epsilon* model tends to incorrectly predict the balance between production and dissipation of turbulence in strong velocity gradient regions such as the upwind corner of buildings. To remove this negative effect on the convective heat transfer and radiation balances over the structures is still our ongoing work, we expect this deficiency to be weak.

To further investigate the contribution of the radiative model, Fig. 6 shows the vertical velocity difference (Fig. 6.1) and the potential temperature difference (Fig. 6.2) in the center-plane between the radiative transfer case and the imposed temperatures case. We notice that taking into account the non-uniform surface heating by 3D atmospheric radiation transfer can substantially modify the distribution of the vertical velocity and potential temperature patterns in the streets, in comparison to simply setting constant surface temperatures: close to the leeward sides, the differences are between -0.3 and $0.05\ m\,s^{-1}$ for the vertical airflow pattern, and between -2 and $1.5\ ^{\circ}C$ for the potential temperature in our study case (Fig. 6).

4.2. Comparison of the different radiative transfer conditions

Up to now, we have seen that the difference between the imposed temperatures and the radiative transfer case is already complex. In fact, depending on the position of the sun and the shadows, the walls and the soil are not heated uniformly, modifying the stratification of the flow and hence the buoyancy forces and turbulence production. Furthermore, even in the same sunlit configuration (i.e. same orientation, same time of the day), the results can be different depending on the values of the parameters used to describe the material physical properties of the building walls or the ground; for instance, the albedo, which may be increased when painting the surface with a light color. In Fig. 7, using the radiative heat transfer model, we present the surface temperatures for three radiative transfer conditions: a 0900 LST sun position with a higher albedo value (0.6 instead of 0.1) for the building walls (Fig. 7.1), a reference case same as Fig. 7.1 but with an albedo of 0.1 for the building walls (Fig. 7.2), and same as 2 but for a 1600 LST sun position (Fig. 7.3). As in Section 4.1, all analyses are made after 10 min of simulation. Increasing the albedo without changing the daytime, since the building surfaces reflect more solar radiation, results in a decrease in wall temperatures (comparison of Fig. 7.1 and 7.2). In the late afternoon (1600 LST), the sun has almost shifted around to the opposite position, therefore the shaded zones appear in front of the windward side and the heated walls are mostly the leeward sides.

Fig. 8 compares the distribution of the potential temperature and the normalized velocity vector maps projected onto the center-plane under the three radiative transfer conditions listed above. In the morning, when increasing the albedo, the sunlit surfaces (windward walls and roofs) are less heated, and consequently the airflow is fairly less heated close to these areas (Fig. 8.1 and 8.2). To emphasize this further, we have plotted the differences between the case with an increased albedo of the building walls case and the reference one: in vertical velocity (Fig. 9.1) and potential temperature (Fig. 9.2). The ground close to the first windward wall and the last leeward wall is more heated because it receives more reflected solar radiation from the building walls. As a result, the potential temperature is locally increased. Increasing the albedo of the walls not only locally changes the airflow pattern (-0.05 to $0.30\ \mathrm{m\ s^{-1}}$) but also the heating pattern: warmer ground and cooler windward walls and roofs.

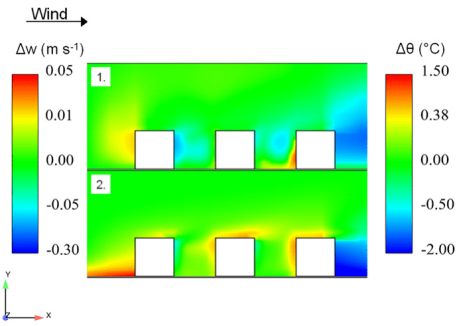

Fig. 6. Difference between 3D radiative transfer with a 0900 LST sun position and imposed temperatures case on the center-plane: (1) difference in vertical velocity (Δw) ($\mathrm{m\ s^{-1}}$); (2) difference in potential temperature ($\Delta\theta$) (°C).

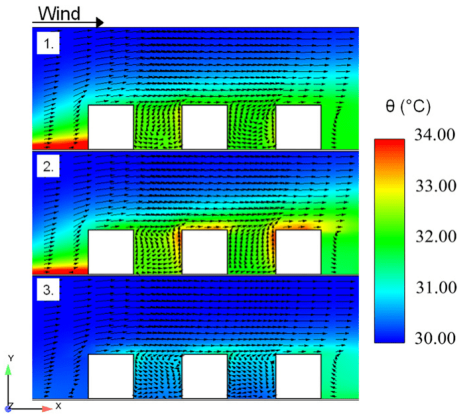

Fig. 8. Comparison of the mean airflow potential temperature (θ) (°C) on the center-plane for three radiative transfer conditions: (1) a 0900 LST sun position with an albedo of 0.6 for the building walls; (2) same as (1) but with an albedo of 0.1 for the building walls; (3) same as (2) but with a 1600 LST sun position.

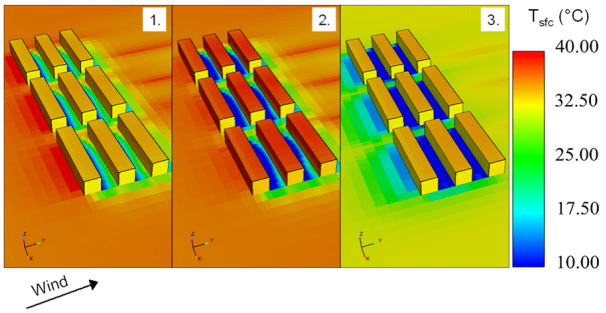

Fig. 7. Comparison of the surface temperatures (T_{sfc}) (°C) for three radiative transfer conditions: (1) a 0900 LST sun position with an albedo of 0.6 for the building walls; (2) same as (1) but with an albedo of 0.1 for the building wall; (3) same as (2) but with a 1600 LST sun position.

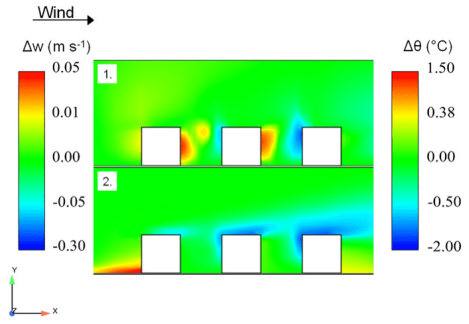

Fig. 9. Difference with a 0900 LST sun position between 3D radiative transfer with an albedo of 0.6 and with an albedo of 0.1 for the building walls on the center-plane: (1) difference in vertical velocity (Δw) (m s^{-1}); (2) difference in potential temperature ($\Delta\theta$) (°C).

In the late afternoon (1600 LST), in comparison to 0900 LST, the leeward walls are sunlit and are more heated than windward walls (Fig. 8.3). In comparison to the neutral case (Fig. 5.1), the airflow structure seems to be less disturbed than when the sun shines on the windward side and the potential temperature is not increased significantly.

4.3. Quantitative analysis

In order to clarify and quantitatively analyze the thermal impact on the airflow, we have plotted several vertical profiles of different variables at different positions in the domain. In Fig. 10a–f, we compare the vertical profiles of potential temperature, normalized vertical velocity and TKE, respectively, 0.24 m in front of the windward side and 0.28 m behind the leeward wall of the last building (from left-hand side to right-hand side) under different thermal models (i.e. neutral, imposed temperatures and different radiative transfer parameters). Taking into account the thermal stratification in the non-neutral cases, the airflow shows a large variability (Fig. 10a–f). Close to the windward wall, compared to the neutral

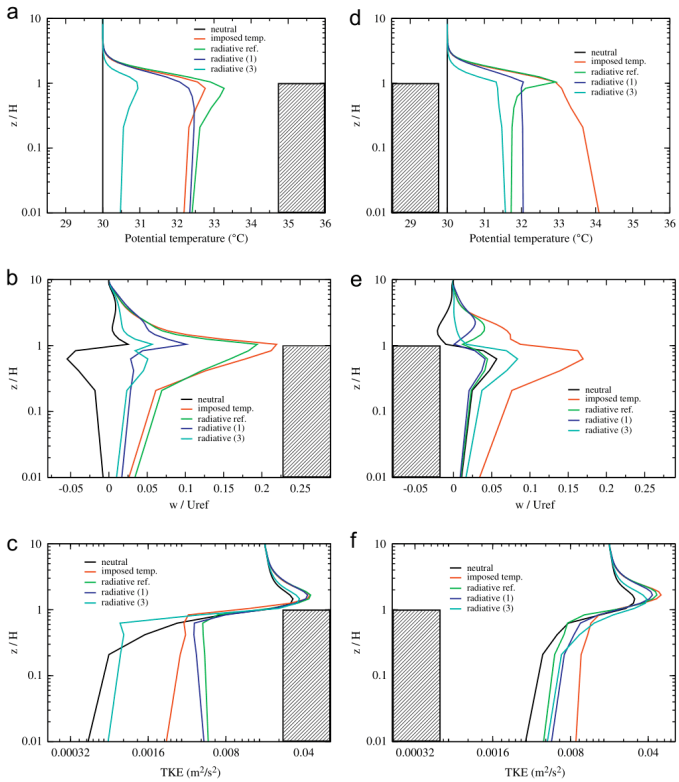

Fig. 10. Vertical profiles of (a) potential temperature (θ) (°C); (b) normalized vertical velocity (w/U_{ref}); (c) turbulent kinetic energy (TKE) (m^2 s^{-2}) 0.24 m in front of the last windward wall (from left-hand side to right-hand side) under different thermal conditions (black: neutral; red: imposed temperatures; green (i.e. radiative ref.): a 0900 LST sun position with an albedo of 0.1 for the building wall; blue (i.e. radiative (1)): same as radiative ref. but with an albedo of 0.6 for the building wall; cyan (i.e. radiative (3)): same as radiative ref. but with a 1600 LST sun position). (d)–(f) same as (a)–(c) but 0.28 m behind the last leeward wall.

condition and except in the radiative transfer case with a 1600 LST sun position, the potential temperature is largely increased near the ground level ($\sim +2.4$ °C). From $z/H=0.2$, the potential temperature rises and reaches its maximal value within the range $z/H=0.8-0.9$. After that, the airflow cools down and the profiles tend to the neutral case at about $z/H=3$. Near the last leeward wall, the potential temperature difference at the ground level between the radiative reference case (green line) and imposed temperatures case (red line) is about 2.5 °C (Fig. 10d), which is due to the shading effects behind the last buildings not taken into account in the imposed temperatures case.

When taking into account the thermal stratification, the vertical component of the velocity shows some variability (Fig. 10b and e). Without heating, the vertical velocity turns negative forming a downdraft flow in the canyons close to the windward sides or over the canyons close to the leeward sides. On the contrary, with thermal transfer, the vertical velocity is always positive and a strong updraft flow is formed from $z/H=0.2$ up to the roof level. The impact of the heating on the TKE (Fig. 10c and f) is also important at these low wind speeds. The thermal gradients near the windward wall and near the leeward wall induce a difference in the TKE production.

Close to the windward wall, choosing the imposed surface temperature on the order of magnitude of the ones from the radiative transfer case makes this case agree well with the radiative transfer case on the airflow properties (red and green lines). Significant differences are found close to the leeward side due to different treatments of the ground temperature at this area. These differences lead us to conclude on the importance of the non-uniform surface heating configuration with the 3D radiative model, linked to the full flow simulation.

For the radiative transfer cases, a late afternoon sunlit position (1600 LST) and using a higher albedo value for the walls both result in smaller heating. However, in comparison to the morning (0900 LST) with an albedo of 0.6, the late afternoon sun position with an albedo of 0.1 shows a weaker impact on the airflow (blue and cyan lines in Fig. 10a–c). Compared to the neutral case, the increase of the potential temperature is less than 1 °C in the cavity (black and blue lines in the Fig. 10a). Moreover, the variability of the vertical velocity and the TKE are also moderate along the windward wall (black and blue lines in the Fig. 10b and c). Behind the last building, the heating of the leeward wall has less influence on the airflow pattern than the heating of the windward one.

5. Conclusions and perspectives

We have investigated the effects of different wall heating conditions on the airflow within an idealized canopy in a low wind speed case, using new atmospheric radiative and thermal schemes implemented in the 3D CFD code (*Code_Saturne*). Firstly, the results show the importance of the thermal stratification effects in urban areas for low wind speed and especially the contribution of 3D radiative transfer within the canopy. The thermally induced motion is combined with the mechanically induced motion formed in the canyon, mainly resulting in increased upward motion. In this short-term study (10 min with a reference velocity of 1 m s^{-1}), the radiation heat transfer plays a major role in the surface energy balance (SEB). For instance, the net radiation flux (Q^*) on the windward wall of the center building is in the range of $240-480$ W m^{-2} versus convection which is only about $20-50$ W m^{-2}. Because of the shading effects, the multi-reflections and the infrared emissions, 3D atmospheric radiative transfer induces a non-uniform and asymmetrical wall heating which, in comparison to the uniform and symmetrical wall heating from imposed surface temperatures conditions, modifies the airflow pattern. The maximum difference close to the leeward walls reaches 0.3 m s^{-1} for the vertical velocity and 2 °C for the potential temperature.

Secondly, under radiative transfer conditions, we also discussed the influence of the sun position and different values for the albedo of the building. The results show that changing the physical parameters of the walls have an important effect on the potential temperature and motion. We illustrate that increasing the albedo from 0.1 to 0.6 (e.g. painting a dark surface to white) reduces the net radiation flux term in the SEB, as a result, the potential temperature close to the windward wall or roof may decrease by 2 °C. More examples, using different building materials (e.g. wood, brick) may modify the Q^* term (difference in the infrared emission) and the conductive heat flux (Q_{cond}) term (difference in the conductivity or thickness, etc.), therefore has a potentially important influence on the airflow pattern. By describing simulations with the same building physical parameters but different sun positions, we show that solar heating of the leeward wall (at 1600 LST) has less influence on the airflow pattern than the heating of the windward wall (at 0900 LST) for our particular set-up.

This knowledge is important to further assess the street canyon ventilation potential, the possible shading strategies on building surfaces and the influence of both aspects on indoor thermal comfort and air quality. It can also contribute to future research and applications in the field of wind engineering and pollutant dispersion in the urban environment, when the thermal stratification is of importance.

However, this discussion is based on an idealized urban area. In a real urban environment, the complex geometry has a strong influence on the wind field. It is well known that conventional *k-epsilon* models, with the turbulent viscosity formulation, tend to overestimate the level of turbulent kinetic energy around the stagnation point and incorrectly model flow over bluff bodies with respect to separation and reattachment. One direction of future work is to use the Large Eddy Simulation (LES) approach to increase the accuracy of the prediction of the airflow around buildings.

Moreover, the simulation results were not compared to any experiment. Using a real measurement dataset may be appropriate to qualitatively evaluate the numerical simulations and enrich the discussion. In order to focus on topics related to microscale dispersion in irregular canopy and complex urban environments, our ongoing work is evaluating this model on a district of a real urban area with the CAPITOUL field experiment (City of Toulouse, France).

References

Archambeau, F., Méchitoua, N., Sakiz, M., 2003. *Code_Saturne*: a finite volume code for the computation of turbulent incompressible flows—industrial applications. International Journal on Finite Volumes 1, 1–62 (available online at 〈http://www.latp.univ-mrs.fr/IJFVDB/saturne.pdf〉).

Blocken, B., Stathopoulos, T., Carmeliet, J., 2007. CFD simulation of the atmospheric boundary layer: wall function problems. Atmospheric Environment 41 (2), 238–252.

Fiveland, W.A., 1984. Discrete-ordinates solutions of the radiative transport equation for rectangular enclosure. Journal of Heat Transfer 106 (4), 699–706.

Franke, J., Hellsten, A., Schlünzen, H., Carissimo, B., 2007. Best Practice Guideline for the CFD Simulation of Flows in the Urban Environment: COST Action 732: Quality Assurance and Improvement of Microscale Meteorological Models. Technical Report. ISBN 3-00-018312-4. COST Office Brussels.

Kanda, M., 2006. Progress in the scale modeling of urban climate: review. Theoretical and Applied Climatology 84, 23–33.

Kim, J., Baik, J., 2001. Urban street-canyon flows with bottom heating. Atmospheric Environment 35 (20), 3395–3404.

Kovar-Panskus, A., Moulinneuf, L., Savory, E., Abdelqari, A., Sini, J.F., Rosant, J.M., Robins, A., Toy, N., 2002. A wind tunnel investigation of the influence of solar-induced wall-heating on the flow regime within a simulated urban street canyon. Water, Air, & Soil Pollution 2 (5–6), 555–571.

Liu, J., Shang, H.M., Chen, Y.S., 2000. Development of an unstructured radiation model applicable for two-dimensional planar, axisymmetric, and three-dimensional

geometries. Journal of Quantitative Spectroscopy & Radiative Transfer 66 (1), 17–33.
Louis, J.F., 1979. A parametric model of vertical eddy fluxes in the atmosphere. Boundary-Layer Meteorology 17 (2), 187–202.
Louka, P., Vachon, G., Sini, J.F., Mestayer, P.G., Rosant, J.M., 2001. Thermal effects on the airflow in a street canyon—nantes 99 experimental results and model simulation. Water, Air, & Soil Pollution 2 (5–6), 351–364.
Miguet, F., Groleau, D., 2002. A daylight simulation tool for urban and architectural spaces—application to transmitted direct and diffuse light through glazing. Building and Environment 37 (8), 833–843.
Milliez, M., 2006. Modélisation micro-météorologique en milieu urbain: dispersion des polluants et prise en compte des effets radiatifs. Ph.D. Thesis. École des Ponts ParisTech (in French, available on line at 〈http://cerea.enpc.fr/fr/theses.html〉).
Milliez, M., Carissimo, B., 2007. Numerical simulations of pollutant dispersion in an idealized urban area, for different meteorological conditions. Boundary-Layer Meteorology 122 (2), 321–342.
Milliez, M., Carissimo, B., 2008. CFD modelling of concentration fluctuations in an idealized urban area, for different meteorological conditions. Boundary-Layer Meteorology 127 (2), 241–259.
Musson-Genon, L., Dupont, E., Wendum, D., 2007. Reconstruction of the surface layer vertical structure from measurements of wind, temperature and humidity at two levels. Boundary-Layer Meteorology 124 (2), 235–250.
Niachou, K., Livada, I., Santamouris, M., 2008. Experimental study of temperature and airflow distribution inside an urban canyon during hot summer weather conditions. Part II. Airflow analysis. Building and Environment 43 (8), 1393–1403.
Oke, T.R., 1987. Boundary Layer Climates, 2nd ed. Routledge.
Onomura, S., Takimoto, H., Kanda, M., 2009. Influence of a heated wall on urban canopy flow using PIV measurements. In: Seventh International Conference on Urban Climate. Yokohama, Japan. June 29–July 3.
Qu, Y., 2011. Three-Dimensional Modeling of Radiative and Convective Exchanges in the Urban Atmosphere. Ph.D. Thesis. École des Ponts ParisTech/University of Paris-Est (available on line at 〈http://cerea.enpc.fr/fich/yongfengthesisfinal.pdf〉).
Qu, Y., Milliez, M., Musson-Genon, L., Carissimo, B., 2011. Micrometeorological modeling of radiative and convective effects with a building resolving code. Journal of Applied Meteorology and Climatology 50 (8), 1713–1724.
Richards, K., Schatzmann, M., Leitl, B., 2006. Wind tunnel experiments modelling the thermal effects within the vicinity of a single block building with leeward wall heating. Journal of Wind Engineering and Industrial Aerodynamics 94 (8), 621–636.
Richards, P.J., Hoxey, R.P., 1993. Appropriate boundary conditions for computational wind engineering models using the $k-\varepsilon$ turbulence model. Journal of Wind Engineering and Industrial Aerodynamics 1993 (46–47), 145–153.
Santiago, J.L., Dejoan, A., Martilli, A., Martin, F., Pinelli, A., 2010. Comparison between large-eddy simulation and Reynolds-averaged Navier–Stokes computations for the must field experiment. Part I. Study of the flow for an incident wind directed perpendicularly to the front array of containers. Boundary-Layer Meteorology 135 (1), 109–132.
Sini, J.F., Anquetin, S., Mestayer, P., 1996. Pollutant dispersion and thermal effects in urban street canyons. Atmospheric Environment 30 (15), 2659–2677.
Truelove, J.S., 1987. Discrete-ordinates solutions of the radiative transport equation. Journal of Heat Transfer 109 (4), 1048–1051.
Uehara, K., Murakami, S., Oikawa, S., Wakamatsu, S., 2000. Wind tunnel experiments on how thermal stratification affects flow in and above urban street canyons. Atmospheric Environment 34 (10), 1553–1562.
Xie, X., Liu, C.H., Leung, D.Y.C., 2007. Impact of building facades and ground heating on wind flow and pollutant transport in street canyons. Atmospheric Environment 41 (39), 9030–9049.
Yee, E., Biltoft, C.A., 2004. Concentration fluctuations measurements in a plume dispersing through a regular array of obstacles. Boundary-Layer Meteorology 111 (3), 363–415.

2.2.4. Validation du modèle sur un quartier réel

Dans les deux publications précédentes, la zone urbaine était idéalisée. Ainsi, dans une troisième étape, nous avons simulé un quartier réel et validé le modèle proposé avec les données expérimentales issues d'une campagne de mesures réalisée à Toulouse (**Masson et al., 2008**).

Les résultats sont consignés dans l'article qui suit **(Qu et al. 2020).**

Référence:

Qu, Y., M. Milliez, L. Musson-Genon and B. Carissimo, 2020: Three-dimensional modelling of radiative and convective exchanges over a European city centre, paper submitted to J. Atmosphere

atmosphere

MDPI

Type of the Paper (Article)

Three-dimensional modelling of radiative and convective exchanges over a European city centre

Yongfeng QU [1], Maya MILLIEZ [1] , Luc MUSSON-GENON [1] and Bertrand CARISSIMO [1,*]

[1] CEREA Teaching and Research Centre in Atmospheric Environment, (Ecole des Ponts ParisTech / EDF R&D)

* Correspondence: Bertrand.Carissimo@enpc.fr

Received: date; Accepted: date; Published: date

Abstract: Many micro-meteorological studies on flow and pollution dispersion assume a neutral atmosphere and most building energy balance models neglect the three-dimensional local variation of the flow and temperature fields. The aim of this work is to develop a three-dimensional (3D) tool coupling thermal energy balance of the buildings and modelling of the atmospheric flow in urban areas. To do so, we have developed a 3D microscale atmospheric radiative scheme in the atmospheric module of the 3D Computational Fluid Dynamics (CFD) code *Code_Saturne* adapted to complex geometry. The full coupling of the radiative transfer and fluid dynamics models has been validated with idealised cases. In this paper, our focus is to simulate the diurnal evolution of the brightness surface temperatures of a district of the city centre of Toulouse, in the South-West part of France, taking into account the 3D effects of the flow around the buildings, in real meteorological conditions. The mesh developed for the city centre and the simulation conditions for the selected day of the campaign are presented. The results are evaluated with the measurements from the Canopy and Aerosol Particles Interactions in TOulouse Urban Layer experiment (CAPITOUL).

1. Introduction

The influence of the urban thermal environment has received more attention than in the past. City residents are subjected to modified thermal environments as well as increased air pollution. In addition, a thermally comfortable environment is important for the inhabitants and commuters of urban areas. Current research concludes that emissions in buildings are one of the major sources of the pollution that causes urban air quality problems and green house gases that contribute to climate change. In that event, sustainable development requires the improvement of the interrelationship between buildings, their components, their surroundings and their occupants. In order to improve the urban microclimate, various countermeasures have been proposed and researched, such as roof greening, use of high albedo paints, and water-retentive materials, etc.

Then in order to better understand the phenomena occurring at neighbourhood scale and to study different scenarios, more and more realistic simulation tools are also developed, such as Computational Fluid Dynamics (CFD) analysis. The behavior of the atmospheric Urban Canopy Layer (UCL) is the result of the interactions between atmospheric structures induced by the urban heterogeneities. One important feature of the UCL is the urban Surface Energy Balance (SEB). Recent researches have sought to reconsider the problem of modeling the SEB , particularly to improve the modeling of the thermo-radiative and aerodynamic phenomena. For instance, in order to learn more about the impacts of

atmosphere MDPI

different proportion of green area, Jesionek and Bruse (2003) developed a classification scheme for typical European urban building types and have simulated them systematically with the microscale climate model ENVI-met. The simulation results where analyzed primarily in view of thermal advantages and disadvantages of increased green area and its effects on pollution dispersion and accumulation. It is shown, that especially in densely build up block structures, greening with trees leads to higher pollution concentration, while in more open structures the thermal advantages of greening, due to shadow effects, can be fully used to improve of the microclimate. Chen et al. (2009) performed coupled simulations of convection, radiation and conduction to evaluate the outdoor thermal environment over different urban blocks, a high-rise area and a mid-rise area in the city of Tokyo in Japan, to compare the effects of measures such as the position of the heat release point of air-conditioning, greening, high surface albedo, and traffic volume. The results showed that the effectiveness of moderation countermeasures differed according to the configuration of the urban blocks. Bouyer, Inard, and Musy (2011) presented the SOLENE-microclimate model including a soil model and a inner building thermal model, this last one allowing to compute the energy consumption of a building interacting with its urban environment. They are both integrated into the SOLENE (thermo-radiative simulation tool), then using the commercial CFD tool as a quasi-dynamic coupling to calculate the air temperature, mass concentrations of moisture and heat transfer coefficient. However, only the energy transport and moisture equations in the CFD tool are solved. Except for the initialization phase, the absence of resolution of momentum equations does not allow to take into account the movement of natural and mixed convection of the airflow in the canopy.

The present research aims to accurately simulate the atmosphere and surfaces in urban environments at microscale. Existing canopy models often use a statistical representation of building which is generally obtained through quantitative field survey or qualitative estimates. But in performing this geometric simplification there is no way to ensure that the simplified geometry match locally the actually city. In this work we want to represent the energy and momentum exchanges in portion of an existing city as realistically as possible. Thus, the objective is to fully model the three-dimensional (3D) airflow in the urban canopy in non neutral conditions and therefore to take into account atmospheric radiation and heat transfers for complex geometries. A new 3D microscale radiative scheme has been previously implemented in the open-source CFD code Code_Saturne, described in details by (Milliez 2006; Qu 2011). As a full thermo-radiative-convective coupling, the model was evaluated with idealized cases, using as a first step, a constant 3D wind field (Milliez 2006). Then, Qu et al. (2011) have validated the full thermo-radiative-convective coupling by comparison with several surface wall temperatures from Mock Urban Setting Test (MUST) field campaign (Yee and Biltoft 2004; Milliez and Carissimo 2007, 2008). Furthermore, in order to assess the thermal impact on the flow fields in different thermal conditions, Qu et al. (2012) extend the work of Qu et al. (2011) to lower wind speed and a higher building density than in MUST.

In order to validate our model as completely as possible with a large available experimental data-set in a real urban environment, we choose the Canopy and Aerosol Particles

Interactions in TOulouse Urban Layer (CAPITOUL) experimental data-set (Masson et al. 2008). Hereafter, we first give a brief overview of the experimental campaign. Then we present the mesh developed for the city centre and the simulation conditions for the selected day of the campaign. Afterwards, we discuss the simulation results with the observation including surface brightness temperatures, infrared pictures taken by an airborne infrared thermo-graph, sensible heat flux, radiation flux, friction velocity data.

2. Model Description

The simulations are performed with the 3D open-source CFD code *Code_Saturne* which can handle complex geometry and complex physics. The numerical solver employs a finite-volume approach for co-located variables on an unstructured mesh. Time discretization is achieved through a fractional step scheme, with a prediction-correction step (Archambeau, Méchitoua, and Sakiz 2003).

Adapted for multi-scales atmospheric airflow (either neutral or stratified) and pollutant dispersion studies, the atmospheric module of *Code_Saturne*, described in Milliez and Carissimo (2007) uses a detailed representation of the surfaces allowing a complex 3D spatial representation of wind speed, turbulence, and temperature. Two turbulent approaches are available in the module, Reynolds-Averaged Navier-Stokes simulation (RANS) and Large Eddy Simulation (LES). We choose the RANS approach with a $k-\varepsilon$ turbulence closure for our simulations. We stress that despite the fact that the $k-\varepsilon$ closure is generally unable to capture precisely the geometry dependent large eddies in many complex flows and overestimates the dissipated energy, it gives a fairly acceptable accuracy with a reasonable computational time for this research work.

In this study, we neglect the anthropogenic heat flux and the latent heat flux. The advection fluxes are obtained by the resolution of the entire flow field. Thus, for each surface the SEB is expressed as:

$$Q_{cond} + Q_H = Q^*,$$

where Q_{cond} is the conductive heat flux ($W\ m^{-2}$) within the building or the ground subsurface, which links the surface temperature to the internal building or the deep soil temperature, Q_H is the sensible heat flux ($W\ m^{-2}$) which depends on the local airflow intensity, Q^* is the net radiative flux ($W\ m^{-2}$).

3. Thermo-radiative model

The radiative fluxes are computed using the Discrete Ordinate Method (DOM) (Fiveland 1984) which solves the radiative transfer equation for a gray non-diffusive semi-transparent media by the directional propagation of the radiative wave. In our models, the angular discretization has two resolutions: 32 or 128 directions and the spatial discretization use the same mesh as the CFD model. Taking into account both short- and long-wave radiation separately, we have adapted a radiative heat transfer scheme available

atmosphere MDPI

for combustion in *Code_Saturne*. Described in detail by Milliez (2006), the new atmospheric 3D radiative approach was developed in *Code_Saturne* for built-up areas. The main advantage of this model is that the radiative transfer equations is solved in the whole fluid domain and not only at solid faces (such as when using view factors), but also can be applied to non-transparent media (e.g. fog or pollution). In this work, we consider a transparent atmosphere between the buildings at the microscale of our simulations.

4. Surface temperature model

As a key parameter, surface temperature T_{sfc} (K) is determined by the SEB and is related in a fundamental way to each of its component fluxes. In the previous work (Qu et al. 2011), the surface temperature was obtained by either with force-restore approach or wall thermal model. In order to take advantage of the each model, in this work, we model the ground temperature with force-restore method and the building surfaces (wall/roof) temperature with wall thermal model. Hence, the modeled surface temperature is separately treated by the relationship:

Ground temperature: Force-restore method

This simple approach is widely used for soil models in meteorological models (Deardorf 1978).

$$\frac{\partial T_{sfc}}{\partial t} = \frac{\sqrt{2\omega}}{\mu_t}(L^* + S^* - Q_H) - \omega(T_{sfc} - T_{g/b})$$

where ω (Hz) is the Earth angular frequency, L^* $(W\ m^{-2})$, S^* $(W\ m^{-2})$, Q_H $(W\ m^{-2})$ are respectively net long-wave, net short-wave, and sensible heat flux, μ_t $(J\ m^{-2}\ s^{-0.5}\ K^{-1})$ the thermal admittance and $T_{g/b}$ (K) either deep soil or internal building temperature.

Building surface temperature: Wall Thermal Model

In the hypothesis of a single layer to express the conduction term, the is:

$$\frac{\lambda}{e}(T_{sfc} - T_{int}) + h_f(T_{sfc} - T_a) = \varepsilon(L_a + L_e - \sigma T_{sfc}^4) + (1-\alpha)(S_D + S_f + S_e)$$

where λ $(W\ K^{-1}\ m^{-1})$ is the average thermal conductivity of the wall, e (m) the thickness of the wall, T_{int} (K) the internal building temperature, h_f $(W\ m^{-2}\ K^{-1})$ the heat transfer coefficient and T_a the external air temperature (K).

In order to take into account the variation of the internal building temperature, it is computed with an incremental-adjustment method modified after (Masson, Grimmond, and Oke 2002) and similarly used by (Krayenhoff and Voogt 2007):

$$T_{int}^{n+1} = T_{int}^{n-1}\left(\frac{\tau - \Delta\, t}{\tau}\right) + \overline{T}\left(\frac{\Delta t}{\tau}\right),$$

where T_{int}^{n+1} (K) and T_{int}^{n-1} (K) are the computed internal temperatures at the following and previous time step respectively, Δt is the time step (s), τ (s) refers to the number of seconds in a day, and $\overline{T}$ (K) is the average outside building surface temperatures computed at time step n and is set one by one. For a diurnal simulation, the initialized internal temperature value can be considered as same as the initialized outside surface temperature (e.g. T_{sfc} at midnight) or the outside surface temperature at half hour ago if the observation data is available.

Brightness temperature

In this work, we compare the simulated and measured brightness surface temperature obtained from infrared imagery. A brightness surface temperature (T_{br} (K)) is defined here as the temperature that yields an emitted broadband thermal radiance equivalent to the sum of the true broadband emitted radiance (with reduction due to gray body emissivity) and the broadband reflected radiance (after infinite reflections for canyon surfaces)(Krayenhoff and Voogt 2007; Hénon 2008):

$$T_{br} = \sqrt[4]{\varepsilon T_{sfc}^4 + \frac{(1-\varepsilon)L^{\downarrow}}{\sigma}}.$$

where ε is the long-wave emissivity, σ the Stefan-Boltzmann constant and $L^{\downarrow}$ $(W\ m^{-2})$ incident long-wave radiation.

5. Convection model

The surface convective heat flux must be computed to both solve the surface energy balance and determine the surface-air thermal gradient and therefore turbulent transport. In *Code_Saturne*, the convective heat transfer is computed in 3D for each surface patch. The buildings are explicitly defined in our simulations. Therefore, the detailed representation of the surface allows for a more complex 3D spatial representation of wind speed, turbulence, and temperature than simple canopy averages or vertical profiles. We use a rough wall boundary condition, based on the logarithmic law modified by the stratification. Usually these modified laws are based on the Monin-Obukov similarity but are implicit and therefore need to be solved iteratively. Here we use an explicit approach based on the work of Louis (1979) and described in Musson-Genon, Dupont, and Wendum (2007).

The heat transfer coefficient h_f is computed for each solid sub-facet, depending on the local friction velocity u_* $(m\ s^{-1})$:

$$h_f = \frac{\rho C_p u_* \kappa f_h}{\sigma_t ln(\frac{d+z_0}{z_{0_T}})\sqrt{f_m}},$$

where C_p is specific heat $(J\ kg^{-1}\ K^{-1})$, u_* is the friction velocity, κ is von Kármán constant, σ_t the turbulent Prandtl number, d (m) is the distance of the cell center to the wall, z_0 the

atmosphere MDPI

roughness length (m), z_{0_T} the thermal roughness length (m), f_m and f_h are the (Louis 1979) stability functions which take a value of 1 for neutral conditions. For vertical walls, the neutral conditions are applied.

6. Overview of CAPITOUL field experiment

The CAPITOUL campaign is a joint experiment, organized by the Centre National de Recherches Meteorologiques and other partners (Laboratoire d'Aérologie, Laboratoire des Mécanismes et Transferts en Géologie and ORAMIP local air quality agency), which took place in Toulouse in southwest of France (4336'16.21"N, 126'38.5"E) from February 2004 to February 2005. It is an effort in urban climate, aiming to document the energetic exchanges between the surface and the atmosphere, the dynamics of the boundary layer over the city, and the interactions between urban boundary layer and aerosol chemistry. A general view of the experiment, describing the goals, experimental set up and a summary of the results is given by (Masson et al. 2008).

Objectives and description of the site

The old downtown area with an area of approximately 3.5 km^2 is generally made up of buildings 4 to 5 stories high with the walls primarily composed of brick and stone and the roofs of clay tile (Figure 1). The surrounding landscape is relatively flat with small rolling hills. Study of the energetic exchanges between the surface and the atmosphere was one of the objectives (Moscicki 2007; Pigeon et al. 2008). We briefly describe the data used in this study.

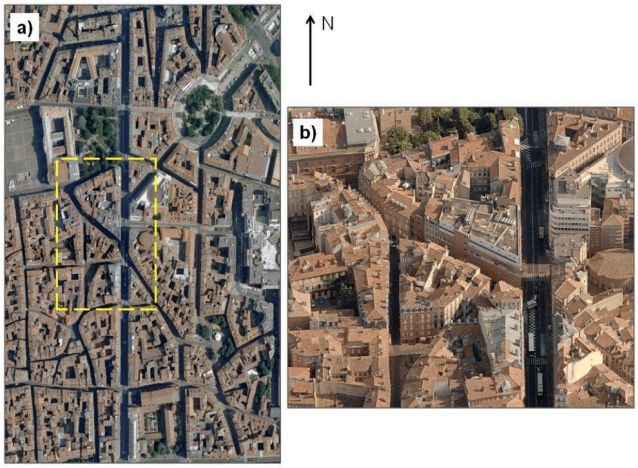

Figure 1 : Aerial view of downtown Toulouse, France: a) main study area, from Google Maps; b) zoom in the selected area (in a yellow contour), from Bing Maps. The north is indicated

Meteorological data

The study area is mainly located in the central site of Toulouse around the corner of the two streets, Alsace-Lorraine and Pomme (yellow contour in Figure 1a and b). In this neighborhood, vegetation is very scarce and buildings are around 20 m in height (Pigeon et al. 2008). The base of the meteorological mast was on a roof at a height of 20 m, with the top of the mast being 47.5 m above the road (position shown by a star in Figure 2). It provided data including short- and long-wave radiation flux, sensible heat, latent heat, air temperature, wind speed and direction etc. continuously from mid-February 2004 to early March 2005. All meteorological variables were sampled at one-second intervals and were recorded as one minute averages (Masson et al. 2008).

atmosphere MDPI

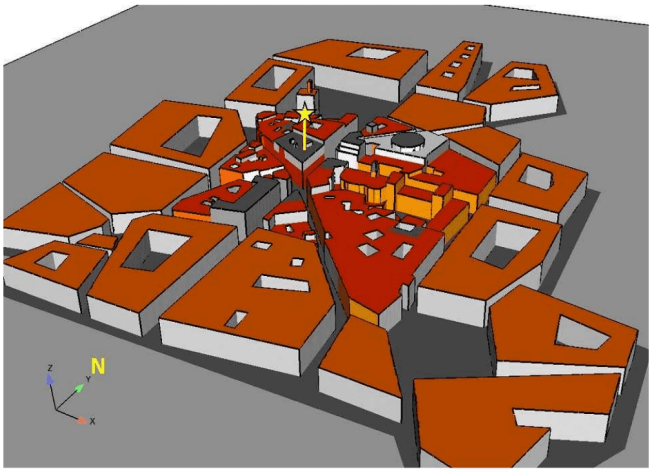

Figure 2 : Central site area geometry processed by ICEM CFD with the meteorological mast position (yellow star).

Infrared surface temperature measurements and Aircraft data

A total of ten InfraRed Thermometers (IRTs) were affixed to balconies or booms to record the surface temperatures of the roads, walls, and roofs of the canyons. Described in details in (Moscicki 2007), four IRTs were positioned in the Alsace canyon to record surface temperatures of the two walls, the road, and a roof. Three IRTs were located in both the Pomme and Remusat canyons to observe the temperature of the two walls and the road in each canyon.

InfraRed Thermal (IRT) airborne images were also obtained during several Intensive Observation Periods (IOP) with 2 airborne cameras on board of a Piper Aztec PA23 aircraft over the study area (flight 430: 0749 - 0816 UT; flight 431: 1115 - 1150 UT; flight 432: 1348 - 1423 UT). The speed of the aircraft was 70 $m\ s^{-1}$ and the camera acquisition frequency was 4.3 frames per second. The flight height was about 460 m, which results in a resolution between 1.5 and 3 m depending on the sight angle (Lagouarde et al. 2010; Hénon et al. 2012).

7. Simulation set-up

Concerning urban canopy energetics issue, several papers on the CAPITOUL project have been published. Pigeon et al. (2007) ((2007, 2008)) present the modeling of the anthropogenic heat flux by the TEB urban scheme (Masson 2000) and its validation against

anthropogenic fluxes estimated by a new method using standard surface energy balance measurements. Based on the use of SOLENE model coupled with a 3D model of the city providing the information about the actual structure of the urban canopy, Lagouarde et al. (2010) ((2010)) simulate the IRT anisotropy and the directional surface temperatures over the Toulouse city. Gastellu-Etchegorry (2008) ((2008)) imports the Toulouse urban databased as a DART scene (Gastellu-Etchegorry, Martin, and Gascon 2004) and test the DART-TEB model for simulating remote sensing images and the radiation budget of urban canopies. Recently, using SOLENE software, Hénon et al. (2012) ((2012)) assessed the case of a small district of the city center for four independent sets of measurements for two complete diurnal cycles, in summer and in winter by comparison with the thermo-radiative simulations.

Whereas earlier works estimate the sensible heat flux with simplified convection models, the heat transfer coefficient h_f is usually considered as a constant or a simple function of height. In order to model the microscale heat transfer with more accuracy by determining the surface-air thermal gradient that controls convective heat transfer and also examine the mechanisms (e.g. complex topographic influences on air motions), we perform the CAPITOUL simulation with *Code_Saturne* to investigate the thermo-dynamical impacts on the local atmosphere.

Choice of the computational domain and Mesh strategy

From the CAPITOUL experiment, we selected the day of July 15^{th} 2004. Considering Alsace-Lorraine and Pomme roads as the center of interest in the computational domain (Figure 1), the dimension of the 3D simulation domain is $891 \times 963 \times 200\ m$. The information about the 3D structure of the urban canopy was provided by the administrative authorities of Toulouse who made the 3D database of the city available for the CAPITOUL project.

First, we import the urban database (AutoCAD format) of the Toulouse town hall into the commercial mesher ICEM CFD. The urban elements in the database are not individual houses or buildings but a group of the walls and roofs including a large number of internal fine walls which are unnecessary to be meshed. Moreover, the urban elements have a variety of heights but no soil element. So before the meshing step, it is necessary to do a preparatory work on the geometry. After a series of geometric optimization (remove the internal surface, simplify a part of details, create the ground then project the buildings onto it ...), we build a proper geometry topology as shown in Figure 2. In real urban environment, all obstacles cannot be resolved with sufficient detail, but their impact need to be parametrised. We describe the strategy for this study as follows. From the boundary of the domain to the center, we progressively retain more geometric details. That is, the buildings at these Alsace-Lorraine and Pomme streets in the center study area are modeled with fine details. Then, the surrounding buildings next to the center study area are simplified as urban blocks. Finally, the buildings in the region outside are treated with a high roughness value in this work . The volumetric mesh used here is an unstructured grid of about 4,5 million tetrahedral cells. The grid resolution varies from 0.5 m near the center to 10 m far from the centre zone (Figure 3).

atmosphere MDPI

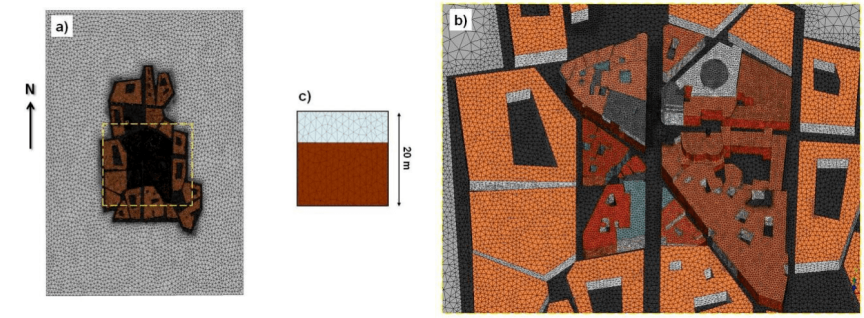

Figure 3: Tetrahedral mesh on the central area: a) whole area; b) zoom in the selected area a) (yellow contour); c) zoom in a Monoprix building wall. The north is indicated by N

The wind inlet boundary conditions are determined from measurements, using the meteorological mast which gives the wind velocity every 2 hours (Figure4a), wind direction (4b), and potential temperature profiles (4c).

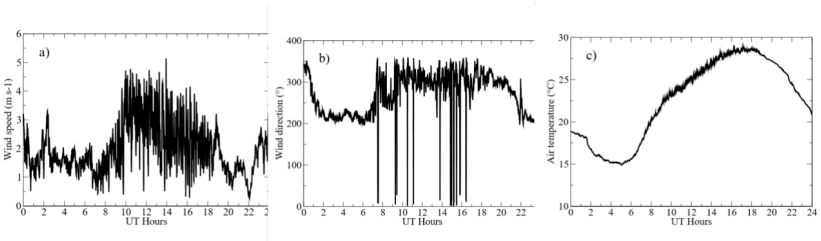

Figure 4: Meteorological data at 47.5 m above the road from the CAPITOUL experiment for 15 July 2004: a) Wind speed (m s–1), b) Meteorological wind direction (°), and c) Air temperature (°C).

From some Toulouse city pictures, we estimate the roughness value depending on its location and set values for the roughness length. Based on Pigeon et al. (2008), we set the thermal properties such as surface conductivity and thickness. We summarize the model parameters in Table I. Since the values from Pigeon et al. (2008) are averages over the 500-m radius around the surface energy balance station, inspecting some Toulouse pictures from Google Maps, we furthermore classify into four wall painting color (rose, gray, whitewash and white) for the buildings in the center area to estimate the albedo. Their values are given in Table II.

8. Results and discussion

Comparison of IRT pictures

An IRT picture from for the aircraft flight 432 of July 15, 2004 at 1412 UT is shown in Figure 5a. In Figure 5b and 5c, we depict respectively the modeled brightness temperature and surface temperature with the radiative-convective full coupling. We note that it is difficult to compare value by value because of the simplification of the geometry. However, since we distinguish different albedo from painting colors, the model reproduced well the heterogeneity of the distribution of the brightness temperature, especially at roof level (Fig. 5b). We can also note that if we were to keep more details especially some slopes on central roof in our 3D model to create a more detailed distribution of the shadows on the roof, the simulated brightness roof temperature would be closer to the observations. The value of the modeled surface temperatures (Fig. 5c) is obviously larger than the modeled brightness one (e.g. about 3°C difference on the roof), because we can see that the brightness temperature is approximately proportional to the product of the surface temperature and emissivity ($T_{br} \approx T_{sfc}\varepsilon^{1/4}$, the emissivity being smaller than 1).

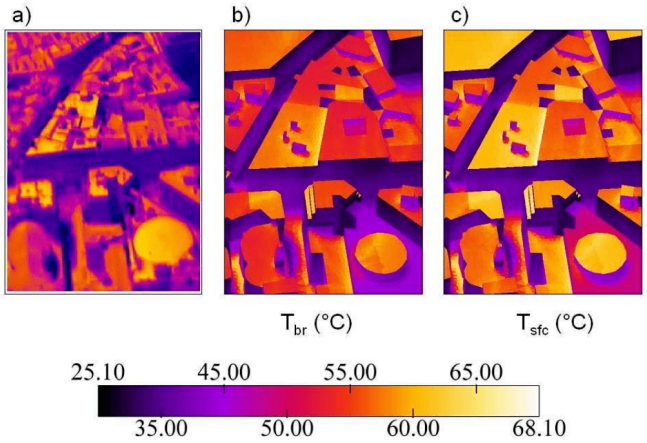

Figure 5: Comparison between the Infrared Thermal (IRT) airborne images, simulated brightness temperatures and surface temperatures of July 15, 2004, at 1412 UT during flight 432 (Lagouarde et al., 2010): a) TIR picture (189 ×118 pixels), source from (Hénon, 2008); b)

atmosphere MDPI

modeled brightness temperature with full radiative-dynamic coupling; c) same as b) but for modeled surface temperature.

Figure 6 from (a) to (d) shows the measured and modeled brightness temperatures for the aircraft flight 431 at 1138 UT, compared with three modeling approaches: radiative model only (Fig.6b), radiative and a constant heat transfer coefficient (Fig.6c), and radiative-convective full coupling (Fig.6d) using the hybrid thermal scheme for the streets and walls. The constant heat transfer coefficient (Fig.6c) is set similar to Hénon (2008) and Hénon et al. (2012). The result of the first simulation (Fig.6b, radiative scheme alone) shows that the brightness temperatures are obviously higher than measurements. For a graphical reason, an additional black contour is drawn to show the building structures. Especially on the roof, the difference is more than 25°C. The modeled T_{br} is out of color range.

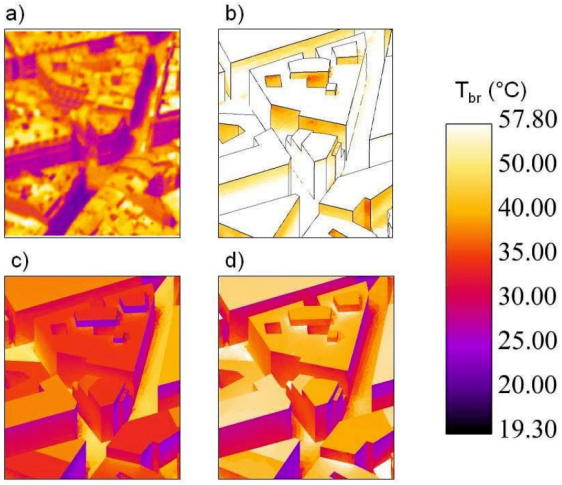

Figure 6: Comparison between the simulated brightness temperatures and Infrared Thermal (IRT) airborne images of July 15, 2004, at 1138 UT during flight 431 (Lagouarde et al., 2010): a) TIR picture (189×118 pixels), source from (Hénon, 2008); b) Modeled brightness temperature without taking into account the convection; c) Same as b) but with a constant heat transfer coefficient; d) Same as b) but with full radiative-dynamic coupling.

Either taking a constant heat transfer coefficient, i.e. assuming a constant wind field in the domain or taking a variable heat transfer coefficient with full coupling i.e. more realistically modeling the wind field, as expected, the results (Fig.6c and d) show a much better agreement with observation (Fig.6a) in comparison to radiative model only case (Fig.6b). From this IRT picture with this view (Fig.6a), in spite of the fact that we did not keep all the

elementary details on the roofs with different orientations and slopes, the simulated temperatures represent well the spatial variability of the observed temperatures.

For the variable h_f case, the model-observation difference rarely exceeds 10°C (Fig.6d). We notice also in the measurement (Fig.6a) that for the same roof and same orientation, the temperature may differ by more than 5°C, for instance at the bottom right of the image. This may be due to heterogeneities in materials and geometry which cannot be all accounted for by modeling each individual area (or even every detail). For building walls, either shaded or sunlit, the difference between measurement and simulation is generally less than 5°C. In the measurements, some horizontal faces (e.g. buildings at center left) are relatively warmer than others. This may be due to some external structures (e.g. balcony) that are not modeled but were exposed to the sun and therefore received more solar heating (Hénon 2008). Regarding the streets, a minimum of 3 cells were set for the width; the model is able to simulate the sharpness of the shadow (Fig.6c and d). The portion of the street brightness temperatures near the buildings is well reproduced. The averaged difference is less than 3°C and the simulated sunny portion is underestimated by about 5°C.

The difference between constant h_f case and variable h_f case (Fig.6 c and d) is also evident. These two different h_f are shown in Figure 7. With the chosen, the constant h_f case shows an overcooling about 15°C at roof level, 4 to 5°C at the walls, 4°C in shaded streets and 7°C in sunlit streets (Fig.6c). The difference is due to the overestimation of constant chosen value ($h_f = 12$) at this moment. In fact, the contribution of the variable h_f may be more important on the surface and air temperature when modeling the temporal evolution. For this reason, we perform the simulation with full coupling for a diurnal evolution in the next section.

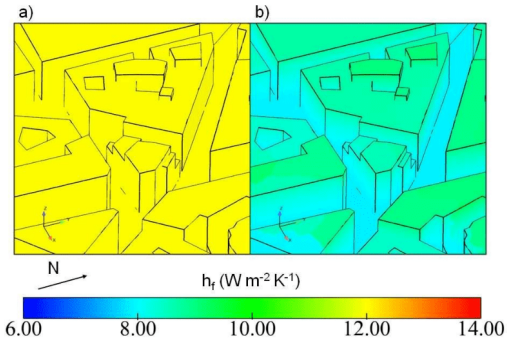

Figure 7: Comparison between two convective models with visualisation of heat transfer coefficient hf (W m−2 K−1) during same flight as Fig. 6: a) constant hf = 12 corresponding to Fig. 6c; b) variable hf corresponding to Fig. 6d.

atmosphere MDPI

Comparison of the local diurnal evolution of brightness surface temperature T_{br}

Figure 8a to c present the model-observation comparison for the brightness surface temperatures of the diurnal cycle of July 15, 2004. The simulation is performed with full radiative-dynamic coupling. Hereafter, unless specified otherwise, all the results refer to full coupling simulations. The infrared radiometers provided the measured brightness temperatures. Their fixed positions around the central building of the study district are shown in Figure 9. Overall, the diurnal evolutions of the brightness surface temperatures at the local positions in the scene are correctly simulated.

For the faces of the Alsace street (black and red lines in Fig. 8a), an overcooling about 5°C appears during the evening (1800 to 2400 UT). However, for the Alsace west face, the model predicts a higher brightness temperature (red line in Fig. 8a) from 0600 to 1200 UT. By using SOLENE model, (Hénon et al. 2012) also report a similar difference in surface temperature. They explain that this may be due to a sensor underestimation. The ground temperature is computed by the force-restore method which is well adapted for the soil model. The bias on the Alsace road (green line in Fig. 8a) can be explained by the approximation of the modeled shadow. Indeed, values taken from the selected cell might be quite different from its neighborhood values.

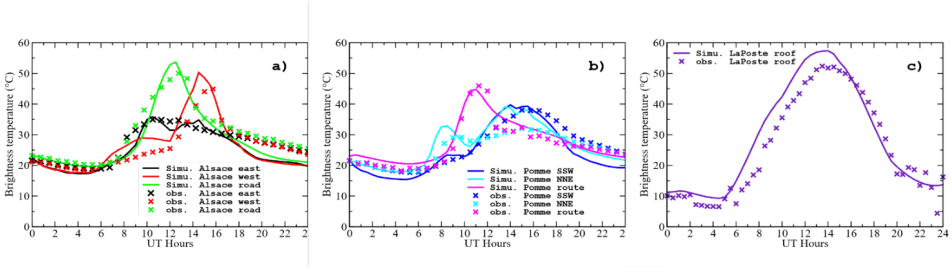

Figure 8: Evolution of brightness surface temperature of different positions of the infrared thermometers during a diurnal cycle (cross symbol: Measurements; full line: Simulation).

Figure 9: From a) to c), different positions of the infrared thermometers. The north is indicated. Source Pigeon (2004).

The brightness temperature of the Pomme route is best predicted (magenta line in Fig. 8b). The primary model-observation disagreement occurs on Pomme northeast face (cyan line in Fig. 8b) during the afternoon. The bias reaches 8°C. We can adopt the same explanation as for the Alsace road. Moreover, from some photos (Fig. 10), we find that there are numerous windows with white blind on this side of the wall. The infrared radiometer might detect a position where white blinds were closed therefore more solar radiation flux was reflected. Or windows were opened, the ventilation in the canopy led to a lower internal building temperature which decreased the external temperature. Finding a solution is a difficult task. Firstly, there is an uncertainty in the observation. Secondly, there is a need to model this wall in more details, maybe including the balcony in front walls and windows.

Figure 10: Photo of the Pomme northeast face, view from affixed IRT sensor. Source Pigeon (2004).

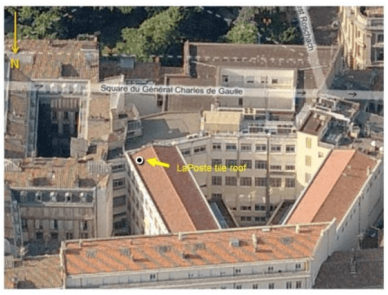

Figure 11: Aerial view of IRT position on the LaPoste roof from Bing Maps.

The modeled roof brightness temperature displays a good agreement with observation before sunrise and from late afternoon to midnight (Fig. 8c). However, the model exhibits significant advance in warming when the roof start being sunlit. Actually, the sensor detecting roof brightness temperature was fixed at a northern building's roof from the mast (Fig. 9c and Fig. 11). This building is treated as a simple block in the 3D model (Fig. 2). However, from Figure 9c and 11, we can observe the complex structure of the roof. In particular, there are some small obstacles which are higher than the measured roof to the

atmosphere MDPI

east but are not represented in the simulated scene. During the sunrise, the roof might be shaded due to these non modeled detail structures. From the late afternoon, the sun shifts to another side. Since no more small obstacles are higher than the measured roof, the bias disappears.

Outgoing long-wave radiative flux $L^{\uparrow}$

Figure 12 shows the model-observation comparison of long-wave radiation flux. The difference between the modeled outgoing long-wave radiation flux at roof surface (full line) and on the mast (dashed line) is generally less than 20 $W\ m^{-2}$. However, both of them give an underestimation of about 20 $W\ m^{-2}$ during the night and a maximum overestimation of about 100 $W\ m^{-2}$ in daytime. In fact, these differences are related to the error of on the roof temperature, i.e. underestimation in the night and overestimation in the day. We recall here, that the outgoing infrared radiation flux highly depends on the surface temperature because of the term of $\varepsilon\sigma T_{sfc}^4$.

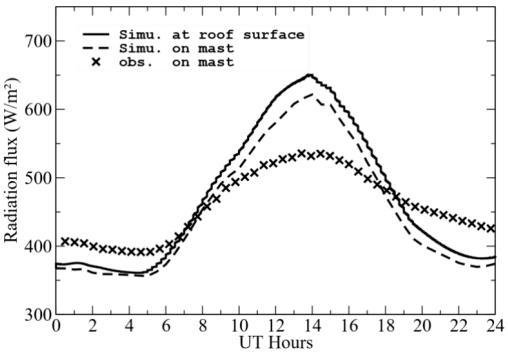

Figure 12: Diurnal variation of outgoing infrared flux calculated at roof surface (full line), at the mast level (dashed line) and measured on the mast (cross symbol).

To complete the discussion, we have the advantage with the model to be able to visualize the radiative flux in the computational domain. Fig. 13 illustrates the distribution of the outgoing infrared flux at 1030 UT on the vertical center-plane and on the building surfaces. Significant variability can be observed on the center-plane. Relatively high values are found at horizontal solid-air interface due to the fact that horizontal surfaces are warmer than the vertical surfaces in the daytime.

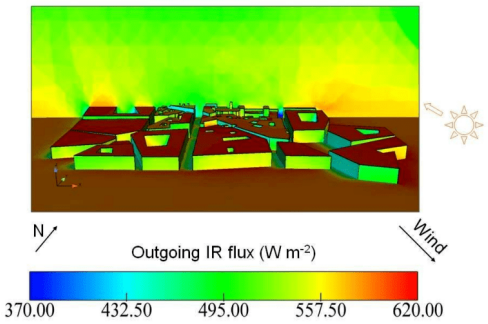

Figure 13: Visualization of the outgoing infrared flux on the center-plane and surfaces at 1030 UT. The north, wind and sun direction are indicated by arrows.

Outgoing global radiative flux $S^{\uparrow}$

Figure 14 compares the modeled upward global solar flux with the measured one. The non-zero measured nighttime solar flux may be due to the sensor errors or the artificial lights from shop-windows, cars and street-lamps (Hénon et al. 2012). The upward solar flux can be estimated by

$$S^{\uparrow} = \alpha(S_D + S_f + S_e)$$

where S_D $(W\ m^{-2})$ is the direct solar flux, S_f $(W\ m^{-2})$ the solar flux diffused by the atmosphere above, S_e $(W\ m^{-2})$ the flux diffused by the environment (i.e. from multi-reflection on the surfaces).

atmosphere

MDPI

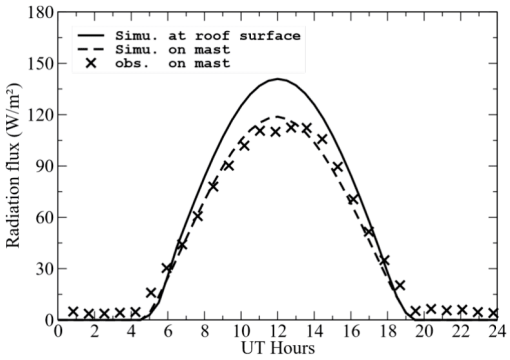

Figure 14: Same as Fig. 12 but for outgoing solar flux.

For this gray roof (Fig. 9b), we set an albedo of 0.15 (Table II). The same value is also proposed by Pigeon et al. (2008) ((2008)) and is used in Hénon et al. (2012) ((2012)). Compared to the observation, in spite of about 20 $W\ m^{-2}$ higher values at noon estimated by the model (full line), the agreement between measurement and modeled the outgoing solar flux on mast (dashed line) is very satisfactory.

In the same manner as for the long-wave radiative flux, in Figure 13 we display the distribution of the outgoing global solar flux at 1030 UT on the center-plane and on the surfaces. Through the visualization the propagation of the radiative flux in the fluid domain, we can better understand the distribution of the shadow projected by the different structures. We can also readily identify surfaces with higher albedo since they reflect more solar radiation flux.

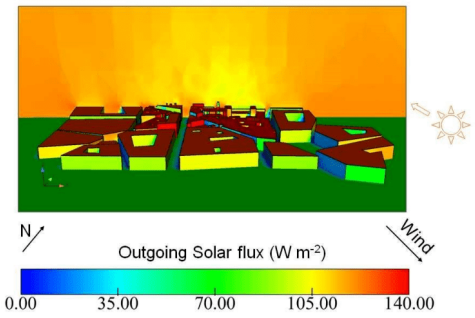

Figure 15: Same as Fig. 13 but for outgoing solar flux.

Sensible heat flux Q_H

Surface sensible heat flux is the energy exchanged between a surface and the air in the presence of a surface-air thermal gradient. Modeling the sensible heat flux contributes to determine both stratification effects on turbulent transport, and to estimate the surface temperature. At roof surface, the sensible heat flux Q_H can be parameterized as:

$$Q_H = h_f(T_a - T_{sfc}),$$

in which h_f $(W\ m^{-2}K^{-1})$ is the heat transfer coefficient and T_a (K) the air temperature.

The sensible heat flux at the surface can be recorded easily in the simulation and be compared to the value measured on the mast computed using eddy-covariance technique. It can be estimated at the mast level as follows:

$$\overline{w'\theta'} = K_t \frac{\partial \theta}{\partial z},$$

where $\overline{w'\theta'}$ is the potential temperature fluctuation, and eddy diffusivity K_t $(m^2\ s^{-1})$ by using turbulent viscosity ν_t $(m^2\ s^{-1})$ and constant turbulent Prandtl number Pr_t as $K_t = \nu_t / Pr_t$. In this work, we set Pr_t to be 1.0. Hence, $Q_H = \rho C_p \overline{w'\theta'}$.

atmosphere

MDPI

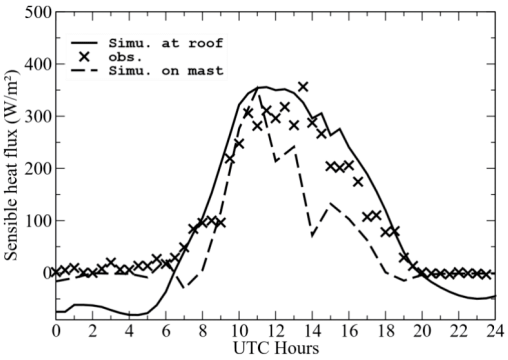

Figure 16: Same as Fig. 13 but for outgoing solar flux.

Figure 16 depicts the comparison between the time evolution of calculated sensible flux at roof surface and the mast observation. At roof, difference between observed and calculated values are less than 40 $W\ m^{-2}$, except for the night ($45-70\ W\ m^{-2}$). From midnight to 0700 UT, the wind is calm but does not have a zero speed (Fig. 4a) and the air temperature varies from 15 to 19°C (Fig. 4c). The observed sensible flux is very small (cross symbol in Fig. 16), this maybe due to the fact that the air layer just above the roof has a temperature very close the roof temperature. However, the initialized roof temperature at this position is set to the same value as the measured roof temperature 11.1°C in Table I). With a non zero heat transfer coefficient and a higher air temperature, consequently, negative sensible heat flux is obtained at roof surface (full line in Fig. 16). For the rest of the day the comparison is rather good. At the mast location, reasonable agreement generally exists between calculated and measured values. The differences are more pronounced from 1300UTC to 1500UTC. We are working on this point for better understanding the difference. The reason may be due to uncertainty from the measurements and not detailed geometries on the roofs, which has a local influence on the convective flux.

Model-Observation comparison of friction velocity u^*

Friction velocity u^* ($m\ s^{-1}$) is also measured on the mast during the CAPITOUL experiment. The u^* at the roof surface is defined by the relation:

$$u^* = (|\tau_w/\rho|)^{1/2},$$

where τ_w is the Reynolds stress at wall ($N\ m^{-2}$), ρ ($kg\ m^{-3}$) the fluid density at the wall.

In order to compare with the observation on the mast, we use the kinematic momentum fluxes in the x and y directions ($\overline{u'w'}$, $\overline{v'w'}$), therefore the friction velocity can be evaluated as:

$$u^* = (\overline{u'w'}^2 + \overline{v'w'}^2)^{1/4},$$

where $\overline{u'w'}$ and $\overline{v'w'}$ are given by:

$$\overline{u'w'} = \nu_t \frac{\partial \overline{u}}{\partial z}, \ \overline{v'w'} = \nu_t \frac{\partial \overline{v}}{\partial z},$$

and ν_t $(m^2\ s^{-1})$ is the turbulent viscosity given by the $k - \varepsilon$ closure.

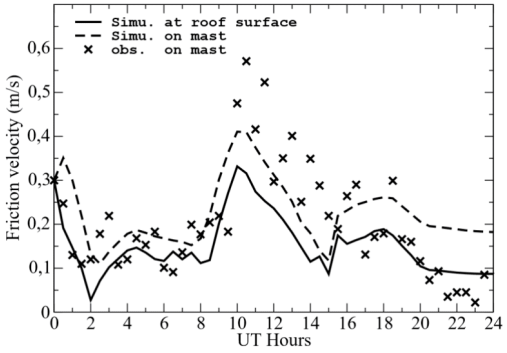

Figure 17: Same as Fig. 12 but for friction velocity.

From Figure 17 it can be seen that the simulated friction velocities are reasonable in terms of magnitude. Modeled friction velocity at roof surface (full line) shows a good agreement with observation when the u^* less than $0.2ms^{-1}$. Simulated u^* on mast (dashed line) can produce higher value $(0.4ms^{-1})$. It seems that the model overestimates the nighttime $(1800 - 2400$ UT) u^* on mast. However, estimates of u^* from the turbulence measurements by the sonic are known to be rather uncertain, especially when u^* is small. The difference between the modeled u^* at roof surface (full line) and at the mast level (dashed line) is due to different methods of the estimation, and the numerical errors in the computed gradients.

9. Conclusions and perspectives

We have investigated the energy exchanges in a real city with the atmosphere during the CAPITOUL campaign, using new atmospheric radiative and thermal schemes implemented in *Code_Saturne*. A pre-processing is realized including the optimization of the complex geometry and creation of a high quality tetrahedral mesh for this study. It also requires determining the complex thermal parameters which take into account the actual variability of materials in the district. Based on the literature data, we have separated the building surface into 4 categories of albedo depending on painting colors.

First, simulations are evaluated with the comparison with Thermal Infrared airborne images from two flights in the day of 15th July 2004 during the CAPITOUL project. The result shows the importance of taking into account heterogeneities in materials and

atmosphere MDPI

geometry to represent the spatial variability of the temperatures in complex urban areas. Then, we have evaluated the coupled dynamic-radiative model with CAPITOUL experiment including the comparison with the measured brightness temperature, sensible flux, radiative fluxes diurnal variation, and statistical values with hand-held IRT data. Overall the agreement between measurements and model simulations are fair but can be improved in the future with more information. For the sensible flux, the model-observation nighttime bias is probably linked to the uncertainty of the estimation on the roof nighttime temperature. Similar explanation can be used for the comparison of the outgoing infrared flux, because results are sensitive to the surface temperature. In fact, due to the complex geometries, a comparison of the IR flux in a simple case might be appropriate for understanding the difference and evaluating the model.

Better agreement is obtained for the comparison of the outgoing solar flux at the mast level. However, the difference between the modeled outgoing solar flux at roof surface and at the mast is still unclear. For the modeled friction velocities, the difficulty mainly appears to capture the extreme values (highest or lowest). Small structures may have important influence on the computation of local brightness surface temperature, sensible flux, outgoing short- and long-wave radiation. The simulation results shows the importance of modeling in details while doing local model-observation comparison. The statistical analysis, while comprehensive, is not exhaustive. Despite the fact that difference between measured and modeled averaged, median and standard deviation of brightness surface temperature may be significant, such comparison is very useful for a better understanding of the radiative transfer processes in the canopy.

The model results are encouraging and give insight into local surface-atmosphere processes, but further and more rigorous testing has to be performed, especially regarding vertical sensible flux and upward infrared flux.

Table I. Parameters applied in the CAPITOUL simulations

Parameter	Unit	Value
Dynamic		
Time-step	*s*	10
Zref	*m*	47.5
Uref	ms^{-1}	3.21
φ	◦	340
Roof z_0	*cm*	10
Wall z_0	*cm*	10
Street z_0	*cm*	2
Radiative		
Time-step	*min*	15
Roof z_{0T}	*cm*	10
Wall z_{0T}	*cm*	10
Street z_{0T}	*cm*	2
α_S		0.08
ε_R		0.9

ε_W		0.92
ε_S		0.95
λ_R	$W\,K^{-1}\,m^{-1}$	0.83
λ_W	$W\,K^{-1}\,m^{-1}$	1.15
eR	m	0.09
eW	m	0.3
μ_S	$J_m{-}2_s{-}0.5_K{-}1$	1330
Initial temperature values		
Tair	◦ C	18.86
Alsace East (outside/inside)	◦ C	22.36/22.94
Alsace Road (outside/inside)	◦ C	23.18/25
Alsace West (outside/inside)	◦ C	21.32/22.23
Pomme SSWest(outside/inside)	◦ C	24.70/25.55
Pomme Route (outside/inside)	◦ C	23.33/25
Pomme NNEast (outside/inside)	◦ C	29.06/29.78
LaPoste Roof (outside/inside)	◦ C	11.13/10.36

Table II. Albedo classification of the buildings surfaces

Paint color	albedo
White	0.6
Whitewash	0.5
Rose	0.3
Gray	0.15

10. References

Archambeau, F., N. Méchitoua, and M. Sakiz. 2003.“: a Finite Volume Code for the Computation of Turbulent Incompressible Flows - Industrial Applications.” *Int. J. Finite. Volumes* 1: 1–62 [Available online at http://www.latp.univ–mrs.fr//IJFVDB/saturne.pdf].

Bouyer, J., C. Inard, and M. Musy. 2011. “Microclimatic Coupling as a Solution to Improve Building Energy Simulation in an Urban Context.” *Energy and Buildings* 43 (7): 1549–59.

atmosphere MDPI

Chen, H., R. Ooka, H. Huang, and T. Tsuchiya. 2009. "Study on Mitigation Measures for Outdoor Thermal Environment on Present Urban Blocks in Tokyo Using Coupled Simulation." *Build. Environ.* 44 (11): 2290–9.

Deardorf, J. W. 1978. "Efficient Prediction of Ground Surface Temperature and Moisture with Inclusion of a Layer of Vegetation." *J. Geophys. Res.* 83: 1889–1903.

Fiveland, W. A. 1984. "Discrete-Ordinates Solutions of the Radiative Transport Equation for Rectangular Enclosure." *J. Heat Tran.* 106 (4): 699–706.

Gastellu-Etchegorry, J. P. 2008. "3D Modeling of Satellite Spectral Images, Radiation Budget and Energy Budget of Urban Landscapes." *Meteor. Atmos. Phys.* 102 (3-4): 187–207.

Gastellu-Etchegorry, J. P., E. Martin, and F. Gascon. 2004. "DART: A 3-D Model for Simulating Satellite Images and Surface Radiation Budget." *Int. J. of Remote Sens.* 25: 75–96.

Hénon, A. 2008. "Températures Mesurées, Modélisées, et Observées Par Télédétection Infrarouge, Dans La Canopée Urbaine: Modélisation Aéro-Thermo-Radiatif Des Flux de Chaleur Urbains." PhD thesis, École Centrale de Nantes.

Hénon, A., P. G. Mestayer, J. P. Lagouarde, and J. A. Voogt. 2012. "An Urban Neighborhood Temperature and Energy Study from the CAPITOUL Experiment with the SOLENE Model Part 1: Analysis of Flux Contributions." *Theor. Appl. Climatol.* 110 (1-2): 177–96.

Jesionek, K., and M. Bruse. 2003. "Impacts of Vegetation on the Microclimate: Modeling Standardized Building Structures with Different Greening Levels." In *Fifth Int. Conf. on Urban Climate*. Lodz, Poland (September 1-5, 2003).

Krayenhoff, E. S., and J. A. Voogt. 2007. "A Microscale Three-Dimensional Urban Energy Balance Model for Studying Surface Temperatures." *Bound.-Layer Meteor.* 123 (3): 433–61.

Lagouarde, J. P., A. Hénon, B. Kurz, P. Moreau, M. Irvine, J. Voogt, and P. Mestayer. 2010. "Modelling Daytime Thermal Infrared Directional Anisotropy over Toulouse City Centre." *Remote Sens. Environ.* 114 (1): 87–105.

Louis, J. 1979. "A Parametric Model of Vertical Eddy Fluxes in the Atmosphere." *Bound.-Layer Meteor.* 17 (2): 187–202.

Masson, V. 2000. "A Physically Based Scheme for the Urban Energy Budget in Atmospheric Models." *Bound.-Layer Meteor.* 94 (3): 357–97.

Masson, V., L. Gomes, G. Pigeon, C. Liousse, V. Pont, J. P. Lagouarde, J. Voogt, et al. 2008. "The Canopy and Aerosol Particles Interactions in TOulouse Urban Layer (CAPITOUL) Experiment." *Meteor. Atmos. Phys.* 102 (3-4): 135–57.

Masson, V., C. S. B Grimmond, and T. R. Oke. 2002. "Evaluation of the Town Energy Balance (TEB) Scheme with Direct Measurements from Dry Districts in Two Cities." *J. Appl. Meteor.* 41 (10): 1011–26.

Milliez, M. 2006. “Modélisation Micro-Météorologique En Milieu Urbain: Dispersion Des Polluants et Prise En Compte Des Effets Radiatifs.” PhD thesis, École des Ponts ParisTech. http://cerea.enpc.fr/fich/these_milliez.pdf

Milliez, M., and B. Carissimo. 2007. “Numerical Simulations of Pollutant Dispersion in an Idealized Urban Area for Different Meteorological Conditions.” *Bound.-Layer Meteor.* 122 (2): 321–42.

———. 2008. “CFD Modelling of Concentration Fluctuations in an Idealized Urban Area.” *Bound.-Layer Meteor.* 127 (2): 241–59.

Moscicki, M. A. 2007. “A Comparison of Modeled and Observed Surface Temperatures in Toulouse, France.” PhD thesis, The University of Western Ontario.

Musson-Genon, L., E. Dupont, and D. Wendum. 2007. “Reconstruction of the Surface-Layer Vertical Structure from Measurements of Wind, Temperature and Humidity at Two Levels.” *Bound.-Layer Meteor.* 124 (2): 235–50.

Pigeon, G., D. Legain, P. Durand, and V. Masson. 2007. “Anthropogenic Heat Release in an Old European Agglomeration (Toulouse, France).” *Int. J. Climatol.* 27 (14): 1969–81.

Pigeon, G., M. A. Moscicki, J. A. Voogt, and V. Masson. 2008. “Simulation of Fall and Winter Surfac Energy Balance over a Dense Urban Area Using the TEB Scheme.” *Meteorol. Atmos. Phys.* 102 (3-4): 159–71.

Qu, Y. 2011. “Three-Dimensional Modeling of Radiative and Convective Exchanges in the Urban Atmosphere.” PhD thesis, École des Ponts ParisTech / Université Paris-Est. http://cerea.enpc.fr/fich/yongfengthesisfinal.pdf

Qu, Y., M. Milliez, L. Musson-Genon, and B. Carissimo. 2011. “Micrometeorological Modeling of Radiative and Convective Effects with a Building-Resolving Code.” *J. Appl. Meteor. Climatol.* 50 (8): 1713–24.

———. 2012. “Numerical Study of the Thermal Effects of Buildings on Low-Speed Air-Flow Taking into Account 3D Atmospheric Radiation in Urban Canopy.” *J. Wind Eng. Ind. Aerodyn.* 104-106: 474–83.

Yee, E., and C. A. Biltoft. 2004. “Concentration Fluctuations Measurements in a Plume Dispersing Through a Regular Array of Obstacles.” *Bound.-Layer Meteorol.* 111 (3): 363–415.

2.2.5. Modélisation de l'atmosphère urbaine dans le cadre du projet EUREQUA

2.2.5.1. Contexte

Après mon doctorat, j'ai continué mes activités de recherche sur le sujet de la ville durable. L'outil développé dans le cadre de ma thèse sert à l'étude de situations de pollution atmosphérique dans l'atmosphère réelle stratifiée (qui ne sont pas modélisables en soufflerie). Les applications concernent à la fois la dispersion des polluants autour des sites industriels qui intéressent EDF et la pollution locale urbaine qui intéresse le Ministère de tutelle de l'Ecole des Ponts. Par ailleurs l'outil était aussi utilisé dans le cadre d'études prospectives de densification urbaine pour les aspects énergétiques et de qualité de l'air, et est utilisé avec cet objectif dans le cadre du projet ANR « EUREQUA » (Evaluation mUltidisciplinaire et Requalification Environnementale des QUArtiers).

EUREQUA est un projet financé par l'Agence Nationale pour la Recherche (ANR) qui a débuté en Mars 2012 et qui a pour objectif d'examiner les enjeux de la requalification environnementale de la ville à l'échelle des quartiers à Toulouse, Paris et Marseille. Ce projet adopte une approche méthodologique originale qui s'appuie sur une équipe pluridisciplinaire associant géographes, sociologues, physiciens de l'atmosphère, acousticiens et architectes, en collaboration avec des responsables du cadre de vie urbain. L'objectif est de faire émerger une conception de la qualité environnementale du cadre de vie qui articule une réflexion renouvelée sur la matérialité de l'environnement urbain (en particulier climat urbain, acoustique et qualité de l'air) et les approches sociales de la relation à l'environnement.

2.2.5.2. Organisations

Ce projet est coordonné par le Laboratoire Interdisciplinaire Solidarités, Sociétés,Territoires (LISST), associant des chercheurs de Météo-France, du Laboratoire Population Environnement Développement (LPED), du Laboratoire Architecture Ville Urbanisme Environnement (LAVUE), de l'Institut français des sciences et technologies des transports, de l'aménagement et des réseaux (IFSTTAR), du Centre d'Enseignement et de Recherche en Environnement Atmosphérique (CEREA), du Laboratoire de Recherche en Architecture (LRA), l'Institut d'Aménagement et d'Urbanisme de la Région d'Ile-de-France (IAU IdF), et les Ateliers Yves Lion.

2.2.5.3. Campagne de mesure

Dans ce travail de recherche, l'approche que nous utilisons combine campagnes expérimentales et modélisation intégrée. La première campagne de mesures a été réalisée en Juin 2013 à Marseille. Après un diagnostic territorial centré sur la qualité environnementale dans deux quartiers d'identification à Marseille, nous avons choisi le quartier de la Valbarelle (Fig2.a). En raison de la proximité d'axes routiers à fort trafic, la Valbarelle connaît aujourd'hui des niveaux de pollution atmosphérique et de nuisance sonore élevés. Les chercheurs multi-disciplinaires ont arpenté le quartier durant 4 jours. Empruntant un parcours prédéfini, nous avons effectué des mesures mobiles du microclimat et de la qualité de l'air ainsi que la prise d'images infrarouges thermiques et l'enregistrement du niveau sonore, ceci à 15 endroits différents du quartier. Un réseau de capteurs fixes a également été installé chez des particuliers et dans les parties communes d'immeubles. Il a enregistré l'évolution des paramètres météorologiques (température, vent, humidité) et les concentrations de polluants (NO2 et ozone).

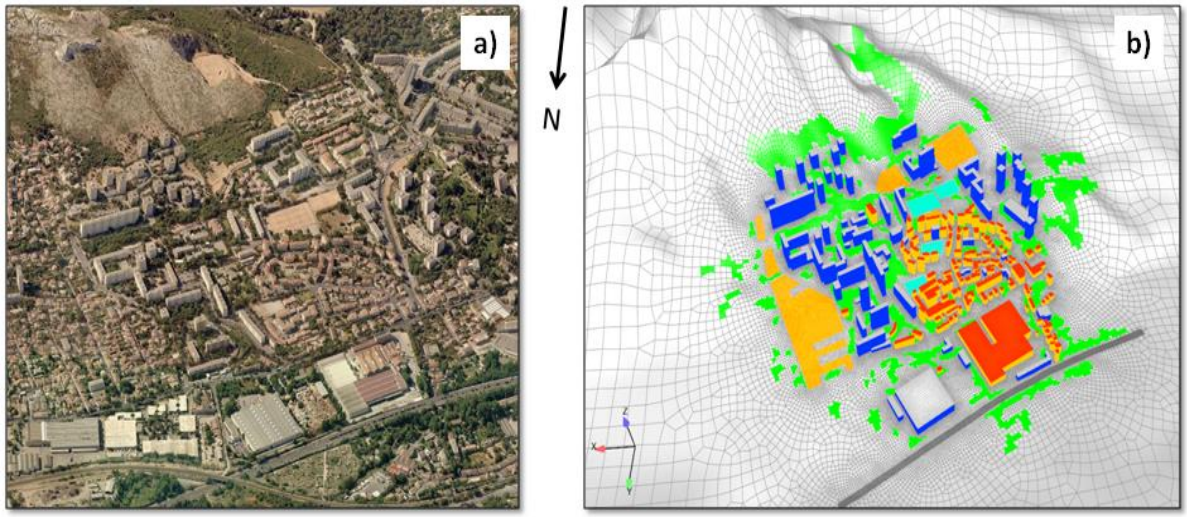

Fig2. a) Vue aérienne du quartier modélisé à Marseille ; b) Maillage réalisé comprenant les bâtiments (toits en rouge et gris), les blocs (en jaune), les terrains de sport (en bleu clair), la végétation (en vert), l'autoroute (en gris), le relief (en blanc). Le nord est indiqué.

Etant co-responsable des mesures thermiques des surfaces urbaines, j'ai participé aux campagnes de Marseille, Paris et Toulouse (Fig.3). J'ai profité de mon séjour au CEREA pour travailler tout particulièrement sur la modélisation fine du bilan énergétique de l'atmosphère urbaine dans 3 quartiers à Paris, Toulouse et Marseille afin d'étudier le confort thermique, la performance énergétique et la qualité de l'air.

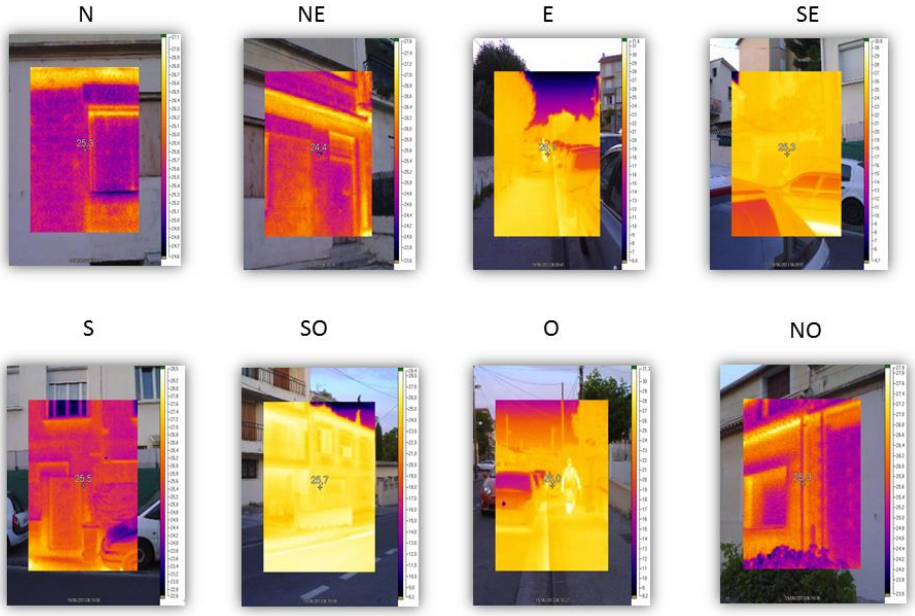

Fig3. Photos infrarouges superposées à l'image visible à un point de mesure suivant les 8 directions cardinales pendant la campagne à Marseille

En complément aux mesures physiques, des enquêtes ont été menées auprès des habitants et des usagers. Ils ont été invités à répondre à des questionnaires afin d' évaluer leur appréciation du lieu (entretien, esthétisme, sécurité, animation, etc.) ainsi que leur ressenti en matière de qualité de l'air et de confort sonore et thermique.

2.2.5.4. Génération du maillage

Les données géographiques sont fournies par l'Institut Géographique National (IGN). Elles se trouvent sous forme de plusieurs fichiers en format « *.shp » correspondant aux différents éléments de la ville. Etant donné que la base de données n'a pas été conçue pour des études de CFD, l'objectif de cette première étape est de simplifier et d'optimiser la géométrie 2D afin d'adapter notre simulation de la dispersion grâce à diverses étapes telles que : simplifier certaines formes de bâtiments, enlever des géométries à taille réduite, regrouper des petites maisons (ensembles pavillonnaires) sous un même bloc, ajouter des éléments marquants etc.

Après avoir créé une géométrie propre en 2D, on l'importe dans le logiciel de maillage open-source SALOME. Nous extrudons verticalement les bâtiments à partir de polygones 2D pour obtenir des bâtiments 3D et de l'information fournie par l'IGN sur les hauteurs de bâtiments. Sachant que le site a une topographie variée, nous ajoutons aussi le relief en utilisant également les

données de l'IGN sous format « *.asc » avec une résolution de 25x25m. Puis, nous maillons le site qui contient l'ensemble des structures urbaines (bâtiments, végétation, autoroutes, terrains de sport, relief, etc) avec une procédure automatisée sous SALOME. La Figure 2 montre le domaine de simulation et le maillage, qui est un maillage non structuré d'environ 6 millions de mailles hexaédriques. La résolution minimum de grille est de 1 m.

2.2.5.5. Résultats

Afin d'illustrer notre maquette numérique, je présente ici une étude numérique sans comparaisons avec les mesures. J'ai simulé un cycle diurne de l'évolution de l'atmosphérique du quartier et de la dispersion des polluants rejetés par l'autoroute dans la zone étudiée sous des conditions météorologiques d'une autre campagne de mesure déjà exploitée.

2.2.5.4.1. Dynamique

Un des principaux effets de la canopée urbaine est un ralentissement local de l'écoulement et une augmentation de la turbulence. L'effet de la végétation (la force de traînée) sur la dynamique de l'écoulement est pris en compte avec un modèle de porosité (**Zaïdi et al., 2013**). J'ai utilisé une rugosité importante pour les zones à forte densité. La figure 4 présente le champ d'énergie cinétique turbulente (TKE) au sol qui caractérise les fluctuations de vent (sans modéliser le relief dans un premier temps). Le vent en amont est d'Ouest en Est. La présence d'obstacles ralentit l'écoulement et crée une augmentation hétérogène de la TKE. Afin d'étudier l'écoulement proche de la végétation, j'ai comparé les résultats entre un cas utilisant le modèle de rugosité (Fig.4a) et un cas ayant recours au modèle de porosité (Fig.4b). Comme escompté, le modèle de porosité freine le fluide, avec une diminution de la TKE dès l'amont par rapport au modèle de rugosité dans les zones de végétation. Il conduit à une estimation plus réaliste de la dynamique de l'écoulement.

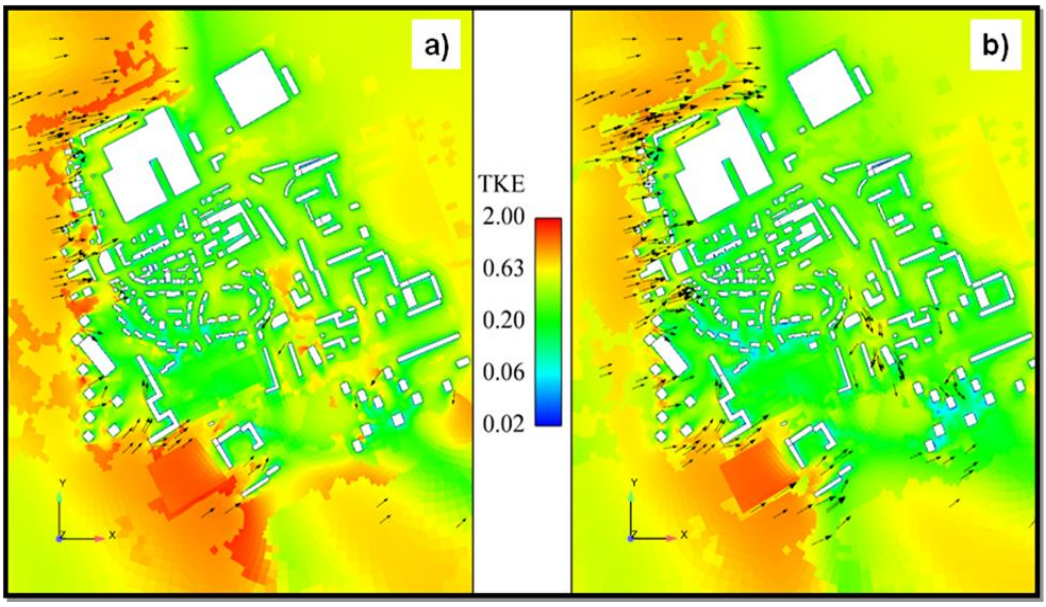

Fig4. Plans de coupe horizontaux de champs de l'énergie cinétique turbulente (TKE) (m^2/s^2) au sol : a) simulation avec le modèle de rugosité ; b) simulation avec le modèle de porosité

2.2.5.4.2. Thermique

Afin de mieux prendre en compte le rayonnement atmosphérique et les effets thermiques des bâtiments, on distingue deux types de bâtiment à partir des photos : immeubles (toits en gris sur Fig. 2b), maisons (toits en rouge sur Fig. 2b). Pour les paramètres thermiques, on s'inspire des valeurs recueillies dans la littérature (**Oke, 1987; Stewart et Oke, 2012**). En sortie de simulation thermo-radiative, on obtient les températures de surface ainsi que les flux InfraRouges (IR) incidents pour chaque maille et pour chaque pas de temps. On peut alors convertir les températures de surface en températures de brillance (Tbr (°C)). Ces dernières peuvent ensuite être comparées à celles obtenues par la caméra thermique IR. La figure 5 affiche les températures de brillance à 3h00 sur le modèle 3D avec un zoom sur un point d'arrêt pendant le parcours de la Période d'Observation Intensive (POI), en utilisant une échelle de couleur de la caméra IR. Les températures simulées rendent bien compte de la variabilité spatiale de la température d'éléments urbains.

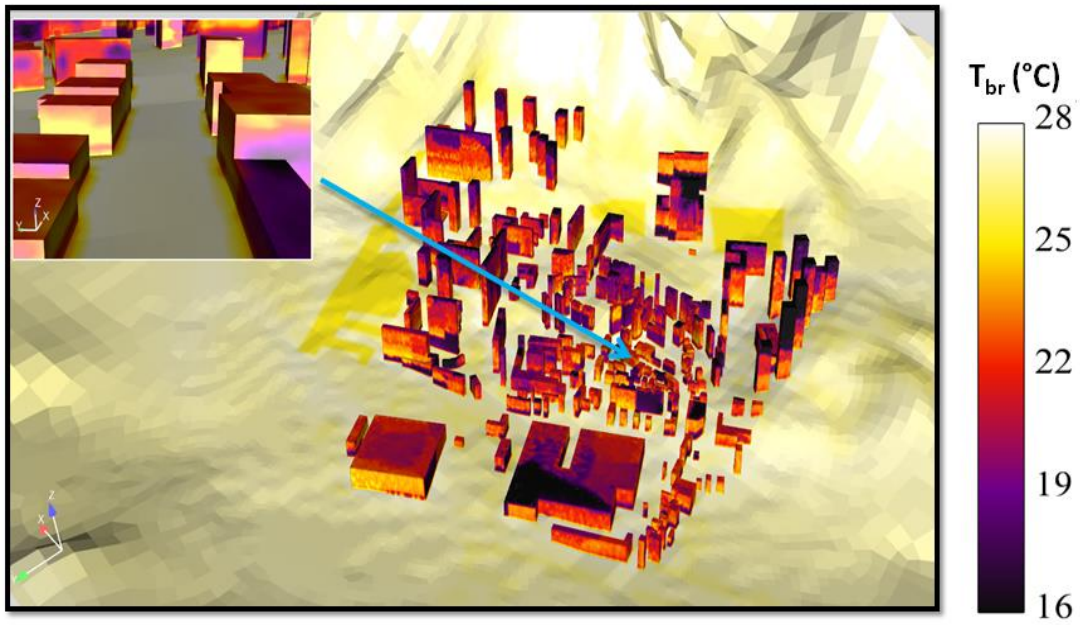

Fig5. Température de brillance simulée à 3h00 avec une vue zoomée sur un point d'arrêt pendant le parcours de la période d'observation intensive

2.2.5.4.3. Dispersion

Il existe de nombreuses sources de pollution urbaine et de types d'émissions : polluant réactif ou passif, source ponctuelle, surfacique ou volumique, source mobile ou fixe etc. L'étude numérique que je présente ici est relative à un rejet continu de polluant non réactif, provenant de l'autoroute. La figure 6 illustre la concentration d'un polluant passif adimensionnelle à 2 m du sol à 11h00 dans le quartier pour un vent incident de sud-est. Il met en évidence l'impact de la pollution due au trafic sur la direction de l'axe du panache au-dessus de la canopée, et la dispersion à travers les forêts et les rues. La dispersion horizontale est fortement influencée par les bâtiments et la direction de l'écoulement. Le polluant est piégé près des bâtiments proches de l'autoroute, où les concentrations sont élevées.

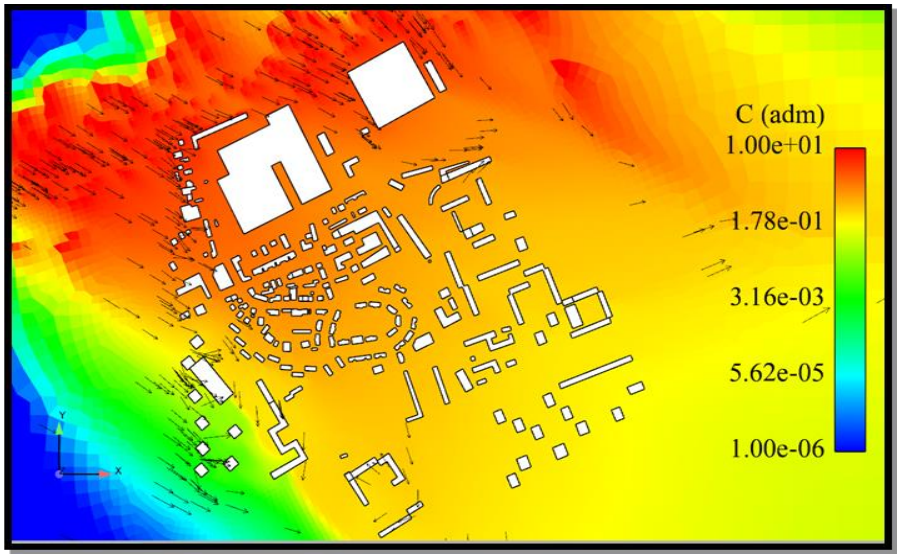

Fig6. Plan de coupe horizontal de champ de concentration d'un polluant passif adimensionnelle, à une hauteur d'un humain z = 2 m, à 11h00

2.3. CONCLUSION

Le travail présenté dans ce chapitre résume la modélisation de l'atmosphère en milieu urbain, à l'aide de simulations numériques avec le code de CFD Code_Saturne. Le modèle développé est un couplage thermo-radiatif-convectif. La validation de ce couplage est effectuée avec les mesures de la campagne de mesures américaines Mock Urban Setting Test (MUST) sur des géométries simples et ensuite avec les données expérimentales de la campagne Canopy and Aerosol Particles Interactions in TOulouse Urban Layer (CAPITOUL) sur un environnement urbain réel.

J'ai établi une méthodologie afin d'engendrer des maillages pour des sites très complexes. J'ai aussi testé un modèle de rugosité et un modèle de porosité pour prendre en compte l'effet de la végétation sur la dynamique de l'écoulement dans le cadre du projet ANR « EUREQUA ». En outre, j'ai souligné l'importance des effets de stabilité atmosphérique propre à la canopée, en particulier pour la modélisation des échanges thermo-radiatifs. Les simulations de mécanique des fluides numériques serviront d'appui à des études sur la qualité de l'air, le bruit et le confort thermique et seront comparées aux résultats subjectifs des enquêtes réalisées auprès des habitants. Une simulation d'aménagement en changeant la géométrie de bâtiments pourrait porter des éléments de réflexion vers une amélioration de la qualité de l'air local.

3.
MODÉLISATION NUMÉRIQUE DU BOIL-OFF GAS NATUREL LIQUÉFIÉ POUR DEVELOPPER DES SOLUTIONS LOGICIELLES D'OPTIMISATION DE LA GESTION DE LA CARGAISON ET DES OPÉRATIONS DU NAVIRE

3.1. PROBLEMATIQUE ET OBJECTIFS

Les nouvelles réglementations sur les émissions de gaz dans l'atmosphère dans l'industrie marine, ont fait du GNL une énergie alternative au fioul lourd. En effet le GNL est considéré aujourd'hui comme le carburant du futur dans la marine marchande. Sa faible émission en gaz à effet de serre ainsi que son coût le placent dans une position favorable pour remplacer les énergies fossiles conventionnelles.

Les prochaines années verront donc le développement des technologies et des infrastructures de stockage, de transfert et de transport de GNL de petites capacités pour répondre aux besoins du marché de l'utilisation du GNL comme carburant marin. Des défis techniques majeurs restent cependant à relever, notamment sur le comportement thermodynamique des fluides stockés.

Mon activité actuelle s'inscrit dans le domaine du transport et le stockage du GNL. Les thématiques de recherche que je développe sont fortement connectées aux axes de recherche de GTT : études d'avant-projet pour les chantiers navals dans la cadre de construction ; expertise auprès de armateurs, affréteurs, sociétés pétrolières de classification ; l'utilisation du GNL comme carburant pour la propulsion des navires (le bunkering) et du développement des petits et moyens transporteurs marins et fluviaux.

En qualité d'expert reconnu en système de confinement, en ingénierie des systèmes et en ingénierie cryogénique, GTT est sollicitée régulièrement pour des études dans le cadre des projets précités. La réalisation de ces prestations de services auprès des acteurs principaux du GNL permet à GTT d'entretenir des relations stables et durables avec l'ensemble de ces acteurs et ainsi de renforcer la confiance accordée à ses technologies, à son savoir-faire et à ses équipes.

Dans ce contexte, mon activité de recherche vise à développer des modèles et des techniques expérimentales innovantes pour améliorer la compréhension de phénomènes physiques dans la cuve, dans le but de développer des solutions pour améliorer la performance énergétique des méthaniers en opération.

Dans cet objectif, j'ai cherché à développer les connaissances acquises lors de ma formation de recherche (développement des modèles numériques et de mesure) afin de consolider et d'étendre l'activité de recherche de GTT, notamment vers

des services spécifiques à ses technologies. Cette expertise est un élément clé de l'offre commerciale de GTT et une source de confiance essentielle pour ses clients.

3.2. ETAT DE L'ART AU STADE INITIAL

Tout apport de chaleur dans un équipement ou une installation qui contient du GNL conduit à sa vaporisation partielle appelée Boil-off Gas ou « gaz d'évaporation ». S'il n'est pas évacué, le BOG s'accumule, entraînant ainsi une montée en pression. Sur les méthaniers, en exploitation normale, des compresseurs permettent de maintenir la pression stable dans les cuves ; ils évacuent le BOG vers les moteurs ou des torchères lorsque le BOG disponible dépasse les besoins moteurs. Le taux journalier d'évaporation sur un méthanier est de 0,05 à 0,15 %.

La plupart des études déjà abordées dans la littérature ont porté sur l'estimation de la performance thermique de la cuve en conditions design. Ce travail est fait sous certaines hypothèses de modélisation ne prenant pas en compte les aspects opérationnels. En effet, le navire est supposé statique et stationnaire, avec des cuves pleines, à température extérieure fixée, à température du liquide fixée, avec échange de chaleur purement par conduction, et avec du GNL supposé être du méthane pur.

D'autres études ont aussi porté sur la modélisation du comportement du GNL dans les bacs de stockage terrestre avec pour principale finalité d'étudier le phénomène de " roll over " dans une configuration statique.

Jusqu'à aujourd'hui, très peu de travaux numériques ou expérimentaux ont été faits pour étudier le comportement du GNL dans des cuves de méthanier pendant son transport. On peut malgré tout citer les quelques références bibliographiques listées ci-dessous. **Chez Hasan et al. (2009)** le BOG produit est estimé en calculant la chaleur totale gagnée par le talon liquide en conditions ballast basé sur sa capacité calorifique. **Miana et al. (2016)** font ces calculs avec des outils avancés de Computational Fluid Dynamics (CFD). De plus les modèles d'évaporation supposent en général une cuve statique **(Dimopoulos et al. 2008**). Cependant, les mouvements de la cuve et du liquide transporté engendrés par les vagues jouent un rôle important sur le BOG, ce qui n'est pas pris en compte dans ces études. Le vieillissement du GNL (c'est-à-dire l'évolution de sa composition au cours du temps) est également un facteur influençant significativement le taux

d'évaporation du GNL et qui n'est pas pris en compte dans les modèles de la littérature.

La complexité des phénomènes physiques observés requiert une modélisation fine du comportement du GNL en prenant en compte les aspects dynamique, multiphasique, multi-espèce et multi-échelle dans l'établissement des lois physiques et des modèles. À ces approches, il faut ajouter la modélisation de l'impact des mouvements de la mer sur le comportement thermique et thermodynamique du GNL durant son transport en particulier sur le taux d'évaporation. Les méthodes existantes ne permettent donc pas aujourd'hui d'étudier de manière précise le comportement du GNL en navigation.

En ce qui concerne les logiciels embarqués d'aide à la décision existants, aucun ne prend en compte la spécificité des méthaniers, à savoir que la cargaison (le GNL) est aussi le carburant, et que cette cargaison s'évapore en permanence au cours du voyage. L'approche est en effet concentrée sur la performance des moteurs, ce qui est une question essentielle sur les navires de croisière ou les porte-conteneurs par exemple, alors que c'est une question secondaire sur un méthanier.

En ce qui concerne la partie expérimentale et de collecte de données, la maîtrise du phénomène d'évaporation du GNL (le boil-off) au cours de son transport par voie maritime est un sujet inexploré alors que ces pertes sont significatives. Avant le début de ce projet, il n'existait pas dans le transport maritime de GNL de bonnes pratiques opérationnelles identifiées et partagées par l'ensemble des acteurs, ou même au sein d'une même société. En effet, à chaque relève d'équipage, nous avons remarqué que les pratiques étaient différentes.

Les seules informations accessibles (en interne et chez les opérateurs avec lesquels nous avons travaillé) concernaient le taux d'évaporation en conditions architecture (donc conditions idéalisées). C'est donc une information éloignée des problématiques opérationnelles et peu valorisables pour réduire ces pertes en opération.

L'autre information disponible en interne et chez les opérateurs concernait le refroidissement des cuves (par spraying) en fin de voyage ballast. Là encore, la seule information disponible était une valeur calculée en conditions architecture, donc difficilement valorisable en vue d'optimiser les opérations.

Chez GTT, toute connaissance sur le sujet s'arrêtait aux problématiques de conception. Il n'y avait aucune connaissance sur l'optimisation opérationnelle. La campagne de mesure et de collecte de données a permis d'avoir des informations sur le comportement réel d'un méthanier en opération, nécessaire et indispensable à la compréhension des phénomènes physiques complexes qui prennent place dans la cuve.

3.3. TRAVAUX REALISES

Dans ce contexte, mes activités chez GTT se centrent donc autour de la compréhension du phénomène physique dénommé Boil-Off Gas, afin de développer des solutions pour améliorer la performance énergétique des méthaniers en opération.

Les efforts de développement ont été de deux types : théoriques dans un premier temps, puis pratiques et expérimentaux (cf. thème suivant). Concernant la partie théorique, l'objectif était de développer un modèle de comportement du méthanier afin de prédire la quantité de gaz d'évaporation générée par la cuve et prévoir la consommation des moteurs avec prise en compte des éléments suivants :

- transfert thermique dans le Cargo Containment Systems
- effet de l'agitation du navire et du liquide dans les cuves sur l'évaporation
- échanges entre les phases liquide et gaz
- vieillissement du GNL (évolution de sa composition au cours du temps)

Avec notre partenaire universitaire ENSIC, nous avons travaillé au développement d'un modèle du vieillissement du GNL et d'un modèle de spraying. Nous avons aussi organisé une collaboration de recherche avec une thèse CIFRE pour modéliser plus finement le comportement thermique et thermodynamique du GNL et son environnement.

Dès 2014, j'ai travaillé sur le projet « Smart Boil-off ». Les premières difficultés techniques rencontrées concernaient la modélisation du comportement de la cargaison d'un méthanier :

- modélisation de l'effet de l'agitation du navire et du liquide dans les cuves sur l'évaporation

- modélisation des échanges entre les phases liquide et gaz
- modélisation du vieillissement du GNL (évolution de sa composition au cours du temps)

Ces modèles développés expérimentalement ont été intégrés à « Simulateur Boil-off » (SBO) au cours du projet.

Progressivement, les difficultés techniques sont apparues au niveau de la performance numérique du modèle, à savoir :

- Garantir la stabilité numérique du modèle (pas de divergence)
- Accélérer d'un facteur 2000 le temps de calcul du modèle pour le logiciel embarqué
- Développer un modèle de tenue à la mer d'un méthanier (prédire les mouvements du navire en fonction des conditions météo) avec des temps de calcul ultrarapide (inférieur à 0.01 milliseconde par calcul)

Après la phase de travail sur la performance numérique, les difficultés techniques se sont situées au niveau de la connexion des différentes briques logicielles.

Le travail d'intégration visera à vérifier expérimentalement les modèles de prédiction et d'optimisation de la performance énergétique du navire, notamment l'évaporation du GNL dans les cuves. Il permettra, dans un second temps, d'améliorer la précision de ces modèles.

Suite au projet « Smart Boil-off », j'ai continué à développer le modèle physique et à piloter le développement d'une plateforme multi-physique intégrant les différents métiers autours de la cuve (BOR architecture, BOR effectif, Comportement du GNL en conditions opérationnelles, Montée en pression, Transferts cuve à cuve, comportement mécanique et thermique de la mousse, transferts thermiques dans les CCS).

En parallèle, une coopération a été menée avec Ariane Group pour mieux comprendre / quantifier l'impact du flux de chaleur et du mouvement du liquide sur le taux de BOG. Une série d'essais cryogéniques avec du méthane liquide pur et un mélange défini méthane/éthane ou méthane/azote avec différents flux de chaleur entrants a été réalisée. La première partie consiste en des tests en Boil-off, la seconde en des tests de montée en pression.

3.3.1. Moyens et résultats

L'activité de recherche sur l'étude du comportement du GNL s'appuie sur des moyens expérimentaux et sur des modèles numériques. Comme indiqué dans l'état de l'art (c.f paragraphe 3.2), la plupart des études déjà abordées dans les publications scientifiques ont porté sur l'estimation de la performance thermique de la cuve en conditions design. Ce travail est réalisé selon certaines hypothèses de modélisation ne prenant pas en compte les aspects opérationnels. En effet, le navire est supposé statique et stationnaire, avec des cuves pleines, à température extérieure fixée, à température du liquide fixée, avec échange de chaleur purement par conduction, et avec du GNL supposé être du méthane pur.

D'autres études ont aussi porté sur la modélisation du comportement du GNL dans les bacs de stockage terrestre avec pour principale finalité d'étudier le phénomène de "roll over" dans une configuration statique. A ce jour, très peu de travaux numériques ou expérimentaux ont été faits pour étudier le comportement du GNL dans des cuves de méthanier pendant son transport.

Le modèle numérique que je développe dans le contexte de mon activité de recherche est zéro-dimensionnel (0D). L'objectif principal est de concevoir la solution embarquée permettant de modéliser les phénomènes physiques du GNL en tenant compte des aspects dynamique, multiphasique, multi-espèce et multi-échelle. Il s'agit également d'ajouter la modélisation de l'impact des mouvements de la mer sur le comportement thermique et thermodynamique du GNL durant son transport, en particulier sur le taux d'évaporation. Le choix du modèle 0D a été guidé par le temps calcul, tout en atteignant un degré de précision suffisant pour nos applications (**Qu et al. 2018**).

Référence:

Qu, Y., Noba, I., Xu, X., Privat, R., Jaubert, J-N., A thermal and thermodynamic code for the computation of Boil-Off Gas – Industrial applications of LNG carrier, Cryogenics (2018), doi: https://doi.org/10.1016/j.cryogenics.2018.09.002

Cryogenics 99 (2019) 105–113

Contents lists available at ScienceDirect

Cryogenics

journal homepage: www.elsevier.com/locate/cryogenics

Research paper

A thermal and thermodynamic code for the computation of Boil-Off Gas – Industrial applications of LNG carrier

Yongfeng Qu[a,*], Ibrahima Noba[a], Xiaochun Xu[b], Romain Privat[b], Jean-Noël Jaubert[b]

[a] GTT (Gaztransport & Technigaz) SA, 1 Route de Versailles, 78470 Saint-Rémy-lès-Chevreuse, France
[b] Université de Lorraine, École Nationale Supérieure des Industries Chimiques, Laboratoire Réactions et Génie des Procédés (UMR CNRS 7274), 1 rue Grandville, 54000 Nancy, France

ARTICLE INFO

Keywords:
LNG
Boil-Off Rate
Boil-Off Gas
Cargo containment systems
Thermal transfer
Thermodynamic

ABSTRACT

This paper describes the numerical method implemented in Gaztransport & Technigaz specific-purpose thermal and thermodynamic code for complex physical phenomena in Liquefied Natural Gas (LNG) carrier tanks. The code is zero-dimensional and is used for LNG industrial applications and research activities in several fields related to Boil-off Gas (generation, consumption, optimization, etc.).

The set of equations considered consists of the LNG and NG mass and energy conservation equations completed with equation of state and equations for LNG aging modeling. An explicit time-marching scheme with multiple-order methods is used. Specific effort has been put into the fast computation of the thermodynamic and transport properties of LNG. The implemented physical approaches have been validated by operational data.

Better management of Boil-off represents a significant operational challenge for players in the LNG chain. Industrial applications illustrate important aspects of physical modeling such as saturation properties, thermal layer and sloshing. These examples also demonstrate the capability of the code to tackle a large variety of LNG carrier operating conditions and tank geometries.

1. Introduction

Currently, there are over 400 Liquefied Natural Gas (LNG) carriers in operation around the world. Gaztransport & Technigaz (GTT) membrane-type LNG tanks (e.g. Mark or NO series) are wildly used in these carriers because of their reliability in the safe storage of LNG, efficient insulation and competitive edge. However, due to the tank's cryogenic nature, a fraction of the cargo LNG volume evaporates during the voyage. This evaporated volume often goes by the name Boil-Off Gas (BOG). Quantifying the BOG is important for the technical and economic assessment of the marine energy systems of LNG carriers.

Over the past decade, numerical simulation has become an increasingly LNG industrial tool for design, performance improvement and analysis of operating conditions for economic and environmental reasons. Such an evolution has been made possible by factors such as the massive increase in computer capacities and the improvement of in-house and commercial software. Sharafian et al. [1] summarized some relevant thermodynamic studies on LNG infrastructures. As the commercial software, Aspen HYSYS and Aspen Plus [2] are mostly used in the market for predicting the thermos-phyiscal properties of LNG over time under liquid-vapor equilibrium and non-equilibrium conditions [3–7].

As for in-house codes, Chen et al. [8] developed the thermodynamic and heat transfer methods to analyze the pressure and temperature changes in a cryogenic tank of 15,000 Gal at an LNG station. Sharafian et al. [1] also presented their model to analyze LNG storage tanks of refueling stations by considering the thermal mass of storage tank and use real operating temperatures and pressures.

LNG weathering is a key influencing the BOG production. The composition of LNG will change and that will influence not only its thermodynamic properties but also its heating value. A number of researchers have investigated LNG weathering prediction. Pellegrini et al. [9] and Migliore et al. [10] presented two weathering models for LNG stored in above-ground tanks based on mass and energy balance, but without the assumption of constant BOR. The models are LNG vapor-liquid equilibrium models. Later, Migliore et al. [11] improved their model by using a non-equilibrium approach to predict the individual temperature evolution of the vapor and liquid phases during the depressurization process.

Regarding the studies on the LNG carriers, Tanudjaja and Lanquetin [12] explored the reduction of fuel consumption on an LNG carrier by retaining a low heel onboard. Ait Ferhat et al. [13] conducted a thermal

* Corresponding author.
E-mail address: yongfeng.qu@gmail.com (Y. Qu).

https://doi.org/10.1016/j.cryogenics.2018.09.002
Received 14 May 2018; Received in revised form 7 September 2018; Accepted 10 September 2018
Available online 11 September 2018

Nomenclature

C_p	specific heat capacity of the barrier (J·kg^{-1}·K^{-1})
D	LNG thermal diffusivity (m^2·S^{-1})
e	thermal layer (m)
E_{total}	total energy in LNG or NG (W)
h	convective exchange coefficient between fluid and the primary barrier of the CCS (W·K^{-1}·m^{-2})
h_t	enthalpy due to condensation, flashing or boil-off gas (J·kg^{-1})
L	wall length (m)
Lv	specific latent heat (kJ·kg^{-1})
K	conductance (W·K^{-1}·m^{-2})
k	volatility
l	thickness (m)
M	molar mass (kg·mol^{-1})
m	mass (kg)
$\dot{m}$	mass flow rate (kg·s^{-1})
n	molar number
Nu	Nusselt number
P	pressure (Pa)
Pr	Prandtl number
R	gas constant (J·mol^{-1}·K^{-1})
Re	Reynolds number
S	exchanged surface (m^2)
t	time (s)
dt	timestep (s)
U_i	thermal transmittance of each compartment face I (J·m^2·K^{-1})
v	molar volume (m^3·mol^{-1})
w_{tank}	tank width (m)
x	molar fraction for liquid
y	molar fraction for gas

Greek symbols

α	accommodation coefficient
β	thermal expansion coefficient (K^{-1})
δ	condensate layer (m)
θ	slant angle (°)
λ	conductivity (W·m^{-1}·K^{-1})
u_m	wave propagation speed (m·s^{-1})
μ	chemical potentials
ν	fluid kinematic viscosity (m^2·S^{-1})
ρ	density (kg·m^{-3})
$\varnothing_{tilting}$	angle of inclination of the ship compared to its static position (°)
Φ	total heat flux (W)
Φ^c	thermal convective flux between fluid and the primary barrier of the CCS (W)
$\Phi^{r_{net}}$	net radiative flux (W)
Φ^{cd}_{ng-lng}	thermal exchange between LNG and NG at the free surface by conduction (W)
ω_i	acentric factor
$\omega_{sloshing}$	waves' frequency (s^{-1})

Subscripts

lng	liquid
ng	gas
bog	evaporated
cond	condensed
flash	vaporized LNG by flashing
out	natural gas coming out of the tank
CCS	membrane cargo containment systems
steel	inner hull
wall	primary barrier of the CCS
comp	compartment
sat	saturation
ci	critical

study on the interaction of an LNG tank system with the environment. Miana et al. [14] calculated the Boil-Off Rate when shipped in Mark III tanks with four schemes of increasing complexity.

All these studies are generally meant for the design of LNG storage tanks. Moreover, evaporation-resolving models usually assume a static tank [15]. For each membrane LNG carrier, the design daily Boil-Off Rate (BOR) of cargo during laden voyage is usually theoretically determined by calculating the heat flow received by LNG, assuming the International Gas Code (IGC) conditions: 45 °C for ambient air temperature, 32 °C sea water temperature, cofferdams temperature maintained at 5 °C, cargo tanks filled at 98% of the total capacity with pure methane (density 425 kg/m^3, latent heat of vaporization 511 kJ/kg), cargo piping empty.

The different LNG carrier's environment factors and their interactions make the Boil-Off complex to estimate and/or compute beforehand for different voyages and scenarios. In addition, tank motions arising from the sea waves play an important role in the BOG. Further research is therefore necessary to improve our understanding of BOR in the LNG carrier's environment.

At GTT, development of in-house codes has been a resolute strategic choice for more than several years. In particular, for problems requiring better management of cargo and of Boil-off, specific effort had been put into in-house "specific-purpose code". The objective of these developments is to propose solutions to optimize Boil-off based on models of the thermodynamic behavior of cargo by taking into account all of the factors that affect the BOR.

Therefore, a zero-dimensional thermal and thermodynamic code has been developed by GTT under quality assurance and is used at GTT in various industrial fields such as onboard service, process engineering (self-pressurization, spraying, ship-to-ship transfer, etc.), and new Cargo Containment System (CCS) design.

This article presents the development of this code. An overview of several studies is proposed to illustrate some industrial applications that are being carried out with the code. Eventually, perspectives for future development are briefly put forward.

2. Equations and model design

The code can handle all membrane-type tanks and complex physics (Fig. 1). The numerical model is based on the mass and energy balances in liquid and gas systems. The following section summarizes the main hypotheses and the equations. We consider an element adding to the system is positive (+), and an element leaving from the system is negative (−).

The main hypotheses are as follows:

- LNG and NG temperatures are homogeneous
- Tank pressure in NG is homogeneous and is identic in each tank
- Dry wall and wet wall temperatures are homogeneous
- Temperature in the cofferdam zones is homogeneous and constant

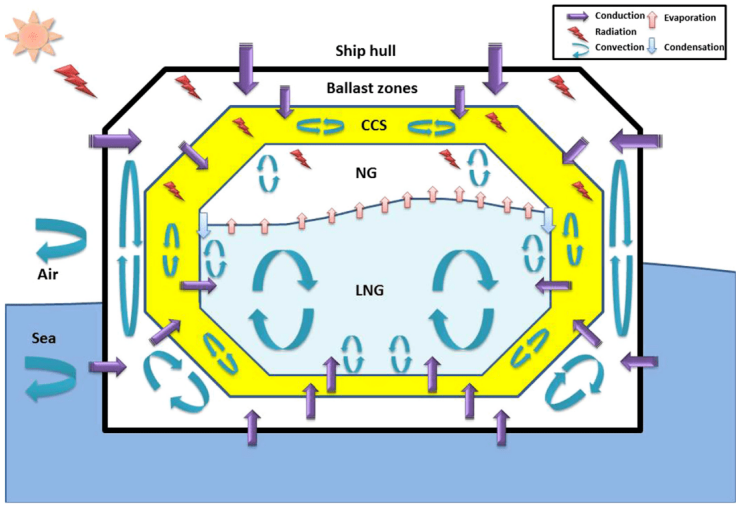

Fig. 1. Schematic representation of the different physical phenomena in the tank.

2.1. Conservation laws

We consider the following system of continuous equations for mass of the LNG and NG phase:

$$\frac{dm_{lng}}{dt} = -\dot{m}_{bog} + \dot{m}_{cond} - \dot{m}_{flash} \quad (1)$$

$$\frac{dm_{ng}}{dt} = \dot{m}_{bog} - \dot{m}_{cond} + \dot{m}_{flash} - \dot{m}_{out} \quad (2)$$

where m_{lng} (kg) and m_{ng} (kg) are LNG and NG mass respectively, $\dot{m}_{bog}$ (kgÂ·s^{-1}) is the free surface evaporation mass flow rate, $\dot{m}_{cond}$ (kgÂ·s^{-1}) and $\dot{m}_{flash}$ (kgÂ·s^{-1}) are the condensation and flashing mass flow rate. $\dot{m}_{out}$ (kgÂ·s^{-1}) is the NG mass flow coming out of the tank.

For energy balance we also distinguish the LNG and NG phase:

$$\frac{dE_{total_{lng}}}{dt} = \Phi^{c}_{lng} + \Phi^{fnet}_{lng} + \Phi^{cd}_{ng\to lng} - \dot{m}_{bog}h_{t_{bog}} + \dot{m}_{cond}h_{t_{cond}} - \dot{m}_{flash}h_{t_{flash}} \quad (3)$$

$$\frac{dE_{total_{ng}}}{dt} = \Phi^{c}_{ng} + \Phi^{fnet}_{ng} - \Phi^{cd}_{ng\to lng} + \dot{m}_{bog}h_{t_{bog}} - \dot{m}_{cond}h_{t_{cond}} + \dot{m}_{flash}h_{t_{flash}} - \dot{m}_{out}h_{t_{out}} \quad (4)$$

where E_{total} (W) is the total energy in LNG or NG; Φ^{c} (W) and Φ^{fnet} (W) are the thermal convective flux and the net radiative flux in LNG or NG; Φ^{cd}_{ng-lng} (W) is the thermal exchange between LNG and NG at the free surface, $h_{t_{bog}}$ (J·kg^{-1}) is the enthalpy due to condensation, flashing or boil-off gas.

2.2. Heat flux leaking modeling

The total heat flux Φ_{CCS} leaking through the membrane cargo containment systems (CCS) can be written as follow:

$$\Phi_{CCS} = \frac{\lambda_{ccs}(T_i)}{l_{ccs}} \times (T_{h,int} - T_{wall}) \times S_{wall} \quad (5)$$

where λ_{ccs} (W·m^{-1}·°C^{-1}) and l_{ccs} (m) are the equivalent thermal conductivity of CCS and insulation thickness respectively, λ_{ccs} is a function of the thermal conductivity of the material which depends on temperature of each sublayer i. $T_{h,\ int}$ (°C) and T_{wall} (°C) are the temperatures of the inner hull and primary barrier of the CCS respectively, S (m^2) is the exchanged surface.

In fact, $T_{h,int}$ is an average between the temperature of the inner hull at compartment side T_1 (°C) and at CCS side T_2 (°C) (Fig. 2):

$$T_{h,int} = \frac{T_1 + T_2}{2} \quad (6)$$

We consider the thermal budget between T_1 and T_2, the primary barrier temperature T_{wall} (°C) (assumed to be closed to LNG or NG temperature) and T_2, and then by using the conductance K (W·K^{-1}·m^{-2}) we can write:

$$K_1(T_1 - T_2) = K_2(T_2 - T_{wall}) \quad (7)$$

In the same manner as in Eq. (7), we consider the thermal budget

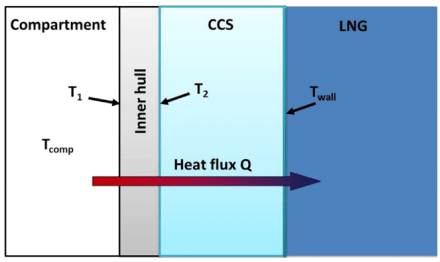

Fig. 2. Schematic representation of the heat transfer through a membrane containment system: Q total heat flux leaking through the insulation; T_{comp} compartment temperature; T_1 inner hull temperature at compartment side; T_2 inner hull temperature at CCS side; T_{wall} primary barrier temperature.

between T_1 and compartment temperature T_{comp} (°C), therefore T_{wall} and T_{comp}, we can express:

$$T_1 = T_{comp} + \frac{(T_{wall} - T_{comp}) \times K_1 \times K_2}{K_1 \times K_2 + K_2 \times K_3 + K_1 \times .K_3} \quad (8)$$

$$T_2 = \frac{K_2 \times T_{wall} + K_1 \times T_1}{K_1 + K_2} \quad (9)$$

with: $K_1 = \frac{\lambda_{steel}}{l_{steel}}$; $K_2 = \frac{\lambda_{CCS}}{l_{ccs}}$; $K_3 = M \times H$

where λ_{steel} ($W{\cdot}m^{-2}{\cdot}°C^{-1}$) and l_{steel} (m) are the thermal conductivity of the inner hull and its thickness respectively, M is a dimensionless coefficient of reinforcement and H is the heat exchange coefficient by convection ($W{\cdot}m^{-2}{\cdot}°C^{-1}$).

For each compartment, the amount of incoming and outgoing energy is equal. By iterating the temperature of adjacent compartments, compartment temperature is expressed as:

$$T_{comp} = \frac{\sum_i^n (U_i S_i T_i)}{\sum_i^n (U_i S_i)} \quad (10)$$

with U_i ($J{\cdot}m^2{\cdot}K^{-1}$) the thermal transmittance of each compartment face i (convection, conduction and radiation), S_i (m^2) the compartment surface, T_i (°C) each compartment's surface temperature.

2.3. Convective heat flux

- **Between the LNG and the primary barrier:**

$$\Phi_{lng}^c = h_{lng} \times S_{lng}(T_{wet\_wall} - T_{lng}) \quad (11)$$

where h_{lng} ($W{\cdot}K^{-1}{\cdot}m^{-2}$) is the convective exchange coefficient between LNG and the wet wall, S_{lng} (m^2) is the wet surface and T_{wet_wall} (K) is the wet wall temperature.

The convective exchange coefficient can be deduced from the Nusselt number and the fluid conductivity. It depends on the slope between the wall and the gravity direction for each part of the tank walls:

$$h_{lng} = \frac{Nu \times \lambda}{L} = C\lambda \left[\frac{g\beta sin\alpha (T_{wet_{wall}} - T_{lng})}{\alpha_{lng} \nu_{lng}} \right]^{\gamma} \quad (12)$$

where L (m) is the wall length, λ ($W{\cdot}m^{-1}{\cdot}°K^{-1}$) is the fluid conductivity, β (K^{-1}) is the thermal expansion coefficient, α (°) is the slant angle, α_{lng} ($m^2{\cdot}S^{-1}$) is the LNG thermal diffusivity and ν_{lng} ($m^2{\cdot}S^{-1}$) is the LNG kinematic viscosity, C and γ are the empirical factors lined to natural convection in turbulent regime.

- **Between the NG and the primary barrier:**

$$\Phi_{ng}^c = h_{ng} \times S_{ng}(T_{dry\_wall} - T_{ng}) \quad (13)$$

where h_{ng} ($W{\cdot}K^{-1}{\cdot}m^{-2}$) is the convective exchange coefficient between NG and the dry wall, S_{ng} (m^2) is the dry surface and T_{dry_wall} (K) is the dry wall temperature. The exchange coefficient h_{ng} can be estimated by using the same method as Eq. (12).

2.4. Conductive heat flux

The thermal stratification is not taking into account in this version. The heat exchange between the LNG and the NG is considered by conduction:

$$\Phi_{ng\rightarrow lng}^{cd} = \frac{\lambda_{lng} S_{ng\rightarrow lng}}{L_{lng}}(T_{ng} - T_{lng}) \quad (14)$$

where λ_{lng}($W{\cdot}K^{-1}{\cdot}m^{-1}$) is LNG conductivity, $S_{ng\rightarrow lng}$ (m^2) is the LNG/NG interface and L_{lng} (m) is the LNG thermal layer.

2.5. Wall temperature

The energy conservation at the primary barrier gives:

$$m_{wall} C_{Pwall} \frac{dT_{wall}}{dt} = \Phi_{CCS} - \Phi_{ng}^c - \Phi_{lng}^c + \Phi_{wall}^{net} \quad (15)$$

where m_{wall} (kg) is the barrier mass, C_{Pwall} ($J{\cdot}kg^{-1}{\cdot}K^{-1}$) is the specific heat capacity of the barrier.

2.6. Equation of state

The modeling of the complex phase behavior of an LNG-NG system requires a suitable thermodynamic model and a robust and efficient computational algorithm for performing phase stability and multiphase flash calculations. Regarding the thermodynamic model, the Peng-Robinson Equation of State has received wide acceptance in the industry because of its ability to predict accurately the phase behavior of liquid-gas systems. To apply this EoS to a mixture, standard Van der Waals one–fluid mixing rules that require the knowledge of binary interaction parameters (k_{ij}) are used. In this work, such interaction parameters were determined using the group contribution method developed for the PPR 78 model [16].

$$P = \frac{RT}{v - b} - \frac{a(T)}{v(v + b) + b(v - b)} \quad (16)$$

and

$$\begin{aligned} R &= 8.314472(J{\cdot}mol^{-1}{\cdot}K^{-1}) \\ b_i &= 0.077796\frac{RT_{ci}}{P_{ci}} \\ a &= \sum_{i=1}^{N}\sum_{j=1}^{N} x_i x_j (a_i a_j)^{0.5}(1 - k_{ij}) \\ a_i &= a_{ci}\alpha_i \\ a_{ci} &= 0.457235\frac{(RT_{ci})^2}{P_{ci}} \\ \alpha_i^{0.5} &= 1 + m_i(1 - T_{ri}^{0.5}) \\ m_i &= 0.37464 + 1.54226\omega_i - 0.26992\omega_i^2 \end{aligned}$$

where P (Pa) is the pressure, R is the gas constant, a and b are the EoS parameters of pure component, v is the molar volume, T_{ci} (K) is the critical temperature, P_{ci} (Pa) is the critical pressure, ω_i is the acentric factor.

2.7. LNG aging modeling

LNG is a mixture of hydrocarbons which contains of 85–95% methane, also containing nitrogen, ethane, propane and other heavier alkanes. Without any additional assumption about pure methane, the mass fraction of each component can be estimated from their mass and temperature evolution over time $(t + dt)$, and the species' conservation equation.

$$x_{lng_i}(t + dt)m_{lng}(t + dt) + x_{bog_i}(t + dt)m_{bog}(t + dt) = x_{lng_i}(t)m_{lng}(t) \quad (17)$$

where x_{lng_i} and x_{bog_i} are the molar fraction in liquid and in BOG respectivly.

The composition of the LNG is changed by the boil-off because the lighter components which have lower boiling points at atmospheric pressure vaporize first. The discharged LNG therefore has a lower percentage content of nitrogen and methane than the LNG that was loaded, and a slightly higher percentage of ethane, propane and butane, due to methane and nitrogen boiling off in preference to the heavier gases. This preferential evaporation not only causes the system to tend toward a new thermodynamic equilibrium state but also causes changes in the thermo-physical properties of the liquid and vapor phases. In order to model this preferential evaporation, a defined volatility coefficient has been elaborated as follow:

$$x_i(t+dt) = \frac{[n_{lng}(t)x_i(t) - \Delta n(t)y_i(t)]}{n_{lng}(t) - \Delta n(t)} \tag{18}$$

where we define the molar mass: $M_{lng}(t+dt) = x_i(t+dt)M_i$
and the molar number: $n_{lng}(t+dt) = n_{lng}(t) - \Delta n(t)$
and the mass: $m_{lng}(t+dt) = n_{lng}(t+dt)M_{lng}(t+dt)$

Once the different physical quantities are calculated, and the volatility can be determined by the thermodynamic model (because it depends on the temperature and the pressure). Therefore we can define the relation between the volatility k_i, the molar number and the molar mass of each species.

$$k_i(t+dt) = y_i(t+dt)/x_i(t) \tag{19}$$

2.8. Boil-off modeling

The LNG is usually transported and stored at a temperature very close to its boiling point at atmospheric pressure which is approximately -160 °C. The LNG evaporation at the free surface is very complex.

A tank filled with LNG composed of multi-component in the thermodynamic state (P_{lng}, T_{lng}) in contact with its vapor in the state (P_{ng}, T_{ng}). Their temperatures, their pressures and their chemical potentials $\mu(P, T)$ being in general different, there is no thermodynamic equilibrium between these two phases.

However, it should be noted that the pressures and temperatures for each of the two phases already implies a form of local equilibrium. That is to say of regularity of the statistical distribution of the particles that make up the fluid. Cases of total imbalance would be related to molecular dynamics and statistical physics.

Then in order to estimate the LNG evaporation rate $\dot{m}_{bog}$ (kg·s^{-1}) at the LNG-NG interface, Collier-Thome model [17] (also named as Hertz Knudsen model) is applied. This model expresses the evaporation of LNG in a biphasic system (liquid-vapor) out of thermodynamic equilibrium as a phenomenon depending on the difference between the saturation pressure which depends on the temperature of the liquid and the pressure of the vapor phase. The saturation pressure in the model is a saturation pressure of the mixture. It is calculated using a thermodynamic model (PR78) which takes into account the temperature and the composition of the mixture (see Eq. (16)).

$$\dot{m}_{bog} = \alpha S_{interface}\sqrt{\frac{M_{lng}}{2\pi R T_{lng}}}\,(P_{sat}(T_{lng}) - P_{ng}) \tag{20}$$

where $S_{interface}$ (m^2) is the LNG-NG interface (or free surface), P_{ng} (Pa) is the NG pressure, P_{sat} (Pa) is the saturation pressure, α is the accommodation coefficient (between 0 and 1). This model is normally used for evaporation estimation in static tank. A constant α is obviously not suitable for different phases of the LNGC voyage. Therefore, a dynamic accommodation coefficient in a linear function of the total heat flux has been introduced: $\alpha = a\hat{A}\cdot\Phi_{CCS} + b$. The values of **a** and **b** are determined from the experience. Moreover, in order to take into account the liquid motion effect on the evaporation, this accommodation coefficient is calibrated from measurement when tank is under sloshing condition.

2.9. Sloshing modeling

The liquid movement inside the tanks (due to waves or navigation) brings mechanical energy to the system. It contributes to the evaporation, but also acts as spraying action and performs as partial cooling down of the gaseous sky.

Cryogenic sloshing problems are mainly studied for space technology but the results of the scientific research in this field apply for LNG ship tanks as well. Thus a model has been proposed by Behruzi and al. [18], providing a basis for this phenomenon. The main difficulty is the estimation of the free surface of the cryogenic liquid: inaccurate thermal gradient can lead to false Boil-off and condensed mass flows. The model used in this paper comes from the condensation model in which the sloshing Nusselt number allows to find the condensation mass flow rate and is expressed as a function of a sloshing Reynolds number.

- **Condensation**

This can occur when the LNG free surface rises provoking the formation of gas pockets likely to condensate. Based on the model proposed by Behruzi and al. [18], a limited layer of the liquid bulk is likely to be condensate according to the vessel's movements. The condensation flow rate $\dot{m}_{cond}$ (kg·s^{-1}) can be written as follows:

$$\dot{m}_{cond} = \frac{\lambda_{lng} S_{ng\to lng}}{L_v \delta}(T_{sat} - T_{ng}) \tag{21}$$

$$\delta = \frac{L}{N_u}$$

$$N_u = A(RePr)^B$$

$$Re = \rho_{lng}\frac{u_m L}{\mu}$$

$$u_m = \frac{l_{tank}}{2}\tan(\varnothing_{tilting})\omega_{sloshing}$$

where δ(m) is the condensate layer, L (m) is the characteristic length, N_u is the Nusselt number, Re is the Reynolds number, Pr is the Prandtl number, u_m (m·s^{-1}) is the wave propagation speed, l_{tank} (m) is the tank width $\varnothing_{tilting}$ (°) is the angle of inclination of the ship compared to its static position, $\omega_{sloshing}$ (s^{-1}) is the waves' frequency.

The condensation phenomenon is linked to the all movements of the LNG carrier. At this stage, only rolling is considered in the model.

- **Flashing**

The flashing phenomenon modeling is similar as the condensation model with some adaptation. When the cold liquid touches on the hot dry wall, a sudden forced convection is created. The flashing flow rate $\dot{m}_{flash}$ (kg·s^{-1}) can be written as follows:

$$\dot{m}_{flash} = \frac{h_{flash} S_{dry\_wall}}{L_v}(T_{dry\_wall} - T_{lng}) \tag{22}$$

where h_{flash} (W·K^{-1}·m^{-2}) is the convective exchange coefficient between the dry wall and the liquid $h_{flash} = \frac{Nu_{flash}\cdot\lambda_{lng}}{L}$.

3. Validations

Some key results will be presented in the two following sections. In order to validate our model as completely as possible with a large available dataset in real LNG carrier environment, we choose the dataset from an onboard collection platform. This type of the collection platform has been installed onboard several LNG carriers. A series of measurements has been made since 2014. The results of this data collection can help determine vessel efficiency, which, in turn, assist operators in maximizing ship efficiency and operations.

The recorded amount of NG leaving from tanks is imposed as boundary condition in the simulations. However, the recorded value is only available for all tanks not for individual tank. Therefore, an assumption has been made to distribute this amount to each tank. This assumption introduces the error that accumulates during the simulation. For this reason, the simulation is performed with a period of 72 h.

3.1. Numerical sensitivity

Before starting the simulations, a numerical sensitivity has been performed. The evolution of temperatures in tanks and of pressure with different time-step has been tested (e.g., 1, 30, 60, 300 s). Finally, using 30 s is a good compromise between precision and computation time. The numerical scheme allows the use of a larger time-step for the total heat flux Φ_{CCS} leaking through the CCS and the LNG aging. Several time-steps have been tested: 1, 5, 15 and 30 min for a diurnal cycle simulation. The resulting difference between a time-step of 1 min and 5 min is small, being less than 0.3%. So 5-min was considered as an optimum time-step for the total heat flux and the LNG aging calculations.

The initial LNG compositions are usually provided by the terminals. Their thermodynamic properties were taken from the REFPROP (an acronym for REFerence fluid PROPerties). This program, developed by the National Institute of Standards and Technology (NIST), calculates the thermodynamic and transport properties of industrially important fluids and their mixtures.

3.2. Simulation of voyages

In the example shown here, the modeled LNG carrier has a capacity of about 160,000 m^3. The LNG temperature is measured by sensors placed at different heights in the tank. These sensors are typically platinum resistance thermometers close to the scaffold, normally five per tank of the cargo. One sensor is always in the liquid phase at the bottom of the tank and another is always in the vapor phase at the top of the tank. These sensors are tested and calibrated at regular intervals. The accuracy varies between 0.1 and 0.2 °C for a temperature between −165 and −145° C.

Figs. 3–6 show the simulation results with the observation including temperatures and pressures in a tank for the navigation phase of a ballast and of a laden voyage.

Overall, the evolutions of the LNG temperatures are correctly simulated (blue lines in Figs. 3 and 5). The temperature can vary with a difference between the liquid and the vapor up to 50 °C. It is difficult to model the gas phase. The differences between the measurement and the simulation (red lines in Figs. 3 and 5) can be explained by the fact that in the tank, the gas temperature is not uniform everywhere and very local variations may occur. However, we assumed a 0D model with an average liquid temperature and an average vapor temperature. Therefore, the variation of the mean NG temperature is better simulated in ballast voyage (red lines in Figs. 3 and 5) because the NG behavior during the ballast voyage is more stable than the one during the laden voyage.

During a voyage the tank pressure is under control and its variation is in a small range. The modeled pressure (full lines in Figs. 4 and 6) displays a good agreement with observation. For the same reason above, the pressure is better simulated in ballast voyage (Fig. 4).

4. Application examples

4.1. Operational Boil-Off

When the operating conditions are imposed as boundary conditions, we can estimate the Boil-off Gas in the real LNG carrier's environment. Fig. 7 gives an overview of this type of calculation procedure. The framework is generic and applicable for different scenarios.

A 24-day's laden voyage is shown here to illustrate this calculation feature.

Table 1 gives the initial LNG composition. To be consistent with the experiment, the LNG temperature is initialized at −159.2 °C in the simulation.

The inputs about navigation conditions are determined from measurements, using the variation of the ship speed and the tank pressure profiles (Fig. 8). The operational Boil-Off Rate is defined as the percentage of the evaporated LNG mass per day with respect to the tank capacity. Moreover, we consider that BOG is the LNG loss amount; natural BOG is the amount of LNG evaporated at the top of the tanks; forced BOG is the LNG extracted from down in the tanks and evaporated, BOG to GCU is the gas released to the Gas Combustion Units.

Unlike the Design BOR, the operational Boil-Off corresponds to the part of the heat ingress that actually leads to the evaporation of LNG, while another part is used to heat the cargo and the CCS. In addition, by taking into account the sea conditions, a part of the evaporation is due to the agitation of the liquid in tanks.

There is no data from the vessels about the LNG and the NG compositions during the voyages, only the composition in the export and import terminals. It is only possible to analyze roughly the composition evolution for laden voyages since the element proportions inside the LNG at the end of a ballast voyage are not recorded. First of all, the model used gives slightly different results for each tank. Because of the lack of real composition data inside each tank, this behavior cannot be really gone further into. On the other hand, the expected composition trend can be observed i.e.: for the lighter elements (CH_4 and N_2), a proportion decrease in the LNG phase and an increase in the BOG composition and the opposite for the heavier elements. One can observe small gaps between the simulated LNG proportions and the terminals' data (Table 2) but it is not enough to assess the impact of those differences (Table 3)

Fig. 9 shows the evolution of measured and modeled BOG due to various LNG extractions in transportation. Even though some local variations are not captured, the temporal evolution of the natural BOG (black lines), forced BOG (red lines) and BOG to GCU (blue lines) are correctly reproduced by our 0D model. From the results, we observe a significant high value of BOG to GCU (blue lines). In fact, this value of BOG to GCU could be reduced by an optimal pressure management. For example, we can adopt a strategy for the tank pressure management when ship speed was low (Fig. 8).

In order to clarify and quantitatively analyze the performance of the model, we have tabulated the results at the end of the voyage. From Table 2, we observe a small difference (about 1%) in the value of total BOG between measurement and simulation. During this voyage, the operational BOR related to the LNG lost volume is 0.14% per day. The value of the operational BOR obviously depends on the operational conditions in which the ship operated during the trip. Different operational conditions or composition of LNG with a different initial

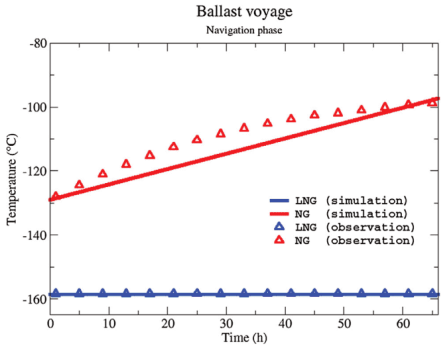

Fig. 3. Evolution of LNG (blue) and NG (red) temperatures during a ballast voyage (triangle symbol: Measurements; full line: Simulations). (For interpretation of the references to colour in this figure legend, the reader is referred to the web version of this article.)

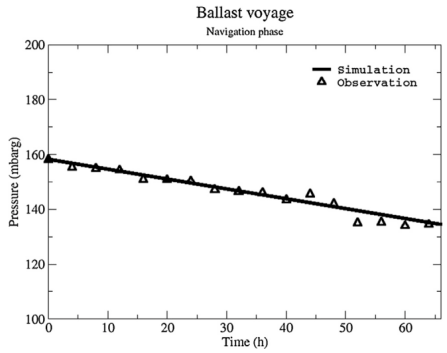

Fig. 4. Evolution of tank gauge pressure during a ballast voyage (triangle symbol: Measurements; full line: Simulation).

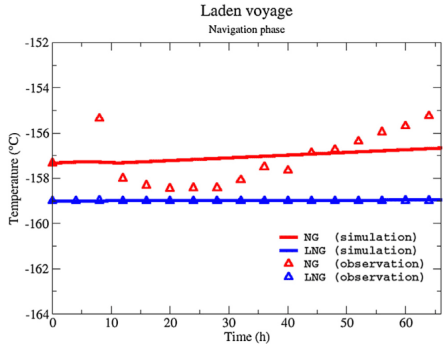

Fig. 5. Same as Fig. 3 but for a laden voyage.

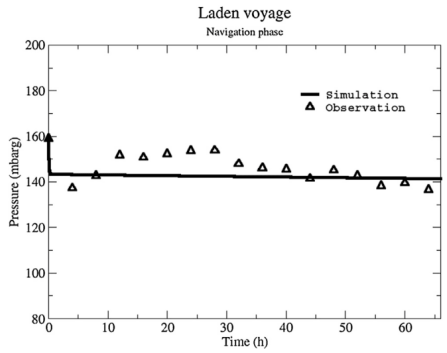

Fig. 6. Same as Fig. 4 but for a laden voyage.

temperature than those simulated in this case would give a different result from this case.

Another application of this type of the simulations is to support the LNG ship design or specification [19]. This kind of simulation can guide ship-owner to choose the best CCS technology according to the type of trade that the ship will perform. It can also help the research and development of new CCS.

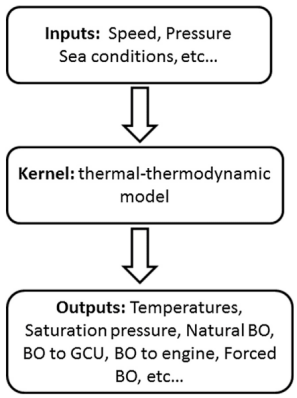

Fig. 7. Overview of the Operational Boil-Off simulation procedure.

Table 1
LNG composition at departure for a laden voyage.

Composition	CH_4	C_2H_6	N_2	C_3H_8	C_4H_{10}
(%)	93.29	5.73	0.03	0.83	0.11

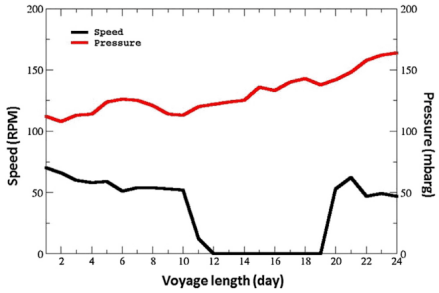

Fig. 8. Datasets about the operating profile for a laden voyage: Ship speed (RPM) and Tank pressure (mbarg).

Table 2
LNG weathering predictions and arrival terminal data.

Composition (%)	Measured	Predicted
CH_4	92.68	[92.90; 93.00]
C_2H_6	6.35	[6.14; 6.17]
N_2	0.01	0.01

4.2. Self-pressurization

Self-pressurization phenomenon is one of the most important problems in the storage of cryogenic liquid. It has been difficult to predict

Table 3
Comparison of the BOG study in the end of the voyage.

	Measured		Simulated	
	Total (natural + forced)	Natural	Total (natural + forced)	Natural
Total BOG (ton)	2236	2225	2259	2258
Total LNG lost volume (m^3)	5036	5011	5087	5085
Lost volume rate (m^3/day)	219	217	221	221
Operational BOR (%/day)	0.14	0.14	0.143	0.143

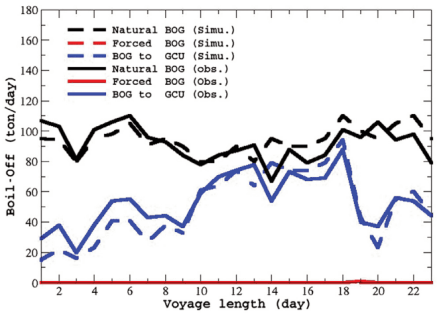

Fig. 9. Comparison of the BOG study with voyage length of 24 days: full lines: observation; dashed lines: simulation.

exact pressurization process due to its complex non-equilibrium thermal behavior.

The study shown here is a part of a project which aims to understand the behavior of a Floating LNG Regasification Unit (FSRU). This FSRU is equipped with a GTT insulation system. It receives the gas from other LNG carriers through ship-to-ship operations. Then it re-gasifies the LNG with a heater and sends it to the network on the ground. When the tank is disconnected from the terminal and the ship needs send out the gas in emergency situations, an emergency system is started off in order to absorb the evaporating gas and maintain the maximum pressure in the tank. The challenge here is to estimate the duration of the self-pressurization to a certain limit.

Fig. 10 depicts the comparison between the time evolution of calculated pressure and observation. The simulation started when the experimental boundary condition became steady, the tank was closed and started self-pressurizing. The exact value is normalized for confidentiality: normalized time $t_N = t/C_1$ and normalized pressure $P_N = P/C_2$, where C_1 and C_2 are two defined constants. As shown in the figure, the modeled pressure compares well to the measurements. To complete the discussion, Fig. 11 illustrates the comparison between the time evolution of calculated temperatures and observation. The variation of the normalized pressure seems more important than in the temperature because the used pressure is the relative pressure in mbarg. If we use the absolute pressure, the pressure change is only about 30% which is coherent with the temperature change. The NG temperature exhibits underestimation. Nevertheless, the modeled temperatures display a good agreement with observation.

During the whole pressurization period, there are two origins of steep pressurization curve (Fig. 10). One is the large evaporation at the interface in initial period (normalized time from 0 to 0.4). Although the tank is closed and pressure increases, the temperature of a large amount of liquid mass is still maintained as saturation temperature in the beginning of self-pressurization. Hence, relatively larger evaporation occurs than latter constant pressurization period having subcooled liquid and it makes the steep increase of pressurization in initial period.

5. Conclusion and perspectives

We have described the physical model implemented in a detailed 0D tool thermal and thermodynamic to meet the requirements of the LNG carrier industrial target applications. Hence, specific effort has also been devoted to implement satisfactory schemes to compute Boil-off Gas in real navigation conditions.

Validations of the full thermal-thermodynamic model were performed through a comparison with onboard observation datasets. The model successfully simulated the liquid and the gas temperatures evolution and the variation of pressure within the ballast and laden voyages for a period up to 3 days.

The rigorous modeling of the LNG evaporation phenomenon can make a significant contribution to industry and science. As a demonstration of the ability of the model, the operational Boil-Off has been also investigated by integrating the actual sailing conditions, the thermal inertia of the CCS, sea conditions and unsteady evolution of LNG and NG. During a laden voyage profile of a case study LNG carrier, we have evaluated the model with onboard experiment including the comparison with the measured natural BOG, forced BOG data and BOG to GCU. The result shows the importance of taking into account operating profile in pressure and in engine consumption to represent the variability of the BOG under real onboard conditions. Overall the agreement between measurements and model simulations is fair. With a given voyage profile, we can perform simulations to choose the best technology for the insulation. The self-pressurization study shows this tool is also suited to predict the pressurization rate in a certain range. It can contribute to applications in the field of dimensioning system.

Model results are encouraging and give insight into the BOG optimization, but further and more rigorous testing have to be performed.

Since 2014, the code is being used for industrial applications and research activities in several fields related to Boil-off. The requirement for improving robustness and precision of numerical schemes becomes all the more apparent as the complexity of physical modeling increases.

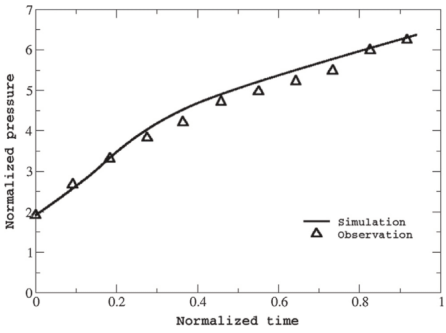

Fig. 10. Evolution of gauge pressure for the self-pressurization study: triangle symbol: observation; full line: simulation.

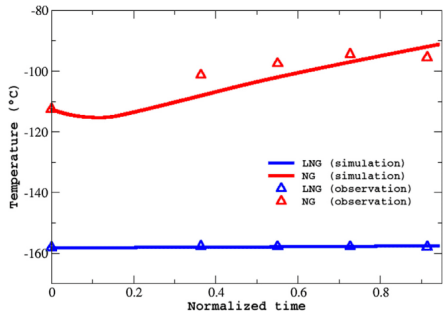

Fig. 11. Evolution of LNG (blue) and NG (red) temperatures for the self-pressurization study: triangle symbol: Measurements; full line: Simulations. (For interpretation of the references to colour in this figure legend, the reader is referred to the web version of this article.)

Apart from fundamental work on robustness and precision (for example for boundary layer at the free surface), future developments will focus on 1D even CFD modeling, especially for the thermal stratification in the tank. Nevertheless, LNG aging will receive further attention. Model and code coupling are also domains of interest that will require attention (LNG carrier global efficacy).

Eventually, the use of this tool as specific-purpose thermal-thermodynamic code for production and as a development platform will be further extended to a community of industrial partners and universities determined to participate in R&D work on numerical schemes and physical modeling.

To supplement the panorama, it is pointed out that for historical reasons the domain of application addressed by this code is essentially limited to LNG, with extension to other cryogenic liquids. Moreover, the structure of this code and the key features of the algorithm have been used as a starting point for embedded software. The later has since then benefited from a sustained development effort. The code also contributes to the research work carried out at the Ariane Group on LNG, with or without tank motions.

Acknowledgements

The authors would like to underline that this paper is based on the work of many other contributors, from developer to end user, to whom they are most grateful, and especially: Pascal Ta, Benjamin Cuniasse, and Didier Hebert.

The authors also wish to express their sincere gratitude to François Hanat, Vincent Berger, Sébastien Duquesnoy, Guillaume Leclere, Julien Burdeau, Emmanuel Rousseau, Antoine Marès, Fabrice Lombard, Laurent Spittael, Laurent Brosset, Laurent Sorlin, Jean-Michel Rovarch, Hélène Loncin, Didier Bouchain, Pablo Gavin, and Gerald Galan for their pertinent advice.

Eventually, the authors would like to point out that this work has been possible thanks to GTT strategic choices and R&D funding for developing software and expertise on numerical methods.

Appendix A. Supplementary material

Supplementary data to this article can be found online at https://doi.org/10.1016/j.cryogenics.2018.09.002.

References

[1] Sharafian A, Herrera OE, Mérida W. Performance analysis of liquefied natural gas storage tanks in refueling stations. J Natl Gas Sci Eng 2016;36:496–509. https://doi.org/10.1016/j.jngse.2016.10.062.

[2] Aspen Plus dynamics user guide (Version 8.8); 2016. < http://www.aspentech.com/ > .

[3] Hasan MMF, Zheng AM, Karimi IA. Minimizing boil-off losses in liquefied natural gas transportation. Ind Eng Chem Res 2009;48:9571–80. https://doi.org/10.1021/ie801975q.

[4] Yan G, Gu Y. Effect of parameters on performance of LNG-FPSO offloading system in offshore associated gas fields. Appl Energy 2010;87:3393–400. https://doi.org/10.1016/j.apenergy.2010.04.032.

[5] Querol E, Gonzalez-Regueral B, García-Torrent J, García-Martínez MJ. Boil off gas (BOG) management in Spanish liquid natural gas (LNG) terminals. Appl Energy 2010;87:3384–92. https://doi.org/10.1016/j.apenergy.2010.04.021.

[6] Park C, Song K, Lee S, Lim Y, Han C. Retrofit design of a boil-off gas handling process in liquefied natural gas receiving terminals. Energy 2012;44:69–78. https://doi.org/10.1016/j.energy.2012.02.053.

[7] Fahmy MFM, Nabih HI, El-Rasoul TA. Optimization and comparative analysis of LNG regasification processes. Energy 2015;91:371–85. https://doi.org/10.1016/j.energy.2015.08.035.

[8] Chen QS, Wegrzyn J, Prasad V. Analysis of temperature and pressure changes in liquefied natural gas (LNG) cryogenic tanks. Cryog Guildf 2004;44:701–9. https://doi.org/10.1016/j.cryogenics.2004.03.020.

[9] Pellegrini LA, Moioli S, Brignoli F, Bellini C. LNG technology: the weathering in above-ground storage tanks. Ind Eng Chem Res 2014;53:3931e3937. https://doi.org/10.1021/ie404128d.

[10] Migliore C, Tubilleja C, Vesovic V. Weathering prediction model for stored liquefied natural gas (LNG). J Natl Gas Sci Eng 2015;26:570–80. https://doi.org/10.1016/j.jngse.2015.06.056.

[11] Migliore C, Salehi A, Vesovic V. A non-equilibrium approach to modelling the weathering of stored Liquefied Natural Gas (LNG). Energy 2017;124:684–92. https://doi.org/10.1016/j.energy.2017.02.068.

[12] Tanudjaja R, Lanquetin B. 1990: high flexibility and effective voyage cost improvement for LNG carrier 'Ekaputra' due to low boil-off rate. Presented at the 14th international LNG/LPG conference and exhibition – GASTECH 90, Amsterdam, Netherlands, December 4–7, 1990. 1990.

[13] Ait Ferhat S, Benbrik A, Lemonnier D. Thermal study by a nodal model of the unit tank-LNG in interaction with environment. Presented at the 7th world congress of chemical engineering, Glasgow, Scotland, July 10–14, 2005. 2005.

[14] Miana M, Legorburo R, Diez D, Hwang YH. Calculation of boil-off rate of liquefied natural gas in mark III tanks of ship carriers by numerical analysis. Appl Therm Eng 2016;93:279–96.

[15] Dimopoulos GG, Frangopoulos CA. A dynamic model for liquefied natural gas evaporation during marine transportation. Int J of Thermodyn 2008;11:123–31.

[16] Qian J, Privat R, Jaubert J-N. Predicting the phase equilibria, critical phenomena and mixing enthalpies of binary aqueous systems containing alkanes, cycloalkanes, aromatics, alkenes and gases (N_2, CO_2, H_2S, H_2) with the PPR78 equation of state. Ind Eng Chem Res 2013;52:16457–90.

[17] Collier JG, Thome JR. Convective boiling and condensation. Oxford Science Publications; 1999.

[18] Behruzi P, Konopka M, de Rose F, Schwartz G. Cryogenic slosh modeling in LNG ship tanks and spacecrafts. Presented at the 24th (2014) international ocean and polar engineering conference, Busan, Korea, June 15–20, 2014. 2014.

[19] Qu Y, Noba I, Cuniasse B. A simulation model for specifying optimal LNG carrier cargo containment systems based on operational simulations. Presented at the 32st international scientific & expert meeting of gas professionals, Opatija, Croatia, May 3–5, 2017. 2017.

3.3.2. Calibration automatique

Afin de s'assurer de la cohérence et la représentativité des modèles physiques théoriques avec la réalité, une calibration automatique des modèles a dû être mise en œuvre afin de combler l'écart entre la théorie et l'observation. Ce processus permet d'utiliser les modèles et le moteur de simulation sur un très grand nombre d'essais ou voyages afin de venir minimiser l'erreur globale de modélisation du Boil-Off Naturel.

Le livrable de sorti est un outil permettant d'automatiser les processus de calibration afin de sortir un jeu de coefficient de calibration par navire et type de propulsion. Cet outil a été co-développé entre GTT et une société française en ingénierie. J'étais interlocuteur GTT pour le pilotage du projet notamment les aspects techniques. Cet outil peut être utilisé par n'importe quel ingénieur impliqué sur les projets de simulation de Boil-off à GTT.

3.4. CONCLUSION

Le présent chapitre a été divisé en 3 parties :

- dans une première partie, j'introduis le problématique du Boil-off à étudier dans le secteur du transport du GNL maritime.
- dans seconde partie, l'état de l'art initial présente les limites fondamentales des approches dans la littérature vis-à-vis surtout de la problématique du Boil-off en opération.
- dans la dernière partie, je présente des travaux réalisés depuis mon arrivé chez GTT au tour de ce sujet avec un article pour résumer les résultats principales.

Le chiffre d'affaires d'une société comme GTT provient principalement de son expertise. La communication vers l'extérieur sur son savoir-faire est extrêmement restreinte, ce qui constitue une difficulté non négligeable pour faire une publication scientifique. Je souligne donc l'effort d'avoir publié un tel article grâce à la coopération université-entreprises.

4.
MESURE DE PROPRIÉTÉS THERMODYNAMIQUES DU GNL

4.1. PROBLEMATIQUE ET OBJECTIFS

La partie expérimentale consistait à collecter des données à bord d'un méthanier à partir de plus de 300 instruments de mesure. Il s'agissait également d'observer et de comparer les pratiques opérationnelles à bord en vue d'identifier et de partager les meilleures pratiques et d'effectuer quelques tests pour voir la réponse du méthanier et de sa cargaison.

La campagne de mesure et de collecte de données a permis d'obtenir des informations sur le comportement réel d'un méthanier en opération, nécessaire et indispensable à la compréhension des phénomènes physiques complexes qui prennent place dans la cuve. Mon rôle a consisté à encadrer l'équipe à bord pour l'analyse de données puis de confronter celles-ci au modèle implémenté.

Pour mieux comprendre / quantifier l'impact du flux de chaleur et du mouvement du liquide sur le taux de BOG, une série d'essais cryogéniques avec du méthane liquide pur et un mélange défini méthane/éthane ou méthane/azote avec différents flux de chaleur entrants a été réalisée avec notre partenariat Ariane Group. Les tests réalisés ont été à la fois des tests en en Boil-Off et des tests de montée en pression. En tant qu'interlocuteur principal de GTT, ma mission a été d'assurer le bon déroulement des essais et d'améliorer notre modèle physique issu des essais.

4.2. MOYENS EXPERIMENTAUX

4.2.1. Collecte de donnée au bord

Le 1er moyen réside en missions expérimentales sur le méthanier pilote (Fig.7).

- Réalisation de 4 missions d'observation, de tests et de mesure de 3 semaines chacune.
- Analyse de la réaction de la cuve et de la cargaison dans diverses situations opérationnelles afin d'identifier les modes opératoires les plus efficaces.

- Réalisation de 2 missions supplémentaires visant à caractériser les premières observations sur un autre méthanier, puis à mettre en place ces modes opératoires optimisés et, le cas échéant, à affiner les premières analyses et les premières conclusions.
- Mise en place de nouvelles pratiques concernant la gestion de la pression des cuves, celle des opérations de spraying et de forcing vaporisation et de chargement du navire.
- Réalisation de tests préliminaires et d'études théoriques afin d'améliorer le fonctionnement de la chaîne gaz.
- Analyse de l'influence de l'assiette du navire, de la température du ciel gazeux et de celle du GNL sur la performance énergétique du méthanier.
- Réalisation de tests et optimisation du fonctionnement de la chaîne gaz.
- Réalisation d'une nouvelle mission à bord d'un autre méthanier pour comparer les observations.

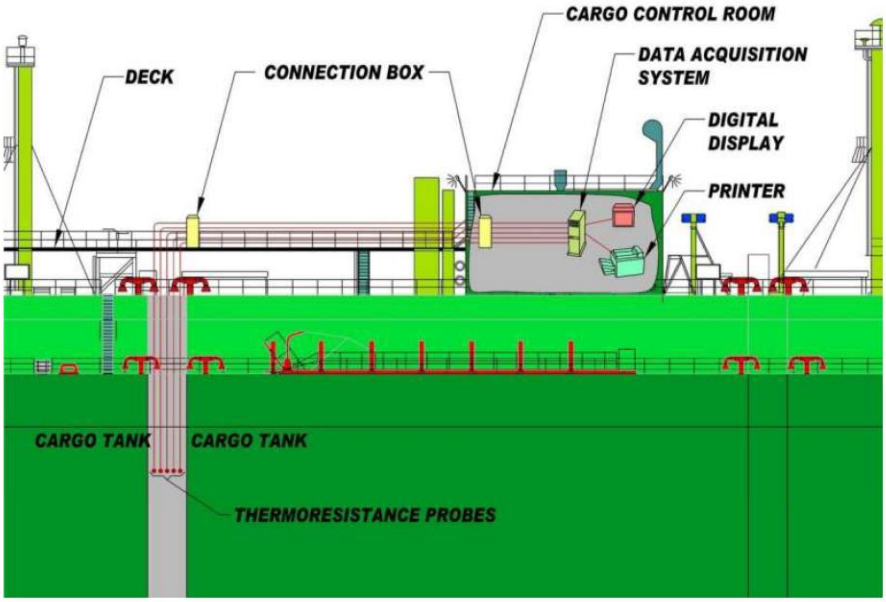

Fig7. Schéma du dispositif de mesure de température sur un méthanier

4.2.2. Essai au laboratoire

Le 2ème moyen expérimental est réalisé par notre partenariat Ariane Group Group (ancien Airbus Safran Lanchers) avec des tests de Boil-off et de montée en pression de liquides cryogéniques à l'intérieur d'une cuve cylindrique de petite taille (de type dewar) dans un environnement statique. En 2016, avec Ariane Group nous avons réalisé les essais EMCTS (pour Ethane Methane

Cylindrical Tank Static) consistent en une série de 24 essais cryogéniques avec du méthane liquide pur et avec un mélange défini méthane/éthane avec différents flux de chaleur entrants. La première moitié sont des tests en boil-off et la seconde, des tests de montée en pression.

Il est possible de contrôler approximativement l'intensité du flux thermique entrant en ajustant le niveau de vide du Dewar. Une batterie de thermocouples et de diodes permet de relever la température en différent points du système.

Tous les essais menés comprenaient une phase, où le système était en condition de Boil-off ouvert et les gaz d'échappement circulaient librement hors du système. A l'issue de ces essais, une étape d'analyse a permis de :

- Calculer la température absolue mesurée par les thermocouples.
- Définir la chaleur parasite.
- Définir la température près de la surface libre.

Le deuxième groupe de tests comprenait une phase d'auto-pressurisation. Au cours de cette phase, le système a été fermé et le développement de la pression observé a été lié à la chaleur parasite.

Après les expériences menées lors de la 1ère campagne d'essais, des capteurs supplémentaires ont été ajoutés et la procédure de test améliorée. En outre, l'ajout d'azote au mélange a modifié significativement la thermodynamique par rapport la 1ère expérience réalisée. La 2ème phase de ces essais, LCTS (pour LNG cylindrical tank static test with LNG like test liquids a été démarré en 2017. Cette série d'essais est pour prendre en compte l'effet de l'azote dans les phénomènes de Boil-off et de pressure rise.

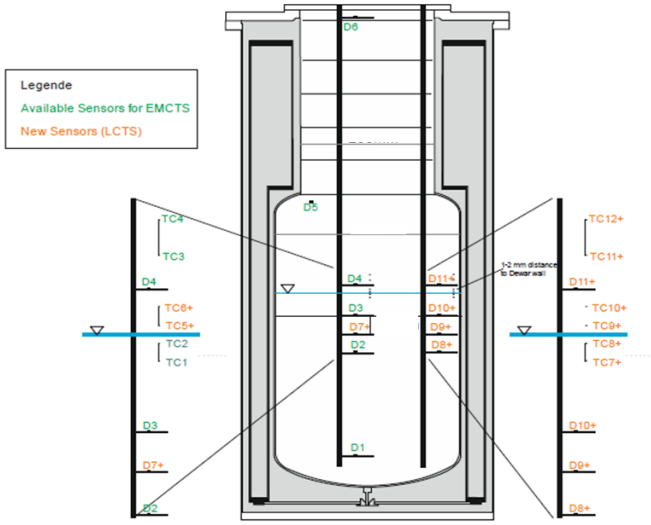

Fig8. Nouvel emplacement de capteurs de température

Par rapport à la 1ère série d'essais, des capteurs supplémentaires sont mis en place (Fig.8). Il y a 11 diodes placées dans le réservoir, une à la sortie des gaz, 2 près de la surface libre dans le centre de Dewar et 2 près de la paroi de Dewar. Cinq diodes sont placées dans le liquide et une à proximité du couvercle du Dewar. Huit thermocouples (TC) sont placés près de la surface libre pour la détermination du gradient de température à la surface libre et quatre thermocouples sont placés dans la phase gazeuse le gradient de température dans le gaz. Les TCs mesurent seulement une différence de température par rapport aux diodes en tant que valeur de tension.

Un stage de fin d'étude que j'ai encadré a été financé pour prototyper un modèle 1D pour modéliser la stratification thermique dans le liquide et de ce fait, aboutir à une meilleure estimation du taux d'évaporation. Au terme de ce stage, un modèle couplant les phénomènes de transfert thermique, de thermodynamique et de mécanique des fluides simplifiée a été développé à partir d'un modèle existant qui a été amélioré et adapté de façon à convenir aux différentes conditions et propriétés relatives au GNL plus GN.

Ces améliorations comportent notamment son adaptation aux échelles réduites en passant du pseudo 2D vers le 1D, la prise en compte de transferts thermiques entre couches avec des échanges conductifs pour le liquide et convectifs pour le gaz et la mise en œuvre d'une condition sur les échanges massiques entre ces dernières (autrement dit les mouvements de quantité de matière au sein d'une même phase).

Les essais EMCTS et LCTS effectués expérimentalement par Ariane Group ont permis de le mettre à l'épreuve et de le valider sur les résultats en températures malgré les difficultés rencontrées concernant les conditions aux limites (flux thermique infiltré vers la cuve). Ces essais ont mis en évidence que la montée en pression s'accompagne toujours de l'établissement d'une couche thermique sous la surface libre entre la température du bulk qui reste homogène et croit lentement et la température de saturation à la surface libre qui croit aussi avec la pression. L'épaisseur de cette couche croit progressivement avec la pression dans la cuve. Le gradient de température à tout instant dans cette couche s'accompagne d'un gradient de densité du liquide.

Ainsi, on peut dorénavant simuler la stratification thermique ayant lieu lors du stockage du GNL de façon satisfaisante et ce pour les différentes conditions aux limites que peut rencontrer une cuve réelle. Deux versions de ce modèle ont été développées, la version zonal 2D initiale pouvant servir dans le cas d'échelles réelles avec des épaisseurs de couche limites plus importantes et une moindre influence du flux thermique latérale sur la partie centrale de chaque phase et la version 1D servira pour de prochains essai sur la cuve d'Ariane Group ou autres cas de petits réservoirs.

La simulation du domaine dans sa globalité avec comme seule donnée d'entrée le flux thermique latéral et à moindre mesure la température de la diode en haut du Dewar pour estimer le flux infiltré par la partie supérieure, a permis de tester et d'approuver la validité du modèle de Hertz-Knudsen pour quantifier le taux d'évaporation avec une corrélation interne à GTT pour l'estimation du coefficient d'accommodation.

À l'issue des différentes simulations, on aboutit aux constats suivants concernant la phase liquide pour les différentes conditions :

Faibles pressions dans le gaz (Condition de cuve ouverte) :

- Forts taux d'évaporation ;
- Accentuation des mouvements convectifs et des transferts de masse au sein du liquide ;
- Dépendance accrue aux variations spatiales et temporelles du flux thermique infiltré ;
- Faibles échanges thermiques entre gaz et liquide à l'interface.

Fortes pressions dans le gaz (Condition de cuve fermée) :

- Faibles taux d'évaporation ;
- Réduction des mouvements de convection massique ;
- Échanges de chaleur considérables du gaz vers le liquide.

Enfin, l'augmentation du niveau du liquide constaté dans les essais expérimentaux peut avoir comme origine deux phénomènes différents, le premier étant la dilatation importante du liquide due à l'augmentation de sa température, et le deuxième est l'apparition de condensation du gaz à proximité des parois latérales.

4.3. CONCLUSION

Le travail présenté dans ce chapitre résume les campagnes d'essais menés par Ariane Group. Les expériences sont source de données essentielles pour mieux comprendre les phénomènes de Boil-off, de montées en pression et du vieillissement du GNL et contribuent à l'amélioration des modèles de la plateforme multi-physique développée par GTT.

L'analyse des données des tests en Boil-off a permis d'exprimer l'épineux coefficient α du modèle d'évaporation de Hertz-Knudsen. L'application d'une telle relation sur un cas réel donne des résultats tout à fait prometteurs et mérite une étude plus approfondie. L'analyse des montées en pression a avant tout mis en avant que la stratification thermique des parties liquide et gazeuse revêtant un caractère essentiel de cette configuration. Le caractère 0-D des modèles utilisés dans notre plateforme est insuffisant et il est nécessaire d'utiliser une modélisation 1-D voire 3D. Cette étude fait par ailleurs l'objet d'un stage que j'ai encadré en 2017 puis d'une thèse CIFRE depuis 2018.

5.
CONCLUSION GÉNÉRALE

Par ce manuscrit, j'ai tenté de décrire avec concision les différentes activités de recherche que j'ai menées pendant les 12 années qui se sont écoulées depuis ma thèse. Mes principaux thèmes de recherche ont été évoqués dans trois chapitres distincts que j'ai conclus par la présentation détaillée de mes perspectives de recherche à court et moyen terme.

Dès le début de ma carrière, j'ai su saisir l'opportunité de développer mes connaissances dans le secteur de l'énergie, traçant pour chaque problème une cartographie de résolution oscillant entre des choix robustes impliquant des méthodes éprouvées et des paris plus risqués permettant de faire progresser les connaissances dans ce domaine.

L'enjeu est donc récurrent : conjuguer précision et faisabilité, obtenir des résultats tangibles tout en restant créatif et original. Mes travaux de recherche se complètent par une activité de publication, s'appuient sur des contrats et des collaborations avec des universités nationales et internationales ainsi qu'avec des entreprises.

Ces années, passées chez EDF et chez GTT, m'ont permis d'asseoir mes connaissances et de mener diverses recherches dans le domaine de l'optimisation énergétique des procédés. Aujourd'hui, de nouvelles perspectives très prometteuses s'ouvrent au GNL en tant que carburant marin, qui vont bien au-delà des seuls méthaniers. Pour pénétrer ce nouveau marché, GTT est à la recherche de solutions innovantes et lance de multiples sujets de R&D. Certains de ces sujets vont s'inscrire dans la durée et induire le financement de thèses. Il est donc fortement souhaitable qu'un collaborateur de GTT soit titulaire d'un diplôme d'HdR afin de pouvoir assurer le co-encadrement officiel du thésard. Ma 1ère priorité va être de répondre aux exigences des industriels qui souhaitent commercialiser les savoir-faire existants et en créer de nouveaux.

En outre, en tant que vacataire à l'Université Paris-Saclay, j'envisage de me présenter à moyen terme sur un poste de PAST rattaché au laboratoire de Mécanique et d'Energétique. Je viendrai ainsi renforcer l'équipe "Fluide Environnement Identification" (FEI) sur des sujets relatifs à la modélisation dynamique multi-échelle de la pollution atmosphérique en milieu urbain. Ce sont des sujets de recherche sur lesquels j'avais travaillé lors de la préparation de ma thèse et en post-doc. De surcroît, l'université Paris-Saclay et le Chinese Scholarship Council (CSC) ont conclu un accord qui prévoit le financement par le gouvernement chinois de 40 thèses par an, pendant 4 ans. Les doctorants ainsi financés effectueront leur thèse dans une École Doctorale de Paris-Saclay. Tous

les champs disciplinaires, et donc toutes les écoles doctorales sont éligibles. Etant d'origine Chinoise, je me suis engagé avec grand plaisir à jouer le rôle d'ambassadeur dans cet immense programme bilatéral. A ce jour, le 1er sujet de thèse avec l'équipe FEI s'inscrit dans le cadre de cette collaboration a été rédigé et diffusé. L'HdR devrait alors me permettre de discuter plus facilement avec les professeurs chinois et les autres collègues français. L'obtention de ce diplôme devrait grandement favoriser les échanges.

6.
RÉFÉRENCES

[1] Archambeau F., Mechitoua N., Sakiz M. Code_Saturne: a Finite Volume Code for the Computation of Turbulent Incompressible Flows Industrial Applications - Int. J. on Finite Volumes, 2003 : 1, 1-62.

[2] Dimopoulos, G.G., C.A. Frangopoulos, 2008: A Dynamic Model for Liquefied Natural Gas Evaporation During Marine Transportation, Int. J. of Thermodynamics, 11, 123-131

[3] Hasan, M.M.F., Zheng, A.M., Karimi, I.a., 2009. Minimizing boil-off losses in liquefied natural gas transportation. Ind. Eng. Chem. Res. 48, 9571-9580. http://dx.doi.org/10.1021/ie801975q.

[4] Masson V., et al., The Canopy and Aerosol Particles Interactions in TOulouse Urban Layer (CAPITOUL) experiment. - Meteor. Atmos. Phys., 2008: 102 (3-4), 135-157

[5] Miana, M., R. Legorburo, D. Diez, Y.H. Hwang, 2016: Calculation of Boil-Off Rate of Liquefied Natural Gas in Mark III tanks of ship carriers by numerical analysis, Appl. Therm. Eng. 93, 279-296

[6] Miguet F., Groleau D., A daylight simulation tool for urban and architectural spaces – application to transmitted direct and diffuse light through glazing - Build Environ., 2002 : 37, 833-843

[7] Milliez M. and Carissimo B., Numerical simulations of pollutant dispersion in an idealized urban area, for different meteorological conditions - Bound.-Layer Meteor., 2007: 122(2), 321-342

[8] Milliez M., Carissimo B., CFD modelling of concentration fluctuations in an ideal-ized urban area for different meteorological conditions - Bound.-Layer Meteor., 2008: 127(2), 241-259

[9] Oke T. R., Boundary Layer Climates. 2nd ed. - Routledge, 1987: 435 pp

[10] Qu Y., Milliez M., Musson-Genon L., Carissimo B., Micrometeorological modeling of radiative and convective effects with a building-resolving code - J. Appl. Meteor. Climatol., 2011: 50 (8), 1713-1724

[11] Qu Y., Milliez M., Musson-Genon L., Carissimo B., Numerical study of the thermal effects of buildings on low-speed air-flow taking into account 3D atmospheric radiation in urban canopy - J. Wind Eng. Ind. Aerodyn. 2012: (104–106), 474–483

[12] Qu, Y., Noba, I., Xu, X., Privat, R., Jaubert, J-N., A thermal and thermodynamic code for the computation of Boil-Off Gas – Industrial applications of LNG carrier, Cryogenics (2018), doi: https://doi.org/10.1016/j.cryogenics.2018.09.002

[13] Qu, Y., M. Milliez, L. Musson-Genon and B. Carissimo, 2020: Three-dimensional modelling of radiative and convective exchanges over a European city centre, paper submitted to J. Atmosphere

[14] Stewart I.D., Oke T.R., Local climate zones for urban temperature studies - Bull. Amer. Meteor. Soc., 2012: 93(12), 1879–1900

[15] Zaïdi H., Dupont É., Milliez M., Carissimo B., Musson-Genon L., Numerical simulations of the microscale heterogeneities of turbulence observed on a complex site - Boundary-Layer Meteor., 2013: 147, 237-25